Synthesis of High Catalytic Activity Bismuth-based Photocatalysts and Their Application in Wastewater Treatment

January 2019

Youju Shu

Synthesis of High Catalytic Activity Bismuth-based Photocatalysts and Their Application in Wastewater Treatment

A Dissertation Submitted to
the Graduate School of Life and Environmental Sciences,
the University of Tsukuba
in Partial Fulfillment of the Requirements
for the Degree of Doctor of Philosophy in Environmental Studies
(Doctoral Program in Sustainable Environmental Studies)

Youju Shu

Abstract

Photocatalytic technology plays an important role in the fields of energy and environment since its development in 1970s. In the past forty years, numerous attempts have been made to develop highly efficient and stable photocatalysts. However, poor visible light absorption efficiency and high recombination rate of electron-hole are still challenging their commercial application.

BiOX (X=Cl, Br, I) is a kind of typical bismuth-based photocatalysts with narrow band gaps that can absorb light in the visible region; still, photogenerated carriers are easy to recombine. In this study, four strategies were adopted to improve photocatalytic activity of BiOX, including breaking the layered structure of BiOX, introduction of nonstoichiometric crystal defects, increasing photocatalyst surface area, and formation of semiconductor composite. Major results can be summarized as follows.

(1) $Bi_4O_5Br_2$ photocatalyst was prepared by adjusting the alkalinity of synthesis system with polyethylene glycolpol-10000 (PEG-10000) as a directing agent, resulting in multiple facets and a uniform sheet-like nanostructure (50 nm in thickness). The prepared photocatalyst exhibited a high visible-light activity with the maximum light absorption at 500 nm. By using $Bi_4O_5Br_2$, 100% of decolorization was achieved in 10 mg/L Rhodamine B (RhB) solution within 20 min, and this high efficiency also remained after recycling the used $Bi_4O_5Br_2$ for 5 times. In addition, $Bi_4O_5Br_2$ photocatalyst exhibited good detoxification effect on chromium (Cr(VI)) through reduction into stable Cr(III) in wastewater under visible light, yielding about 90% Cr(VI) reduction within 120 min at an initial solution pH11.

(2) In order to improve the specific surface area of single-phase catalyst $Bi_4O_5Br_2$ and its photocatalytic efficiency as well, another new photocatalytic mesoporous material, namely $Bi_4O_5Br_2$/SBA-15 was synthesized at different loadings of $Bi_4O_5Br_2$ on the mesoporous silica material (SBA-15). The synthesized photocatalyst was confirmed to be a composite material with mesoporous structure, exhibiting a high visible-light absorption intensity and a low recombination rate of photo-generated electrons and holes. Along with the increase in $Bi_4O_5Br_2$ loading, the band gap was found to slightly decrease from about 3.30 eV to 3.10 eV. When the mass ratio of Bi/SiO_2 was 30/100 during the synthesis, the obtained photocatalyst (Bi_{30}/SBA-15) reflected the fastest RhB decolorization, reaching to 100% within 20 min in 10 mg/L RhB solution. This high decolorization efficiency still remained after recycling the used composite for 5 times. The obtained photocatalyst was also trialed for high concentration ammonium

nitrogen and Cr(VI) removals, in which 81.3% of ammonium nitrogen and 100% of Cr(VI) were achieved within 120 min when treating the simulated wastewater. In this study, $Bi_4O_5Br_2$/SBA-15 with mesoporous structure showed good adsorption and photoreduction capacity. The enhanced visible-light photocatalytic activity of the synthesized $Bi_4O_5Br_2$/SBA-15 can be ascribed to the existing active sites both inside and outside of SBA-15, and thus improved separation of photo-generated electrons and holes.

(3) In this study, ZrO_2 and WO_3 were further introduced into the structure of mesoporous $Bi_4O_5Br_2$/SBA-15 to form the narrow band gap catalyst $Bi_4O_5Br_2/ZrO_2$-WO_3/SBA-15. After the morphology, composition, structure and properties being confirmed, the composite $Bi_4O_5Br_2/ZrO_2$-WO_3/SBA-15 particles (between 3 and 4 nm) were found to have narrower band gap (2.98 eV) than $Bi_4O_5Br_2$/SBA-15 ones. The $Bi_4O_5Br_2/ZrO_2$-WO_3/SBA-15 composite could decolor 10 mg/L RhB within 10 min, exhibiting higher visible light photocatalytic activity than $Bi_4O_5Br_2$/SBA-15. The high photocatalytic performance can be attributed to the n-p type heterojunction of $Bi_4O_5Br_2/ZrO_2$-WO_3/SBA-15, beneficial for the effective separation of photo-generated electron-hole pairs. After 5 cycles' reuse, the RhB decolorization efficiency by $Bi_4O_5Br_2/ZrO_2$-WO_3/SBA-15 only decreased by 10.0%. This ternary composite was also found to have better decontamination effects on organic/inorganic matters under visible light.

(4) Another trial for the enhancement of the visible-light photocatalytic activity of $Bi_4O_5Br_2$ was to prepare graphitic carbon nitride (g-C_3N_4)/$Bi_4O_5Br_2$ composite by using in-situ synthesis method. The synthesized g-C_3N_4/$Bi_4O_5Br_2$ was found to have strong light absorption in the visible region due to its narrower band gap than g-C_3N_4. 100% of 10 mg/L RhB decolorization and 80% of phenol removal were achieved by g-C_3N_4/$Bi_4O_5Br_2$ within 15 and 120 min, respectively, with the highest photocatalytic activity obtained at the g-C_3N_4 /$Bi_4O_5Br_2$ mass ratio of 5:5. Meanwhile, the composite possessed a large specific surface area (26.90 m^2/g) and highly stable photocatalytic activity (99.6% of RhB decolorization remained after 5 times' recycling of the used composite). g-C_3N_4/$Bi_4O_5Br_2$ composite was also found to have detoxification effect on Cr(VI) in wastewater under visible light.

Results from this study are expected to provide experimental and scientific data for the development of highly efficient bismuth-based photocatalysts to realize their application in practice in the future.

Key words: Bismuth-based photocatalyst; $Bi_4O_5Br_2$; Visible light; Decolorization; Detoxification

Contents

List of tables

List of figures

Chapter 1 Introduction

In recent years, with the rapid development of the industrialization process, environmental pollution has become more and more serious [1]. Dye wastewater from textile, printing and dyeing industries has become increasingly harmful in cities, especially to the environment and human health [2, 3]. Once discharged into the aquatic system, dye wastewater would contaminate water source by strong colorating, inhibitting sunlight penetration, hindering the photosynthesis of aquatic organisms and affecting the growth of aquatic species [4, 5]. At the same time, the toxicity, mutagenicity and carcinogenicity of dyes would cause irreversible damage when the aquatic species are directly contacted [6]. In addition, heavy metals, high concentration ammonium nitrogen and phenol are difficult to remove, which cause adverse effects on our biosphere [7-9]. Therefore, how to efficiently control the pollution from wastewaters has become an important issue for human life and the society.

Currently, photocatalytic technology is considered as a promising method for solving dye wastewater pollution, because it can transfer organic macromolecule of dyes into water and carbon dioxide under ultraviolet and visible light [10, 11]. In the past 40 years, photocatalytic technology has been applied in other fields such as H_2 generation, nitrogen fixation, photochemical organic synthesis and antibacteria [12-15].

1.1 Photocatalytic technology

In 1972, two Japanese scholars, Fujishima and Honda first discovered photocatalytic decomposition of water could be used to produce hydrogen and oxygen by TO_2 photoelectron under ultraviolet (UV) illumination [16]. By using semiconductor particles or powders as photocatalysts, Bard designed a photocatalytic system to replace the photoelectrochemical electrodes [17-19]. Since then, TiO_2 photocatalytic technology has unprecedentedly received an extensive global attention for the development of new energy and the protection of the ecological environment. In 1976, Carey et al. reported that TiO_2 could dechlorinate and degrade the organic compound polychlorinated biphenyl under ultraviolet light [20]. However, the development and application of TO_2 is largely limited due to some key technical problems such as its wide band gap and the difficulty of loading on the carrier [21, 22]. For more than 40 years, scientists have carried out a lot of research work in the fields of physical chemistry and materials, and made great progress in the principle, application and development of photocatalysts.

1.1.1 Basic principles

The basic principles of photocatalytic technology can be introduced as the following reaction formula from (1-1) to (1-10), which are based on the generation of electron-hole pairs by a narrow bandgap of semiconductor excited under light irradiation. Generally, the band structure of a semiconductor is composed of an electron-filled highest valence band (VB) and a minimum conduction band (CB) that is not filled with electron. When the photon energy is greater than its own band gap energy (Eg) of photocatalyst, the photocatalyst can absorb the photon energy to promote the photo-generated hole (h^+) on the valence band accorgingly. Subsequently, the photocarriers are separated into a free electron (e^-) and a free hole (h^+) under the excited condition of photocatalyst. Once free electrons and holes are captured, the photooxidation reaction and photoreduction reaction of photocatalyst will happen on the VB and CB under light irradiation, respectively. Therefore, the result shows that the trapped h^+ directly reacts with the adsorbed donor molecule on the VB, and the trapped electron e^- reacts with the acceptor on the CB. In addition, the photocatalyst will lose activation when the electron-hole pairs release energy and recombine at the surface capture point. For example, when the photogenerated hole reacts with the water adsorbed on the surface of photocatalyst, a highly reactive hydroxyl radical •OH will be formed on the main active sites as oxygen species, and the superoxide radical anion ($•O_2^-$) and pure oxygen (O) are present to form another source of ROS production with oxygen. The trapped holes adsorbed on the souface of the molecule can also generate a radical cation $•RH^+$, and then form a radical species •R. Generally, heterogeneous photocatalyst includes an excitation source and some active species that can greatly promote photodegradation. The mechanism of free radical can be expressed by the following reaction formulas [23]:

$$\text{Photocatalyst} + h\nu \rightarrow h^+ + e^- \quad (1\text{-}1)$$

$$h^+ + H_2O \rightarrow •OH + H^+ \quad (1\text{-}2)$$

$$h^+ + OH^- \rightarrow •OH \quad (1\text{-}3)$$

$$h^+ + \text{pollutant} \rightarrow (\text{pollutant})^+ \quad (1\text{-}4)$$

$$e^- + O_2 \rightarrow •O_2^- \quad (1\text{-}5)$$

$$•O_2^- + H^+ \rightarrow •OOH \quad (1\text{-}6)$$

$$2•OOH \rightarrow O_2 + H_2O_2 \quad (1\text{-}7)$$

$$H_2O_2 + •O_2^- \rightarrow •OH + OH^- + O_2 \quad (1\text{-}8)$$

$$H_2O_2 + h\nu \rightarrow 2\ •OH \quad (1\text{-}9)$$

$$\text{Pollutant} + (\bullet OH, h^+, \bullet OOH \text{ or } \bullet O_2^-) \rightarrow \text{degradation product} \quad (1\text{-}10)$$

There are three main active species such as hydroxyl radical (•OH), hole (h^+) and superoxide radical ($\bullet O_2^-$) during the photocatalytic reaction process. •OH is considered as the main oxidant for degrading pollutants in solution under light irradiation. •OH is generated by the following two steps: firsty, photogenerated holes (h^+) easily make water molecules (H_2O) and hydroxide ions (OH^-) form •OH, such as reaction formula (1-2). After that, photogenerated electrons (e^-) reduce oxygen (O_2) to generate superoxide radicals ($\bullet O_2^-$) in aqueous solution, and then superoxide radicals ($\bullet O_2^-$) combine holes (h^+) to form •OOH radicals, and finally further decompose $\bullet O_2^-$, as shown in reaction formulas (1-3) to (1-9). And photogenerated holes (h^+) are widely recognized as an oxidant to directly degrade organic pollutants (1-10) [23]. It is worth mentioning that the photoinduced e^- is easily recombined with h^+ under the absence of electrons and holes trapping agents. Therefore, special trapping agents play an important role in the separation of photogenerated electron-hole pairs for enhanced photocatalytic efficiency.

1.1.2 Photocatalytic materials

Photocatalytic material is defined as photocatalyst, which can decompose detrimental substances under the sun light containing UV rays. In order to develop of H_2 energy and to protect the environment, more and more photocatalytic materials have been developed and produced. At present, there are mainly three types of photocatalysts as follows: binary metal oxide semiconductor, amorphous oxide semiconductor, and non-oxide semiconductor photocatalysts. The binary metal oxide semiconductor materials are single-phase semiconductor photocatalysts [25-27], such as TiO_2, WO_3 and ZnO. However, these photocatalysts have large forbidden band width, which could enhance the band gap range. The amorphous oxide semiconductor photocatalysts mainly include BiOX (X=Cl, Br and I) [28, 29], Bi_2WO_6 [30, 31], and $BiMoO_6$ [32, 33]. The non-oxide semiconductor photocatalysts are single-phase semiconductor materials with no oxygen in the composition. In the past few decades, research on non-oxide semiconductor photocatalyst was focused on environmental remediation, with several breakthroughs being achieved. For example, Wang et al. prepared an Ag@AgCl photocatalyst to reduce part of AgCl into Ag particles to effectively solve the optical instability of AgX via its surface plasma resonance [34].

Among these three types of photocatalysts, bismuth-based photocatalysts have the best photocatalytic performance on pollutants removal under ultroviolet and visble light (Table 1-1), due to their unique layered structure promoting the separation of photoelectrons and holes.

Therefore, bismuth-based photocatalysts have been received more and more attention in wastewater treatment and energy generation.

1.2 Bismuth-based photocatalyst

1.2.1 Classification of bismuth-based photocatalyst

Bismuth is a metal element with atomic number at 83 in the fifth main group and the sixth period in the periodic table. The electrons of outermost layer are arranged in 6s26p3, which shows stable valence state at +3. It is widely distributed with special structure and stable valence state on the earth. Bismuth-based photocatalyst has an obvious light absorption in the visible range because the bismuth element structure can drive the hybridization of the 6s orbital (Bi6s) and the 2p orbital (O2p) of oxygen to increase electron transition. Based on these characteristic, many bismuth-based photocatalysts have been synthesized such as $BiVO_4$ [35], Bi_2WO_6 [36], Bi_2MoO_6 [37], $Bi_4Ti_3O_{12}$ [38, 39], $BiFeO_3$ [40, 41], $Bi_2Fe_4O_9$ [42, 43], $Bi_5FeTi_3O_{15}$ [44], BiOX (X = Cl, Br, I) [45, 46] and so on. BiOX (X = F, Cl, Br, I) is a typical type of bismuth-based photocatalyst with a PbFCl crystal structure including a symmetry of D 4h, a space group of P4/nm, and the tetragonal system [45, 46]. The valence band of BiOX mainly consists of Xnp (n=2(F), 3(Cl), 4(Br), 5(I)) and O2p orbitals, while the conduction band is mainly contributed by Bi 6p orbital [47]. BiOX of BiOCl, BiOBr and BiOI have a staggered heterojunction by $[Bi_2O_2]^+$ layer and two layers of halogen atoms combination. Zhang et al. first successfully prepared BiOX (X=Cl, Br, I) by one-pot solvothermal method with ethylene glycol as solvent. It was found that the prepared particles of BiOI were microspheres by self-assembly nanosheets, which enhanced the organic matters degradation under visible light [48]. Chen et al. used a surfactant of polyvinylpyrrolidone and solvent of ethylene glycol to form nanomicrospheres by solvothermal method [49]. It had greatly improved the photocatalytic performance under visible light.

BiOX (X=Cl, Br and I) is stable, non-toxic and resistant to acid and alkaline conditions [47]. Interestingly, the atoms of the layered structure are connected by strong covalent bonds, and the layers are contacted by van der Waals forces. Once the layered structure is peeled off, the opened layered structure would grow along {001} facet under weak Wan der Waals force [50]. In addition, there is an internal electric field formed between the $[Bi_2O_2]^+$ layer and the halogen layer, which increases the separation rate of electrons and holes. Huang et al. used density functional theory to explain the internal electric field of BiOX between the indirect transition bandgaps [51]. The CB of BiOX is found to be composed of Bi_{6p} and the VB is

occupied by O_{2p} and X_{np} (n=2(F), 3(C1), and 4(Br)) orbitals [46]. The photogenerated electrons of indirect transition bandgap can return to the VB through k layers, which reduces the probability of carrier recombination [52].

Band gap energy of photocatalyst is an important index that affects light absorption and catalytic performance. Among BiOX photocatalysts, BiOCl has a wide band gap (3.2eV) and can only respond to ultraviolet light. While BiOI has good responsiveness to ultraviolet and visible light, but its too small band gap width (1.7 eV) makes photogenerated carriers easy recombine. The VB potential of BiOI is the lowest, therefore, the oxidization ability of hole is the weakest [53]. BiOBr has a better visible light responsiveness and suitable band gap width (2.7 eV), which has a good research value [54-58].

BiOBr is becoming a research hotspot because of its high catalytic activity under visible light irradiation and suitable band structure among the BiOX catalysts [59]. However, photogenerated carriers are found to easily combine which is a common problem of BiOBr [60]. Therefore, many researchers are working hard to look for effective strategies and further improve the photocatalytic performance of BiOBr, such as morphology control [60-62], multiple crystal faces exposure [63, 64], and heterogeneous hybridization [65].

Some researches confirmed that the increase of bismuth dosage could change the facets crystallization and layered structure to improve the photocatalytic performance of BiOBr [66-68]. Density functional theory (DFT) calculations show that the VB of BiOBr is mainly composed of hybrid orbitals of Br 4p and O 2p, while the bottom of CB is mainly composed of Bi 6p orbitals [65]. It is also clear that Bi content could expand the CB and VB edges of BiOBr. Recently, some bismuth-rich BiOBr have been synthesized to enhance the photocatalytic performance, such as $Bi_4O_5Br_2$ [69], Bi_3O_4Br [66] and $Bi_{24}O_{31}Br_{10}$ [67]. However, it is still scarcy in their practical application. An ideal condition is to design a new type of bismuth-rich ultrathin nanosheets in the photocatalyst. Based on the diffusion equation, $t = d^2/k^2\mathrm{D}$ (d is the particle size, k is a constant, D is the diffusion coefficient of the electron-hole pair), the ultrathin thickness can make the d value smaller, while a higher D value is obtained in the internal electrostatic field. Therefore, an ultrathin nanostructure of BiOBr can achieve higher carrier mobility and lower recombination rate [70].

1.2.2 Problems of bismuth-based photocatalyst

Bismuth-based photocatalysts have attracted considerable research interests because of their suitable band gap structure capable of absorbing sunlight for photocatalytic reactions.

However, their practical application is still limiteddue to some inherent drawbacks. For example, BiOCl is only responsive to ultraviolet light regions that account for 4% of sunlight. Although BiOBr and BiOI are capable of absorbing visible light, the wide band gap of BiOBr still limits their effective use of visible light, and the relatively narrow band gap of BiOI inevitably increases the recombination probability of photogenerated carriers [59]. In addition, the band gap of BiOX is mismatched with light-trapping, and fewer active sites will result in inefficient separation of photogenerated electron-hole pairs. Therefore, to find the strategies to solve the above problems is very important.

1.3 Strategies to improve the photocatalytic activity

Based on the above problems of bismuth-based photocatalysts, some strategies can be applied to design layered structures to overcome these drawbacks. These strategy approaches are summarized as follows.

1.3.1 Surface decoration

Photocatalytic performance is largely dependent on the surface characteristics of the semiconductor, because photocatalytic reactions usually occurr on the surface of semiconductor [68]. Therefore, surface decoration of the photocatalyst is affective to well promote the photocatalytic performance. There are two ways by surface modification to form oxygen vacancies and modify the surface functional organic molecules. One way is to create oxygen vacancies on the surface of the semiconductor [71]. Oxygen vacancy has two effects on the bismuth oxyhalide photocatalyst. Firstly, oxygen vacancy can change the light absorption capacity of gas molecules such as CO, H_2O, O_2, and H_2 on the photocatalyst surface combination [72]. Secondly, surface oxygen vacancy can provide an effective method for adjusting the electronic properties of BiOX semiconductor to enhance light absorption and charge mobility. Surface modification can inhibit photoinduced carrier recombination by modifying functional organic molecules such as electron or hole trapping agents on the surface of BiOX. Metal decorating is an ideal method for single phase catalyst modification. Furthermore, it has been reported that heterogeneous and homogeneous metal decorating could enhance the photocatalytic activity of photocatalyst. For instance, Liu et al. used Ag nanoparticles loading onto the BiOI flower-like nanostructure by solvothermal method [73]. Ag/BiOI photocatalysts ha excellent photocatalytic activity for organic

pollutants under visible-light irradiation due to Ag nanoparticles surface plasmon resonance (SPR) and electron trapping ability [74]. Jiang et al. successfully used Fe and Ti loading on the BiOBr hollow-structured flower-like microspheres by solvothermal method to dope iron onto the BiOBr of the flower-like microsphere structure to enhance visible light absorption [75]. Mn [76], Pt [77], Ti [78] and so on were studied to modify the layered BiOX photocatalyst, which enhanced catalytic activity by high efficiency photogenerated electrons separation. Unfortunately, excessive heterogeneous nano-metal particles are easily agglomerated during synthesized system, resulting in low specific surface area and quantum efficiency. Homogeneous metal decoration also shows some advantages, such as easier control of synthesis condition, no impurity production, and well matched metal in the synthesized heterojunction. Yang et al. used Ag nanoparticles as templates to synthesize small particle size Ag/AgCl photocatalysts by in-situ oxidation, and the synthesized Ag/AgCl photocatalysts exhibited excellent photocatalytic activity for organic pollutants under visible-light irradiation [79]. Wang et al. reported the preparation of plasmonic Cu/Cu_2O composite photocatalysts, and it was confirmed that the photocatalytic activity under visible light was much higher than Cu_2O [80]. However, it is difficult to control the synthesis operation because the metal particles are easily oxidized to oxide. Bi is a stable and environmental element, which can be reduced on the surface of monomer catalyst [81]. Metals/semiconductors composite provides a new way to design solar energy harvesting processes. In a plasma photocatalytic system, plasma metal nanoparticles with the ability to collect visible light were loaded on a semiconductor to create a resonance of a free electron coherent oscillation and an electromagnetic radiation electric field, forming a so-called local surface plasmon resonance [82, 83]. The nanostructures of metal nanoparticles can couple with BiOX semiconductors to enhance the photocatalytic performance of BiOX. And these plasma photocatalysts can be obtained by metal nanoclusters on the surface of semiconductor with photochemical deposition and ion exchange reaction.

1.3.2 Crystal facet adjustment

In the layer structure of bismuth oxyhalide, the strong interlayer covalent bond of $[Bi_2O_2]^+$ layer and the weak van der Waals force of the halogen double layer can form a polarizable atom and orbit, which induces the orientation along the crystal orientation perpendicular to internal electric field (IEF) of the $[Bi_2O_2]^+$ layer and the halogen layer. The IEF can promote the

separation and migration of photogenerated carriers by this unique layered structure. Jiang et al. found that the {001} independent crystal face of BiOCl single crystal nanosheets exhibited higher photocatalytic performance for salicylic acid than that of the {010} independent crystal face nanosheets under ultraviolet light [84]. This phenomenon is due to the layered structure mediated IEF which could induce more nanosheets in the {001} direction than in the {010} direction. Effectively photogenerated charge separation and migration could inhibit the recombination of photogenerated electron-hole pairs and enhance photocatalytic degradation. Li et al. found that increasing the exposure ratio of the {001} crystal plane of Bi_3O_4Cl nanosheets could induce a strong IEF and promote the enhancement of photoreactivity [85]. The IEF of Bi_3O_4Cl nanosheets was confirmed in the {001} crystals by the voltage and charge density of the surface, and the percentage of the face was related to the size of IEF. Therefore, a higher exposure of the {001} plane could significantly increase the separation and migration efficiency of electron-hole pairs.

1.3.3 Heterojunction formation

Constructing heterojunction is also an effective method to improve the photocatalytic performance of BiOX. The heterojunction can be formed by integrating different components into a multi-component composition with better photocatalytic performance than the single semiconductor [86]. In general, BiOX nanomaterials may play a three-fold role in the semiconductor heterojunction systems.

Firstly, BiOX has a redox potential in a wide range. They are easily matched with the energy levels of different semiconductors to establish an IEF and enhance the separation and transmission of photogenerated electron-hole pairs, such as Bi_2WO_6/BiOI [87], C_3N_4/BiOBr [88], AgBr/BiOBr [89]. Secondly, narrow band gap BiOX semiconductors such as BiOBr and BiOI are capable of photosensitizing other wide-bandgap semiconductors for efficient use of sunlight, such as BiOI/ZnO [90] and BiOI/TiO_2 [91]. Lastly, BiOX can be coupled with carbon-based nanomaterials to improve charge separation and transport, especially graphene, such as BiOCl/graphene [92], BiOBr /graphene [93], and BiOI/graphene [94]. Therefore, the transfer of electrons from BiOX to graphene could effectively increase the separation rate of electron-hole pairs, thereby, enhancing the lifetime of carriers and the photocatalytic efficiency.

1.4 Research objective and originality

BiOX (X=Cl, Br, I) is a kind of typical bismuth-based photocatalysts with narrow band

gaps that can absorb light in the visible region. Still, their quantum size is small, special light response is poor, and photogenerated carriers are easy to recombine. Therefore, in this study, four strategies are adopted to improve photocatalytic activity of BiOX, including breaking the layered structure of BiOX to introduce nonstoichiometric crystal defects, loading single phase photocatalyst to increase photocatalyst surface area, forming p-n heterojunction by tenary metal composite, and formation of semiconductor composite. The objective of this study is to design and synthesize new bismuth-based photocatalysts, and ensure the photocatalyst activity and stability before its practical application. In this context, the investigation on the new synthesized photocatalyst characteristics such as XRD patterns, morphology structure, composition and optical property, and their application in dyes wastewater treatment were carried out to disclose the reaction mechanisims. In general, this study is expected to provide new methods for photocatalyst synthesis and to realize the practical application of photocatalyst under visible light. Up to the present, few reports are available on the above mentioned aspects.

1.5 Structure of this dissertation

As shown in Fig. 1-1, the contents of this thesis are divided into the following six parts so as to obtain highly effective photocatalysts for dyes wastewater treatment.

In Chapter 1, the senticfic proplems of photocatalyst BiOX was put forward, which is mainly relating to the easy recombination of photogeneration electron-hole pairs easily. After addressing the probably enhancement methods, the objective of this research was arrived along with the structure of the dissertation.

In Chapter 2, $Bi_4O_5Br_2$ was designed and synthesized by breaking the layered structure of BiOBr using a directing reagent PEG-10000 by adjusting system pH to form facets defect structure in addition to the introduction of nonstoichiometric effect to form bismuth-rich decoration. The polycrystalline facet $Bi_4O_5Br_2$ photocatalyst was characterized by morphology, structure, photocatalytic performance and stability.

In Chapter 3, $Bi_4O_5Br_2$/SBA-15 was designed and synthesized by loading $Bi_4O_5Br_2$ on the SBA-15 mesoporous molecular sieves with an expectation of high activity and photocatalytic performance. The characterization, photocatalytic performance and other properties were determined in this chapter.

In Chapter 4, in order to further enhance the photocatalytic performance, the ternay element composite catalyst of $Bi_4O_5Br_2/ZrO_2$-WO_3/SBA-15 was designed, and synthesized and characterized.

In Chapter 5, it was attempted to couple $Bi_4O_5Br_2$ with g-C_3N_4 to form p-n heterojunction, and its photocatalytic performance was confirmed by RhB degradation under visible light.

Finally in Chapter 6, the characteristics of the above synthesized photocatalysts were summarized and compared. Future research works were proposed regarding the improvement of practical application performance of the synthesized photocatalysts.

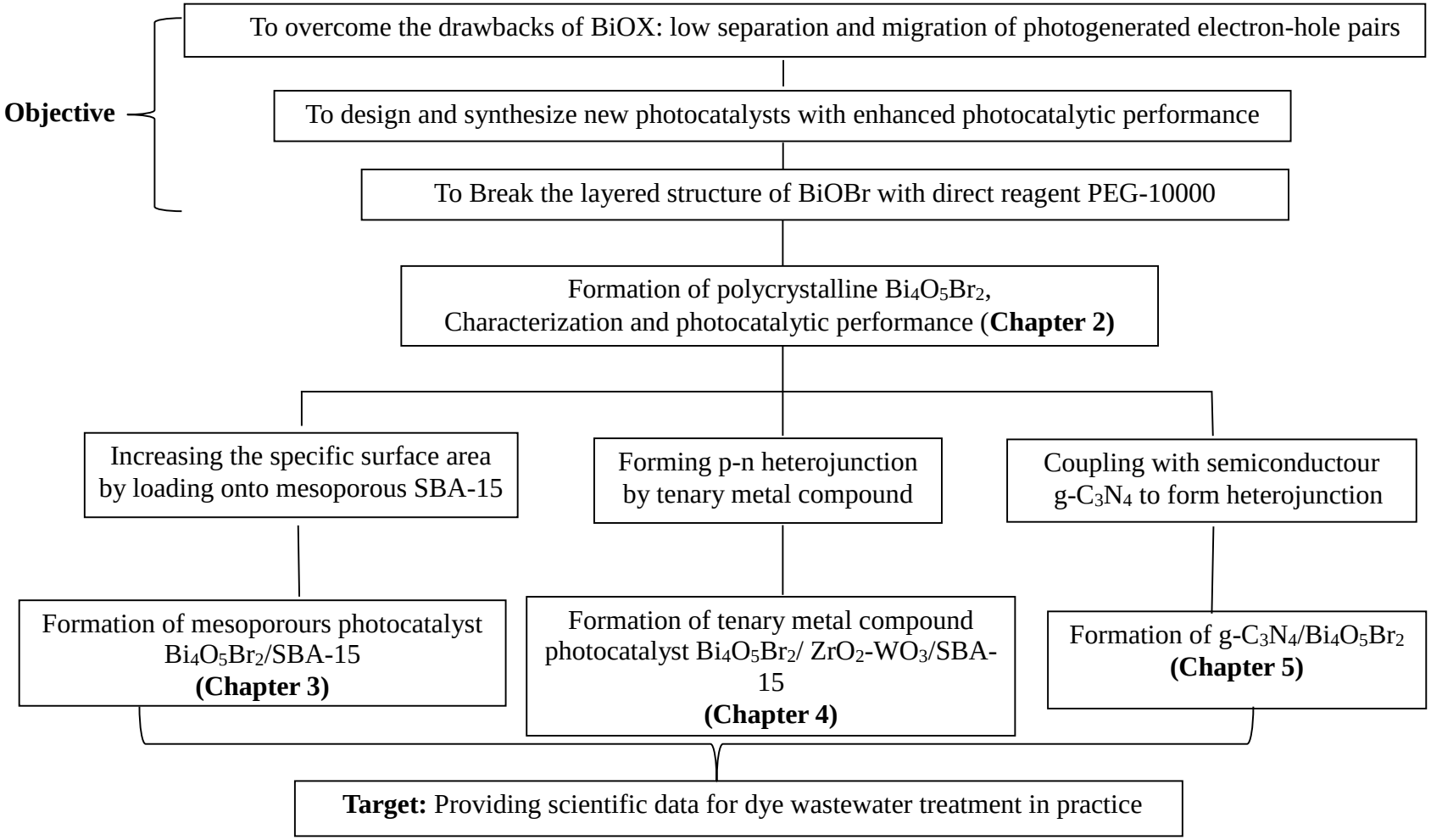

Fig. 1-1 Framework of the dissertation

Chapter 2 Synthesis of polycrystalline $Bi_4O_5Br_2$ with enhanced visible-light-driven performance

2.1 Introduction

Bismuth oxyhalides (BiOX (X = Cl, Br, I)), originally belonging to the Sillen family, have demonstrated excellent photocatalytic activity because of their uniquely layered structure, which features an internal static electric field perpendicular to each layer and facilitates the separation of photogenerated charge carriers [95]. Among BiOX samples, BiOBr has attracted particular attention due to its suitable band gap value (2.7 eV), visible light-responsive ability, and excellent photocatalytic performance [95-98]. It has two different absolute band gaps, which causes different oxidation reactions under ultraviolet light and visible light [99]. It is worth mentioning that BiOBr has unique exposed crystal planes, which could enhance its photocatalytic performance [100]. However, due to their conduction band minimum located too positive potential, the photocatalytic activity of BiOBr was still very low for toxic matters removal and its by-products generation [101, 102].

Based on these problems, some strategies have been produced to enhance its photocatalytic performance, such as facet regulating [85, 103], surface modification [71, 92], doping [104-107], fabricating plasmonic photocatalytic system [108-110] and forming heterojunction [111-118]. Density function theory (DFT) calculations of BiOBr indicate that its valance band maximum (VBM) mainly consists of Br 4p and O2p orbitals, while the Bi 6p orbitals dominated the conduction band minimum (CBM). The theoretical calculation suggests that an effective way to upshift the CBM position of bismuth oxybromide is to increased content of bismuth. For example, bismuth-rich strategy is useful to form bismuth-rich photocatalyst by changing the stoichiometric ratio of Bi, O, and Br has been adopted for BiOBr modification, such as $Bi_4O_5Br_2$ [69], Bi_3O_4Br [66] and $Bi_{24}O_{31}Br_{10}$ [67]. However, it is still a significant challenge to prepare $Bi_4O_5Br_2$ with facile, low cost and green method. Generally, PEG-10000 is a very green, co-effective and environmentally bio-based degradable material. It is also an ideal directing agent due to its slow growth, rapid growth, rapid terminating reaction and mild condition requirements when it undergoes free radical polymerization [119]. To the best of our knowledge, one step synthesis of $Bi_4O_5Br_2$ photocatalyst with polymer (PEG-10000) as directing agent has not been reported.

Heavy metals are one of the main pollutants in water sources, which have heavy toxicity and non-degradability. Chromium is a typical heavy metal with valence states of Cr(VI) and Cr(III) in aquatic ecosystem. Compared with Cr(III), Cr(VI) is very dangerous for human health due to its inhibition for biological enzyme activity and strong carcinogenic by respiration [120]. Therefore, Cr(VI) detoxification is very urgent for human health and environmental safety. Previously, adsorption method has been considered as a promising method for heavy metals removal in the field of environmental control. So far, few reports could be found on chromium detoxification by $Bi_4O_5Br_2$ photocatalyst.

In this chapter, $Bi_4O_5Br_2$ photocatalyst was synthesized using a hydrothermal method with polymer template as directing agent and pH adjustment. The characterization and photocatalytic performance were investigated, and the synthesis conditions of $Bi_4O_5Br_2$ were optimized based on Rhodamine B (RhB) decolorization test. Chromium removal experiment was invesitigated in synthetic wastewater by $Bi_4O_5Br_2$ photocatalyst.

2.2 Materials and methods

2.2.1 Synthesis of $Bi_4O_5Br_2$ composite

$Bi_4O_5Br_2$ was synthesized with a solvothermal method. Typically, Under stirring at 100 rpm, Cetyl trimethyl ammonium bromide (CTAB, 1.5 mmol) and $Bi(NO_3)_3$ $5H_2O$ (1.5 mmol) were added and dissolved in the glycerol solution (15 mL glycerol and 6 mL deionized water, stirring for 30min), then the stirring lasted for 30min. 0.1 g polymer (such as Polyethylene glycol -10000(PEG-10000), adjusting the pH with hydrochloric acid (HCl) and ammonia solution to 3, 7, 10, 11, and 12, respectively, the obtained mixture was solvothermally treated at 150 ℃ for 24 h. The obtained solid after centrifugation was washed with water and ethanol for 5 times, and then dried at 60 ℃ for 12 h.

2.2.2 Characterization of the catalyst

X-ray diffraction (XRD) measurement was conducted on a D/max-2550 PC X-ray diffractometer. Scanning electron microscope (SEM, Hitachi S-4800) and transmission electron microscope (TEM, JEOL JEM-2100 high-resolution transmission electron microscope (HRTEM)) were also used to characterize the obtained photocatalysts, respectively. The Brunauer-Emmett-Teller (BET) surface area was determined by a micromeretics ASAP 2010 apparatus with a multipoint BET method using the adsorption data in the relative pressure (P/P_0) range of 0.05-0.3. The desorption isotherm curves were used to explain the pore size

distribution according to the Barrett-Joyner-Halenda (BJH) method. EDS was used to determine the chemical elements and their relative abundance in the samples. The optical diffuse reflectance spectra (DRS) was acquired with a UV-vis-NIR scanning spectrophotometer. The photoluminescence (PL) spectra were obtained on fluorescence spectrophotometer (Hitachi F2500). X-ray photoelectron spectra (XPS) analysis was performed on a PHI-5400 instrument with Mg Kα as the X-ray source under a pressure of 1.33×10^{-7} Pa and a step of 0.05 eV. The C (1s) level (285.0 eV) was taken as the reference binding energy.

2.2.3 Photocurrent density test

The synthesized samples (20 mg, respectively) were dispersed in 200 μL N, N-Dimethylformamide (DMF) solution respectively for 1 h to obtain liquid suspension. 20 μL of the above suspension was transferred onto the conductive surface of FTO glass to form a 1 cm^3 film at 80 ℃, and then dried for 20 min. Electrochemical analyzer was used to test the photocurrent density of the samples. The test system consisted of a standard three-electrode system. The sample film was used as the working electrode, a Pt electrode.

2.2.4 Photocatalytic activity measurement

The photocatalytic activities of as-prepared $Bi_4O_5Br_2$ composites were evaluated by the degradation of RhB aqueous solution under visible light irradiation. 10 mg/L of RhB solution was used to evaluate the photocatalytic activity of the obtained composites. The A 300 W xenon lamp with a 420 nm cut-off filter provided visible light irradiation. Prior to irradiations, the suspensions were magnetically stirred in the dark for 30 min to ensure the establishment of an adsorption–desorption equilibrium of RhB on the catalyst surface. Then, the solution were irradiated by xenon lamp. At given irradiation time intervals, 4mL of the suspensions were collected and then the slurry samples including the photocatalysts and RhB solution was centrifuged (10 000 rpm, 10 min) to remove the photocatalysts. The 725N UV-vis spectrophotometer (Beijing Purkinje General Instrument Co., Ltd.) was used to further analyze the concentration changes of RhB solution with the wavelength of 554 nm. The RhB solution temperature was controlled at 19 ± 2 ℃. A same photocatalyst dosage of 0.2 g/L was used for all the tests.

2.2.5 Active species trapping experiment

To detect the active species produced in the photocatalytic process, such as superoxides ($\bullet O_2^-$), hole (h^+) and hydroxyl radical (•OH), trapping experiments were carried out by adding different scavengers into the RhB solution (50 mL, 10 mg L^{-1}), including 1 mM $Bi(NO_3)_3 \bullet 5H_2O$, 1 mM sodium oxalate (SO), 1 mM p-benzoquinone (BQ) or 1 mM iso-propanol (IPA).

2.2.6 Chromium detoxification experiment

Chromium (Cr(VI)) stock solution (2000 mg/L) was prepared by dissolving 2.82 g of $K_2Cr_2O_7$ in 0.5 L deionized water. The working concentrations were prepared from this stock solution by deionized water. 50 mg/L of Cr(VI) solution was selected to analysize the removal rate of the obtained $Bi_4O_5Br_2$ photocatalyst. Firstly, Cr(VI) solution reached adsorption equilibrium with stirring in dark for 30 min, and then the solution was irradiated by A 300 W xenon lamp with a 420 nm cut-off filter providing visible light irradiation. Then, the residual solution of Cr(VI) was collected during the time intervals with 0.2 mL H_2O_2 and Cr(VI) solution were centrifuged (10 000 rpm, 10 min) to remove the photocatalysts as fast as possible. The concentration of Cr(VI) was determined by ICP-MAS.The distribution of ofchromium was analysized with the used photocatalysts for chromium transfernation by XPS. A same photocatalyst dosage of 0.2 g/L was used for all the tests.

2.3 Results and discussion

2.3.1 Characterization of $Bi_4O_5Br_2$

Fig. 2-1 shows the XRD pattern of the samples that prepared with and without polymer addition under different pH values (3, 7, 10, 11, 12) during the synthesis process. Fig. 2-1a indicates that the facet structure of the samples without PEG-10000 under different pH values was similar with BiOBr (JCPDS No. 09-0393) [121, 122], and the characteristic diffraction peaks of samples appeared in the vicinity of 25.0°, 31.5°, 46.2°and 57.2° with crystal facets position being corresponded with (110), (112), (020) and (220), respectively. However, there were no the characteristic diffraction peaks of samples without PEG-10000 at around 29°and 32°with $Bi_4O_5Br_2$ (JCPDS No. 37-0699) [122] indicating that PEG-10000 is very important for $Bi_4O_5Br_2$ formation. from Fig. 2-1b, it can be seen that the characteristic peaks of the samples synthesized with PEG-10000 at pH values 10, 11, and 12 have the characteristic peaks of tetragonal $Bi_4O_5Br_2$ (JCPDS No. 37-0699), and the characteristic peaks at around 29°and 32° could be attributable to the (101) and (110) planes of tetragonal $Bi_4O_5Br_2$, respectively. Cell

parameters show that a=14.520 Å, b=5.625 Å, c=10.830 Å, which prove that $Bi_4O_5Br_2$ has been synthesized successfully when PEG-10000 was added as a directing agent under pH 10, 11, and 12. It also can be seen that only after adjusting the pH to 11, the diffraction peak index of the obtained sample conforms to the monoclinic $Bi_4O_5Br_2$. The peak intensity of the diffraction peak is the highest, indicating that the optimal parameter of synthesizing $Bi_4O_5Br_2$ photacatalyst could be obtained only after adjusting the pH value of the reaction system to 11. In addition, since no other peaks belonging to impurities appeared in the XRD diffraction pattern, it indicates that the prepared $Bi_4O_5Br_2$ is single-phase and has high purity. The samples with PEG-10000 in the pH3 and pH7 reaction systems did not show obvious diffraction peaks. Since the two samples are relatively soft, it is considered to be a hydrate of bismuth at lower crystallinity. Then we further observed the phase of the product under the conditions of pH10 and 12. In the samples at pH10 and pH12, the characteristic diffraction peaks of $Bi_4O_5Br_2$ appeared in the vicinity of 29° and 32°, but they could not correspond well. It is believed that the lattice parameters should be changed. The particle size of different samples with PEG-10000 under different pH values was investigated by XRD in (Table 2-1). The particle size was bigger with the increase of system pH. The particle size was the biggest when the pH reached 11 with the crystal lattice formation, which also indicated that polymer PEG -10000 could promote the growth of $Bi_4O_5Br_2$ particles size under alkaline conditions [69].

Table 2-1 Particle size of samples synthesized with PEG-10000

Samples	2θ (°) (1)	D (nm)	2θ (°) (2)	D (nm)
pH=12	29	6.5	32	8.3
pH=11	29	9.3	32	9.7
pH=10	29	6.6	32	7.8
pH=7	29	n.d.	32	n.d.
pH=3	29	n.d.	32	n.d.

n.d. denots no data was collected.

The optical properties of the synthesized photocatalysts were investigated by UV-visible diffuse reflectance spectroscopy (DRS) as shown in Fig. 2-1(c). $Bi_4O_5Br_2$ synthesized with PEG-10000 had good visible light absorption performance and the absorption band edge showed a red-shift toward the visible region with an absorption onset at about 510 nm. The following equation (Eq. 2-1) showed the relationship between band gap and light absorption

[123, 124].

$$\alpha h\nu = A(h\nu - E_g)^{n/2} \quad (2\text{-}1)$$

where α, h, ν, E_g, and A represent the light absorption coefficient, Planck constant, optical frequency, band gap, and constant, respectively, and n depends on the characteristics of the semiconductor. For direct bandgap semiconductors, n = 1, and indirect bandgap semiconductors, n = 4. $Bi_4O_5Br_2$ is an indirect bandgap semiconductor, n = 4. Therefore, the bandgap value E_g of the $Bi_4O_5Br_2$ sample can be obtained by the tangent of the $(\alpha h\nu)^{1/2}$ - photon energy ($h\nu$) curve (Fig. 2-1(d)). It showed that the bandgap of the $Bi_4O_5Br_2$ synthesized with PEG-10000 was approximately 2.43 eV, which means that it has a low band gap, high visible light utilization and good photocatalytic activity.

The morphology of samples without PEG-10000 and with PEG-10000 at pH=11is shown in Fig 2-2. It is shown that the samples without PEG-10000 were agglomerates and disordered from Fig. 2-2(a-c), and there was no lattice nanosheet. The structure of $Bi_4O_5Br_2$ synthesized with PEG-10000 under pH 11 is shown in Fig. 2-2(d) to 2-2(f). It can be seen that the size of $Bi_4O_5Br_2$ was small, with the size ranging from 500 nm to 3 μm, and there is no obvious agglomeration phenomenon and disordered accumulation. The nanosheets and lattice of the sample under pH=11 with PEG-10000 were shown in Fig. 2-2(e-f), respectively.

Table 2-2 shows that the specific surface area of the sample with PEG-10000 gradually increases with the increase of pH value increasing, and the specific surface area reaches a maximum at pH=11, and then the specific surface area decreased. The reason for this result is that the polymer PEG-10000 undergoes a protonation reaction under acidic conditions, which inhibits the crossing of [-Bi-O-Bi-] and the group of PEG-10000. Under alkaline conditions, it is beneficial to the hydrolysis of the polymer, increasing the reactivity of Bi, and more favorable for crystal formation. The produced product itself of [-Bi-O-Bi-] is hydrolyzed under strong alkaline condition, resulting in difficulty in crystal formation. Compared with the samples without PEG-10000, the specific area is much higher than that of without PEG-10000.In order to further confirm the elemental composition and the valence state of synthetic photocatalyst, X-ray photoelectron spectroscopy was performed (Fig. 2-3). It can be seen from the element scanning spectroscopy (Fig. 2-3(a)) that only the peaks relating to the four elements of O, Bi, and Br appeared, indicating that the obtained sample had a high purity. The high resolution XPS for Bi 4f is shown in Fig. 2-3(b). The binding energies of Bi $4f_{5/2}$ and Bi $4f_{7/2}$ are 159.05 and 164.34 eV for $Bi_4O_5Br_2$ [125]. Fig. 2-3(c) shows O 1s peak of the $Bi_4O_5Br_2$ composites. The O 1s peak was deconvoluted into two peaks at 532.6 and 530.2 eV, which could be assigned to the

O-H bond and the lattice Bi-O [126]. The Br 3d spectra are shown in Fig. 2-3(d), in which similar phenomenon with Bi high resolution XPS was also observed. The Br 3d3/2 and 3d 5/2 peaks are situated at 68.2 and 69.2 eV [126]. The XPS analysis provides the solid evidence for synthesized $Bi_4O_5Br_2$ with the directing agent of PEG.

Table 2-2 BET surface area, pore volume and pore size of the obtained samples

		S_{BET} (m^2/g)	Pore volume (cm^3/g)	Pore size (nm)
With PEG-10000	pH=12	139.8	0.2	6.1
	pH=11	160.9	0.19	6.9
	pH=10	131.3	0.21	6.4
	pH=7	101.6	0.2	3.6
	pH=3	82.5	0.17	2.1
Without PEG-10000	pH=11	94.3	0.12	3.3
	pH=10	97.5	0.21	4.7
	pH=7	79.8	0.19	2.7
	pH=3	69.5	0.26	2.5

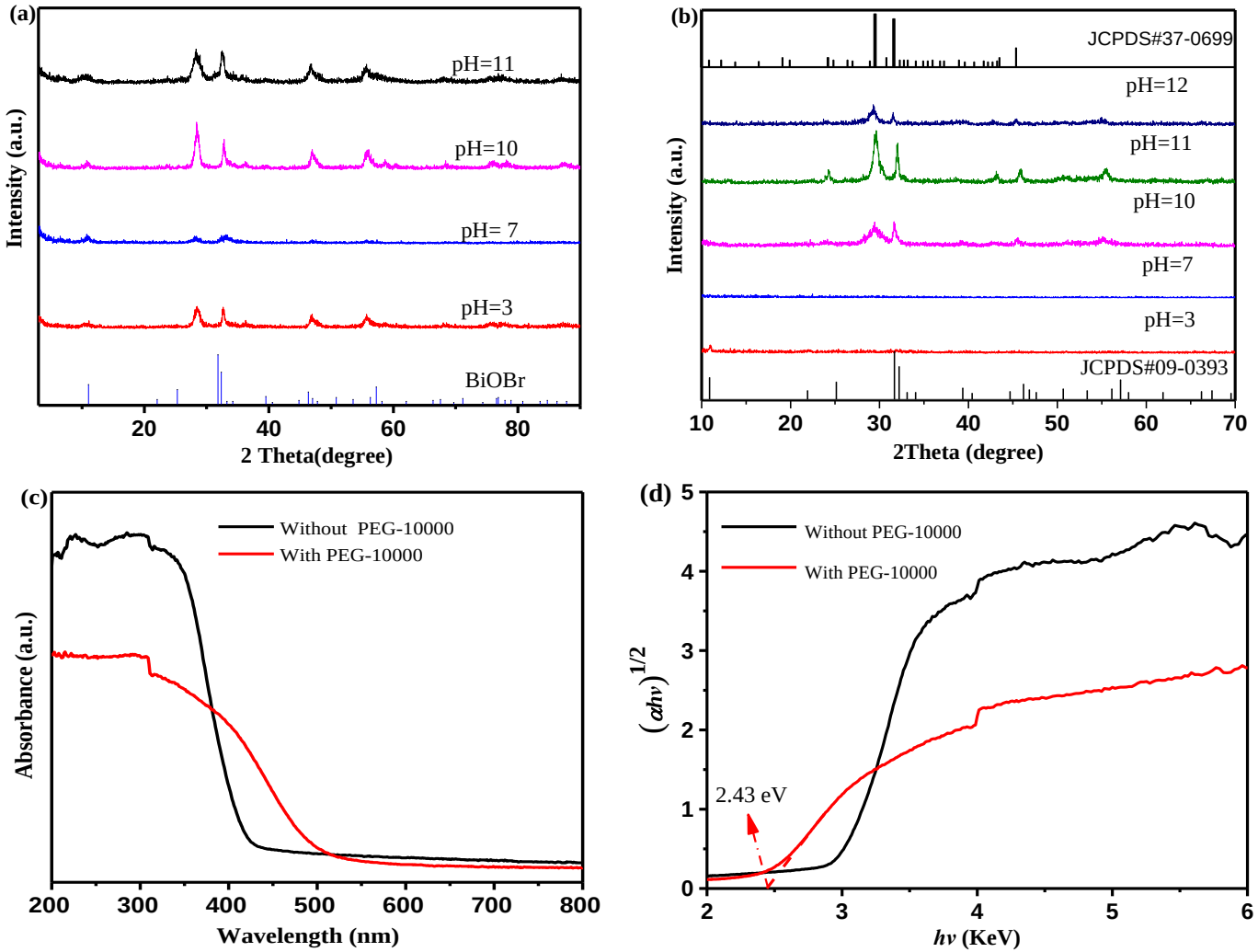

Fig. 2-1 The XRD patterns of synthesized samples without PEG-10000 (a) and with PEG-10000 (b) under different pH values; DRS (c), and $(\alpha hv)^{1/2}$ - (hv) curves (d) of samples at pH =11.

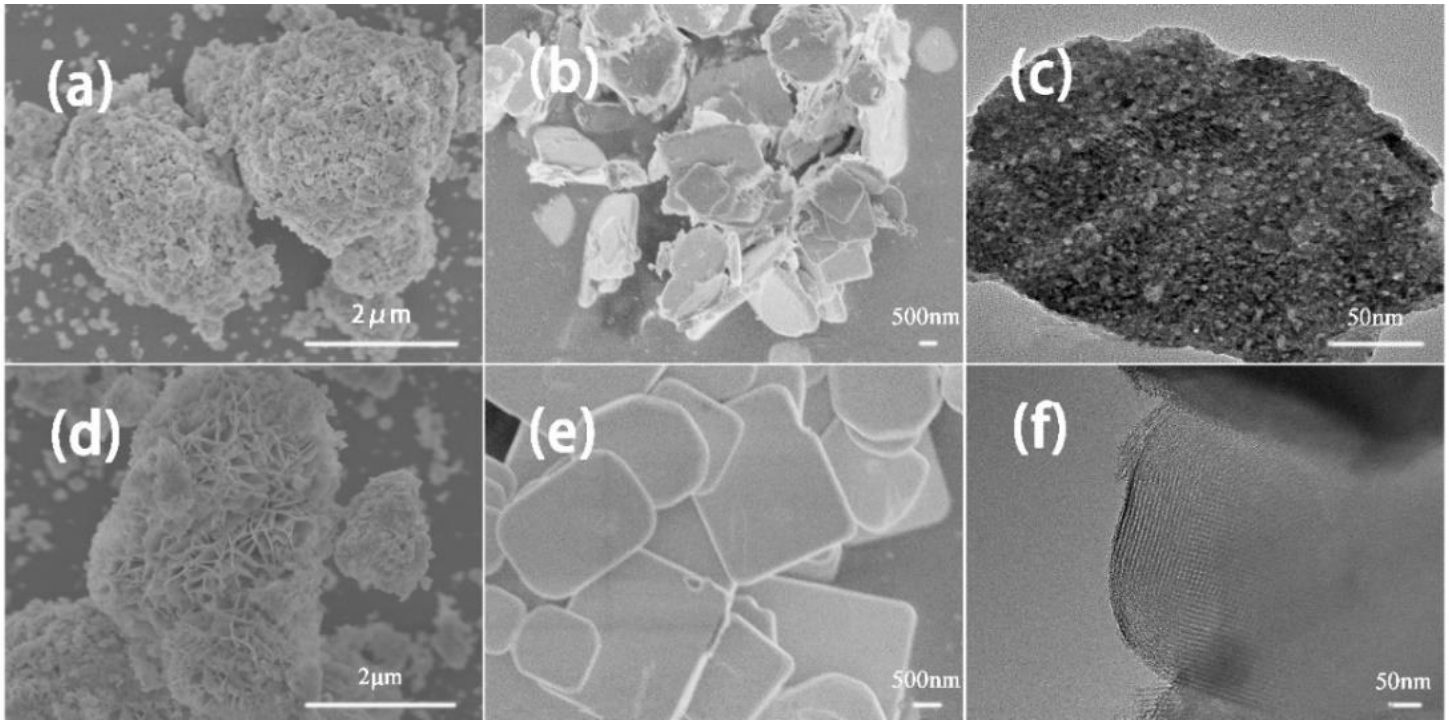

Fig. 2-2 SEM images of samples obtained under pH=11 without PEG-10000 (a, b) and with PEG-10000 (d, e); TEM images of samples without PEG-10000 (c), and with PEG-10000 (d).

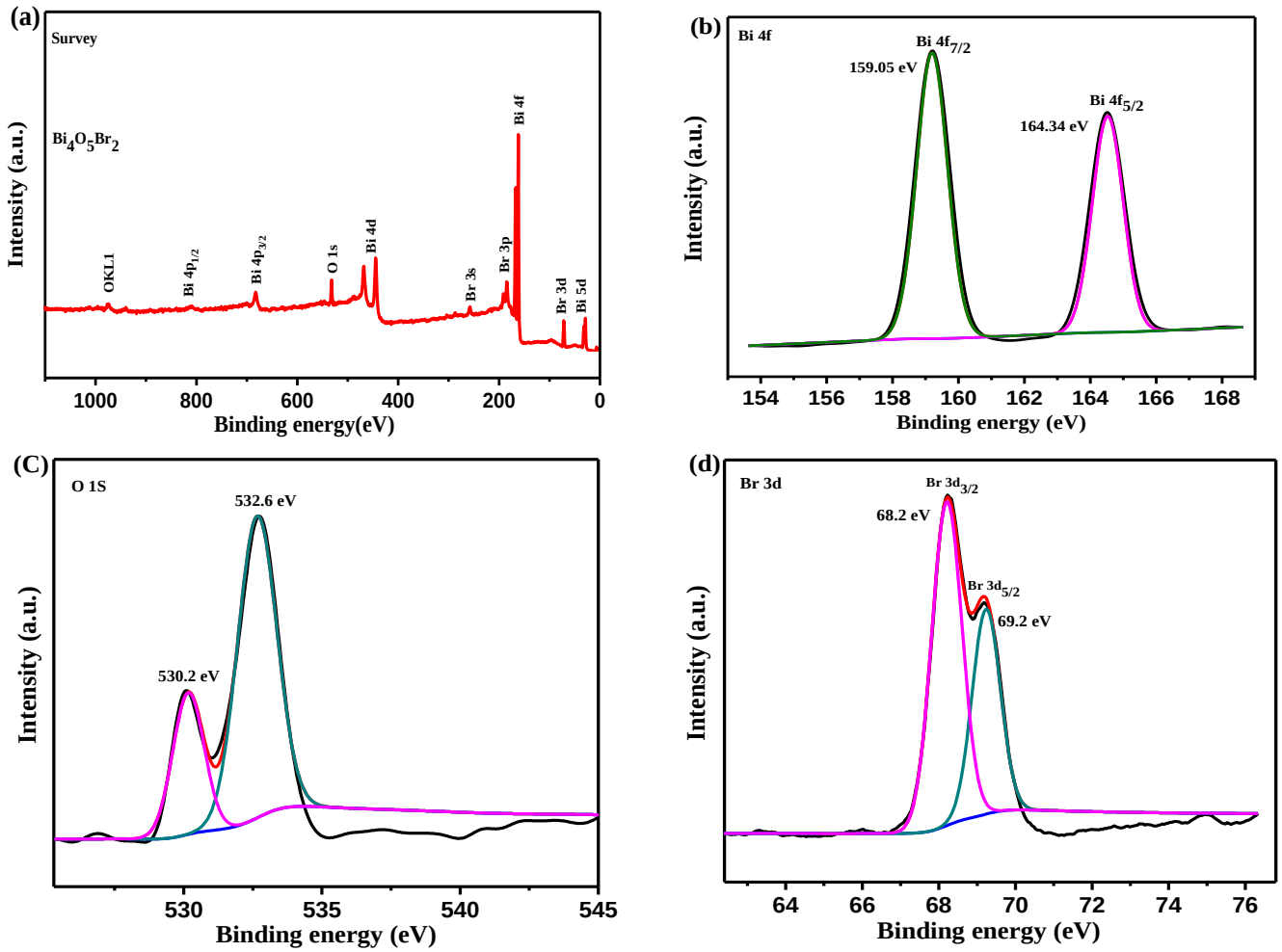

Fig. 2-3 XPS spectra of $Bi_4O_5Br_2$ samples (a), Bi 4f (b), O 1s (c) and Br 3d (d).

2.3.2 Evaluation on photocatalytic performance of $Bi_4O_5Br_2$ composites

Photocatalytic performance and stability of photocatalyst are important indexs in its practical application. Fig. 2-4 demonstrated that the $Bi_4O_5Br_2$ composite had better photocatalytic performance and stability. From Fig. 2-4(a), it showed thatthe RhB decoloration rate was about 80 % over the synthesized samples with PEG-10000 under pH=10, 11, and 12 synthesis conditions. All the samples with PEG-10000 obtained the better decoloration rate of RhB within 40 min compared with BiOBr at the same intial concentration of RhB solution. And the best decoloration rate on RhB was obtained within 25 min, and RhB can be completely decolored with the synthesized samples at pH=11. Interestingly, the synthesized sample with PEG-10000 at pH=12 existed the better absorption performance than that of BiOBr and the synthesized samples under pH=10 and 11, which indicates that the directing reagent would terminate the broken layer reaction and side reaction may occur in the synthesis system. Fig. 4(b) showed that the sample of the prepared $Bi_4O_5Br_2$ at pH=11 has good stability for RhB decoloration. Results showed high stability and photocatalytic activity with 5 time reusing $Bi_4O_5Br_2$ (pH=11), and about 99.40 % RhB was decolored. According to the formula (Eq. (2-2)):

$$- \ln (C/C_0) = kt \qquad (2\text{-}2)$$

the rate constants k was obtained by the function of $-\ln(C/C_0)$ and time, which indicating that the decoloration of RhB with new photocatalyst conformed to the quasi-first-order kinetics formula with the rate constant k values much higer than those of samples without PEG-10000 under the different pH conditions (Fig 2-4(c)). This phenomenon indicates that the prepared photocatalyst with PEG-10000 as directing agent have better photocatalytic performance.

The $Bi_4O_5Br_2$ catalyst was selected and different active species capture agents such as 2mmol isopropanol (IPA), 2mmol sodium oxalate(SO), 1mmol p-benzoquinone (BQ) were added to decolor RhB under visible light to further study the photocatalytic mechanism. Isopropanol can capture hydroxyl groups (•OH), sodium oxalate can capture holes (h^+), and p-benzoquinone can capture superoxide radicals ($•O_2^-$). It can be seen from Fig. 2-5(a), the photocatalytic performance was slightly decreased with sodium oxalate, which indicated that h^+ was not the active species during the photocatalytic reaction. However, the photocatalytic activity was greatly limited by adding isopropanol and benzoquinone, reflecting that the main active species were •OH and $•O_2^-$. Fig. 2-5(b) shows that photogenerated holes (h^+) have strong oxidant activity and can directly degrad organic contaminants.

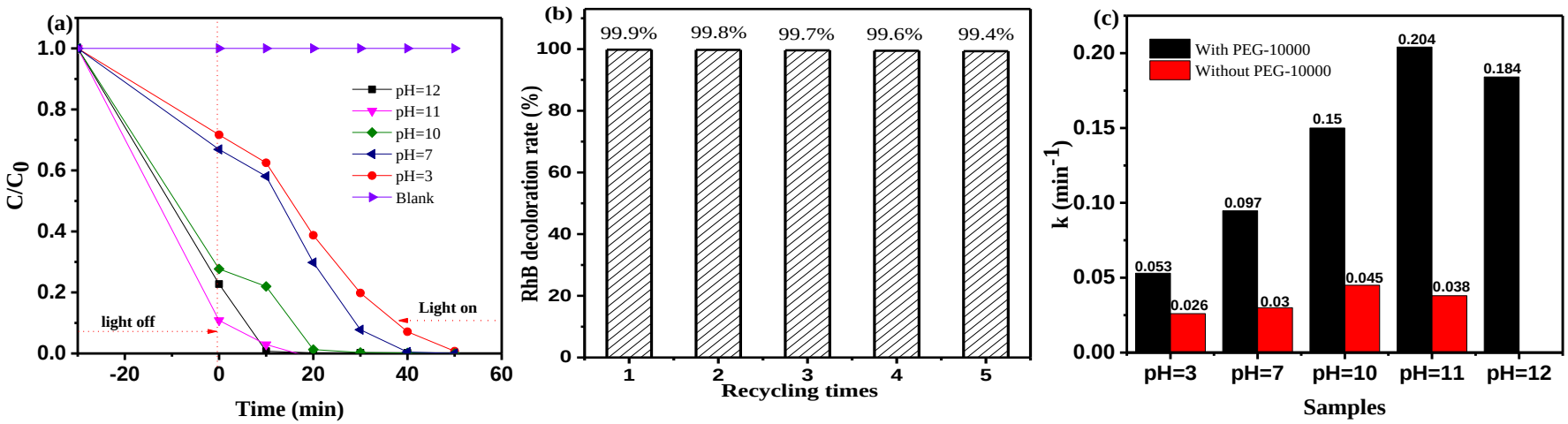

Fig. 2-4 RhB decoloration with the synthesized samples under different pH with PEG-10000 (a) and without PEG-10000 (b), and their reaction rate constant k (c).

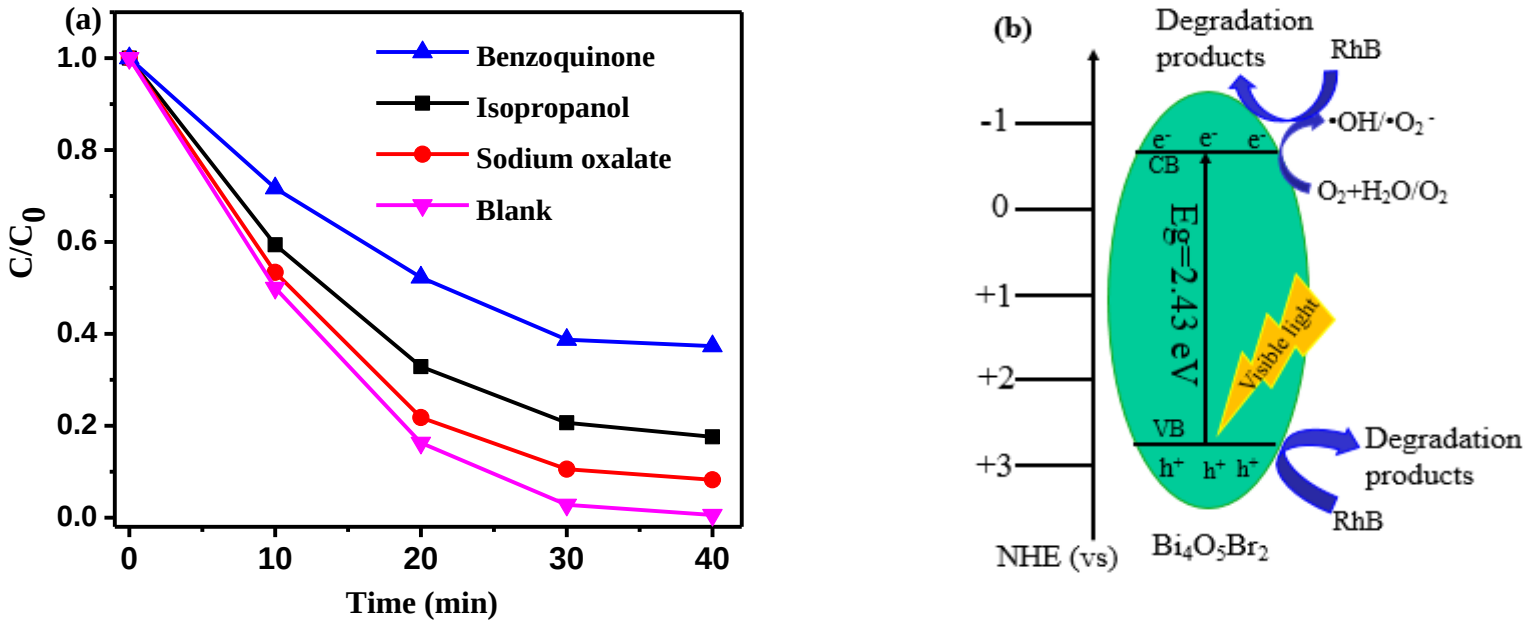

Fig. 2- 5 Photocatalytic activity of $Bi_4O_5Br_2$ under different scavengers (a) and Mechanism of RhB decolorization over$Bi_4O_5Br_2$ under visible light (b).

Photocurrent was characterized by analyzing the separation efficiency of e^- and h^+ (Fig. 2-6(a)). The higher density of photocurrent represents the higher separation efficiency. From Fig. 2-6(a), it showed that the density of photocurrent of $Bi_4O_5Br_2$ was much stronger than BiOBr, which indicating that $Bi_4O_5Br_2$have lower recomnination rate of e^- and h^+. The reason may be the heterojunction formed between Bi-O and BiOBr, or the SPR effect on elemental Bi and BiOBr. Therefore, the mechanism of single-phase photocatalyst $Bi_4O_5Br_2$ synthesis is inferred by adjusting the stoichiometric effect of bismuth atom and brominde atom to form bismuth-rich photocatalyst , which is consistent with the analysis of the photoluminescence spectrum (PL). In PL spectrum, the intensity of the peak spectra represents for the separation rate of photogenerated carriers. The intensity was the stronger, the recombination rate of photo-generated electron and hole pairs is lower, and the photocatalytic activity is weaker [127]. In order to analyze the photocatalytic activity of $Bi_4O_5Br_2$, the PL spectra of $Bi_4O_5Br_2$ and BiOBr were measured at 388 nm (Fig. 2-6(b)). From Fig. 2-6(b), BiOBr has a strong emission peak at 453 nm, while it has a lower peak spectra,confirmed that photocatalytic activity of $Bi_4O_5Br_2$ is stronger than BiOBr due to the photogenerated e^- and h^+ were effectively separated.

According to the $(\alpha h\nu)^{1/2}$ - $(h\nu)$ curve (Fig. 2-1(d)), Eg can be obtained at 2.43 eV. In order to further explore the mechanism of the decoloration of RhB by $Bi_4O_5Br_2$, the active species in the photocatalytic reaction were studied. Photogenerated electrons (e^-) reduce oxygen (O_2^-) dispersed in an aqueous solution to form superoxide radicals ($\bullet O_2^-$), which react with holes (h^+) to form •OOH radicals, which are finally decomposed into superoxide. This high efficiency of RhB decolorization can also be realized with high efficiency separation and by recycling the used $Bi_4O_5Br_2$ composite (Fig. 2-4(b)).

2.3.3 Evaluation of chromium removal by using $Bi_4O_5Br_2$ photocatalyst

As we know, Cr(VI) is very difficult to remove in the field of environmental control. How to realize the Cr(VI) transformation from the high toxicity to stable state is very meaningful for wastewater treatment. Fig. 2-7 explored that transformation of toxic Cr(VI) into stable Cr(III) could be realized by photoreduction under visble light. It can be seen that the obtained samples have good reduction performance for Cr(VI) photoreduction with the initial pH of solution at 7 (Fig. 2-7(a)). And the final transformation effort was obtained above 90% Cr(VI) reduction within 120 minunder visible light.

In order to further confirm the Cr transformation, XPS analysis was adopted to inverstgate the distribution on the used photocatalyst surfacewithCr2p spectra after photoreduction under

visible light. Fig. 2-7(c) showed the high energy spectrum had two energy bands at 577.24 eV and 586.51 eV, which were attributable to the binding energies of Cr 2p3/2 and Cr 2p1/2 orbitals , respectively. The Cr 2p1/2 spectrum was fitted to two peaks at about 587.29 eV and 586.15 eV. And the Cr 2p3/2 spectrum was fitted to two peaks at about 577.60 eV and 576.34 eV, which belonging to Cr(VI) and Cr(III), respectively. The co-existence of Cr(VI) and Cr(III) was contributed by the reduction of Cr(VI) with $Bi_4O_5Br_2$.

2.4 Summary

In this chapter, a highly active single-phase $Bi_4O_5Br_2$ photocatalyst was synthesized by using solvothermal method by adding polymer PEG-10000 into the mixed solvent as directing agent and adjusting the alkalinity. The synthesized $Bi_4O_5Br_2$ was confirmed to be an excellent photocatlyst with multiple facets, dimensional flow-like nanosheets structure.and high visible light responsiveness. Compared with BiOBr, the new photocatalyst had good photocatalytic activity and lower combination rate of photogenrated electron and hole pairs. The result of RhB decoloration showed that 100% of RhB decoloration with synthesized composite within 40 min under visible light, which can also be recycled and reused for highly efficient decolorization. In addition, Above 90 % toxic Cr(VI) was reducted into stable Cr(VI) over the obtained samples within 120 min under visible light. The $Bi_4O_5Br_2$ composite was co-catalyst with a great potential for practical application in wastewater treatment.

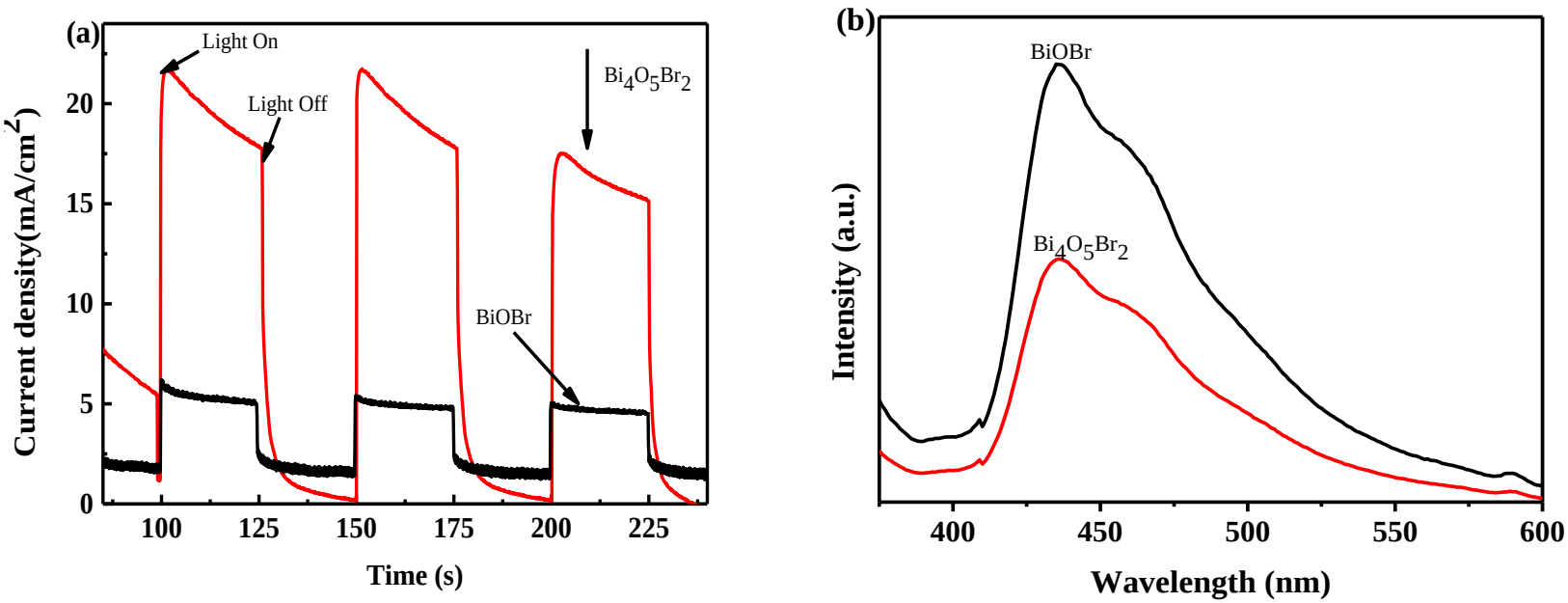

Fig. 2-6 Photocurrent responsiveness of (a) and PL spectra (b) of samples

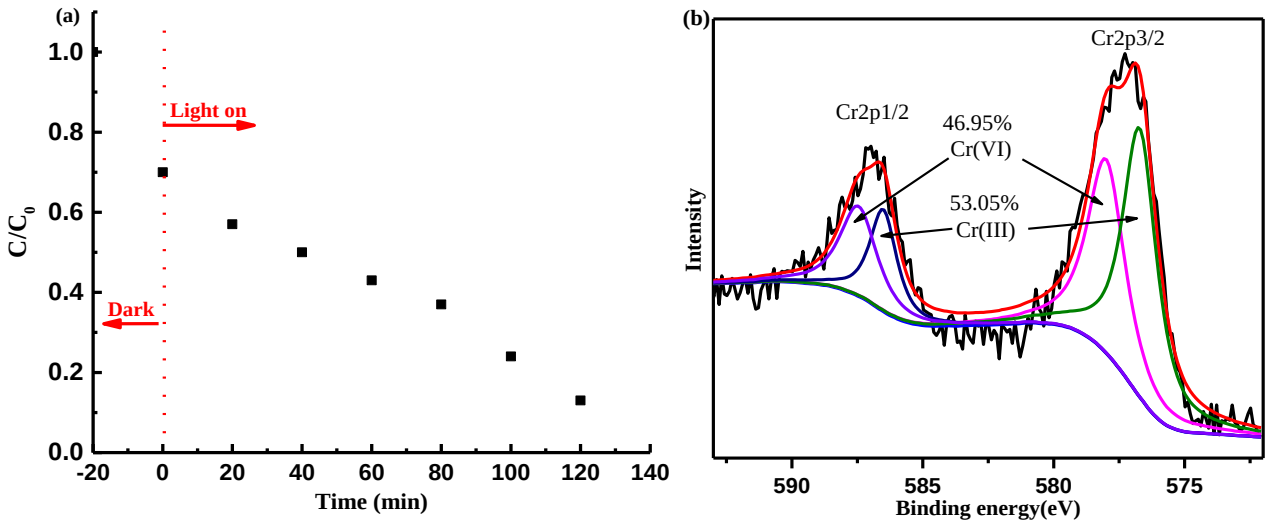

Fig. 2-7 Cr(VI) removal (a) and (b) Cr distribution on the obtained sample at pH=11 by XPS

Chapter 3 Fabriction of $Bi_4O_5Br_2$/SBA-15 material and its application in wastewater treatment

3.1 Introduction

In Chapter 2, single-phase photocatalyst $Bi_4O_5Br_2$ was investigated, which existed special facets structure andgood visible light catalytic activity, however, single-phase $Bi_4O_5Br_2$ also has some drawbacks such as poor thermal stabilityand easy agglomeration in t practical application in wastewater treatment, which has a direct effect on the active sites during the photoreduction and photooxidation process. In order to solve the above problems, the excellent supports was necessary for single-phase $Bi_4O_5Br_2$ modification.SBA-15 is a kind of silicon-based molecular sieves with self-ordered mesoporous material, uniform pore size, large pore structure, high surface area and good stability in acid and alkaline conditions [128, 129], which was considers as an ideal carriers for single-phase photocatalyst loading on the surface to enhance the active sites contact during the photocatalytic processing In addition, no report was found on loading single-phase $Bi_4O_5Br_2$ semiconductor on SBA-15 carriers to enhance the photocatalytic performance of composite photocatalysts. Moreover, after loading $Bi_4O_5Br_2$ on SBA-15, the photoelectron migration on the surface of the photocatalyst and the recombination rate of photogenerated electrons and holes have not been studied yet.

Ammonium is a typical pollutant in aquatic resource, which easily causing water eutrophication, and high concentration of ammonium in water will be a threat for human health and ecological environment [138]. In the past time, ammonium removal was reported by SBA-15, which foucused on the adsorption capacity. However, there was no report on the ammonium removal over the photocatalyst with SBA-15 as a support. In Chapter 2, Cr(VI) could be detoxicification over the $Bi_4O_5Br_2$ under visble light The new strategy of loading single-phase photocatalyst on SBA-15 was designed. However, whether the synthesized catalyst has the performance of the co-catalyst still need to further verification.In this chapter, hydrothermal synthesis method was used to generate the $Bi_4O_5Br_2$/SBA-15 photocatalytic materials, i.e. $Bi_4O_5Br_2$ was grafted onto the surface of SBA-15. The morphology, XRD phase, optical properties and photocatalytic activity of $Bi_4O_5Br_2$/SBA-15 were characterized by XRD, BET, TEM, XPS, DRS and other methods. While Rhodamine B (RhB), Cr(VI) and ammonium was used as target contaminants, the different decolorization capacities, photoreduction and adsorption capacity of the synthesized photocatalysts (obtained under different loading ratios

of $Bi_4O_5Br_2$/SBA-15) were investigated under visible light. At the same time, the photocatalysis stability and reusability of the newly synthesized

3.2 Material and methods

3.2.1 Synthesis of mesoporous $Bi_4O_5Br_2$/SBA-15composite

$Bi_4O_5Br_2$/SBA-15 was prepared through the following two steps. The first step was to synthesize $Bi_4O_5Br_2$ with solvothermal method. The synthesis method was the same as Chapter 2.when the synthesis condition ofpH value was adjucted to 11.

In the second step, $Bi_4O_5Br_2$/SBA-15 was synthesized by sol-gel method. In a typical run, 2.0 g polyether P_{123} (PEO-PPO-PEO) was added into 65 mL deionized water at ambient temperature under mechanical stirring for 3 h. 10 ml HCl (2 mol/L) was then dropped into the above mixture at 40 ℃ with stirring for 1 h. $Bi_4O_5Br_2$ was mixed with the above system with different mass ratios of Bi/SiO_2 of 20/100, 30/100, 40/100, and 50/100. After stirring for 1 hour, 4.5 g tetraethyl orthosilicate (TEOS) was slowly dropped into the mixture system at 40 ℃ with stirring for 24 h. The synthesis system was later solvothermally treated at 140 ℃ for 24 h. The solids was centrifuged, washed, and dried at 60 ℃ for 8 h. The samples were calcined at 550 ℃ in air atmosphere for 6 h, which were named as Bi_{20}/SBA-15, Bi_{30}/SBA-15, Bi_{40}/SBA-15, and Bi_{50}/SBA-15, respectively.

3.2.2 Characterization and evaluation of photocatalytic performance

In this part, the synthesized photocatalysts was analysized from morphology, XRD patterns, optical property and photocatalytic performance. The characterization methods for morphology, XRD, optical property were similar to Chapter 2 (2.2.2).The evaluation of photocatalytic performance for the synthesized photocatalysts was carried out using the same methods as in Chapter 2 (2.2.3 and 2.2.4). The application experiment for chromium detoxicitation was done as in Chapter 2 (2.2.5).

3.2.3 Evaluation of Ammonium removal experiment

Ammonium stock solution (500 mg/L) was prepared by dissolving NH_4Cl in 0.5 L deionized water. The working concentrations were prepared from this stock solution by deionized water. 100 mg/L of NH_4Cl solution was selected to analysize the removal rate of the obtained $Bi_4O_5Br_2$/SBA-15 photocatalyst. Firstly, NH_4Cl solution reached adsorption equilibrium with stirring in dark for 30 min, and then the solution was irradiated by A 300 W

xenon lamp with a 420 nm cut-off filter provided visible light irradiation. Then, the residual solution of NH_4Cl was collected with 0.2 m L H_2O_2 during the time intervals and NH_4Cl solution was centrifuged (10 000 rpm, 10 min) to remove the photocatalysts as fast as possible. The concentration of NH_4Cl was determined with Nessler's reagent by 725N UV-vis spectrophotometer (Beijing Purkinje General Instrument Co., Ltd.). 0.2 g/L new photocatalyst was added into simulated wastewater to test the photocatalytic performance all the tests.

3.3 Results and discussion

3.3.1 Characterization of $Bi_4O_5Br_2$/SBA-15 composites

The crystalline facet is a key factor for its photocatalytic perfprmance.The XRD phase was investigeted on the crystallinezation of the new synthesized materials.From Fig. 3-1(a), the small angle XRD pattern of SBA-15 with different loading ratio of $Bi_4O_5Br_2$ was determined. A strong diffraction peak (2θ=0.90° to 1.0°) and two weak diffraction peaks (2θ=1.3° to 1.8°) in the range of small angle (2θ=0.3° to 5°) were produced in all the synthesized samples.These characteristic peaks are coincident with the crystal plane diffraction peaks of (100), (110), and (200) in the two-dimensional hexagonal structure of SBA-15, respectively,which attributes to the presence of a typical two-dimensional hexagonal,silicon crystal facets and ordered mesoporous structure [130]. And this phenomenon indicates that the single phase photocatalyst $Bi_4O_5Br_2$ did not change the mesoporous structure of SBA-15 during the synthesis process. As we can see, the diffraction peaks is shifted to higher angles from Bi_{20}/SBA-15 to Bi_{50}/SBA-15, confirming that the pore capacity and diameters gradually decrease along with the increase of loading ratio, and the largest pore diameter was abbtained when the mass ratio of Bi/SiO_2 reached to 20:100 [131]. Interestingly, the diffraction peak intensity was first increased and then decreased, and the highest intensity of diffraction peak was occurred with the mass ratio of Bi/SiO_2 reached to 30:100. This results explored that the mesoporous structure of the synthesized Bi_{30}/SBA-15 was the most regular among the synthesized samples. The high intensity of peaks was attributable to the Bi atom which was incorporated into the mesoporous silica matrix, creating a new crystal facets on mesoporous structure [132]. This phenomenon provided an useful information on Bi distribution on the surface of SBA-15. Fig. 3-1(b) shows the wide angle XRD patterns of the synthesized $Bi_4O_5Br_2$/SBA-15 samples. As seen, all the samples had similar characteristic peaks, and the corresponding positions of the characteristic peaks were 11.2 °, 25.0 °, 31.5 °, 39.2 °, 46.2 °, 53.5 °, 57.2 °, 67.1 °, and 76.0 °, respectively. These

peaks reprent for the tetragonal phase of $Bi_4O_5Br_2$ (standard card JCPDS No. 09-0699), which coincide with the corresponding crystal planes of $Bi_4O_5Br_2$ (001), (011), (012), (110), (112), (020), (211), (220), and (130), respectively. Especially, the strongest diffraction peak intensity was obtained at 31.5 °, indicating that the synthesized photocatalyst also exists the (012) crystal plane like single phase tetragonal $Bi_4O_5Br_2$ photocatalyst.

Table 3-1 shows the specific surface area, the pore volume and the average pore size of thesynthesized photocatalysts. The pore diameters of Bi_{20}/SBA-15, Bi_{30}/SBA-15, Bi_{40}/SBA-15, and Bi_{50}/SBA-15 firstly increased and then decreased. This variation trend was consistent with the results of the small angle XRD of synthesized samples. With the increase of $Bi_4O_5Br_2$ loading ratio, both the specific surface area and pore volume of the synthesized photocatalysts showed a decreasing trend with the increase of single phase $Bi_4O_5Br_2$ loading, which indicating that the aggregation of single phase photocatalyst may bring about the increase of the relatively size of $Bi_4O_5Br_2$ particles during synthsis process, therefore, the pores of SBA-15 was easily blocked. This phenomenon implied that the effect of synthesis material on pollutants removal and the adsorption capacity of $Bi_4O_5Br_2$ /SBA-15 might gradually decrease when compared to SBA-15 [133]. Fig. 3-2 illustrates the nitrogen sorption-desorption isotherm curves of the synthesized composites. From this figure, it can be seen that the Langmuir type IV hysteresis loops occurred in all the curves, which confirmed that the synthesized samples (Bi_{20}/SBA-15, Bi_{30}/SBA-15, Bi_{40}/SBA-15, and Bi_{50}/SBA-15) had the ordered mesoporous structure .The morphology of SBA-15, $Bi_4O_5Br_2$, and $Bi_4O_5Br_2$/SBA-15 were detected by the SEM and TEM images in (Fig. 3-3). As seen from Fig. 3-3(a), the image of pure mesoporous material SBA-15 clearly existed well-ordered mesoporous hexagonal arrays and one-dimensional channels of the mesoporous structure (with a diameter of 7.3 nm). The results demonstrated the high ordered level obtained from silica synthesis and confirmed the pore size distribution [134]. Fig. 3-3(b) and 3e showed the morphology of $Bi_4O_5Br_2$ with special nanosheets structure and crystalline facets. No diffraction spots or diffraction rings were observed in Fig. 3-3(d), revealing the amorphous silica characteristics of SBA-15. Fig. 3-3(c) and 3-3(f) shows the images of Bi_{30}/SBA-15 sample. Smaller particles were grafted on the surface of larger particles SBA-15 in all the images.These agglomerations of nanoparticles were mainly in the range of 100 nm. This observation is consistent with the $Bi_4O_5Br_2$ phase from the XRD patterns. However, as it can be seen from Fig. 3-3(c) and 3-3(f), $Bi_4O_5Br_2$ as rods or spheres were distributed on the surface of the SBA-15. Fig. 3-3(c) and 3-3(f) also shows that $Bi_4O_5Br_2$ might be chemically bonded to the surface of SBA-15, not simply loaded on the surface, which may produce stable

photocatalytic components thus exhibit photocatalytic activity, thereby increase the possibility of recirculation of the photocatalytic material.

In order to study the elemental composition and valence state of the photocatalytic materials, XPS analysis of Bi_{30}/SBA-15 was performed (Fig. 3-4). The XPS spectrum of Bi_{30}/SBA-15 confirmed the existence of Si, C, O, Bi, and Br elements. The appearance of element C may be caused by CO_2 from the sample absorption of air during the analysis [135]. In Fig. 3-4(b)**,** the peak at 103.6 eV was corresponding to Si 2p spectrum, which was the characteristic peak of Si-O-Si band in SiO_2 of SBA-15 and the characteristic peak of Si^{4+} [136-138]. A high resolution energy spectrum of O 1s with two main peaks (Fig. 3-4(c)), 530.6 and 533.0 eV, respectively, was obtained. The main peak 530.6 eV was attributed to the lattice oxygen of Bi-O bond in $[Bi_2O_2]^{2+}$ in the layered $Bi_4O_5Br_2$/SBA-15, while the peak at 533.0 eV was chemisorbed oxygen and OH^- adsorbed on the surface of the material [139]. The Bi 4f spectrum displayed in Fig. 3-4(d) contains two peaks at binding energy of 159.4 and 164.8 eV, which belonged to Bi 4f7/2 and 4f5/2 [140, 141]. Fig. 3-4(e) shows that the high-resolution energy spectrum was confirmed to be Br 3d. As its two partial peaks were 68.4 and 69.5 eV [61, 62,137], respectively, and the corresponding spectra were 3d5/2 and 3d3/2, its valence was -1. Results of the XPS spectra indicated that the measured elements corresponded to the elements in the synthesized samples.

Fig. 3-5 shows the UV-vis DRS of $Bi_4O_5Br_2$/SBA-15 at different loading ratio of the two major materials. As seen, all the samples had a certain absorption under UV light and the absorption efficiency of Bi_{20}/SBA-15 was the highest. As shown in Fig. 3-5(a), all the composite samples exhibited significant absorption side bands in the visible light range around 410, 415, 430, and 435 nm, respectively. In addition, with the increase of the loading ratio, the absorption wavelength of visible light by the photocatalytic material was red-shifted, and the light response range was expanded. Among them, the band gap of Bi_{50}/SBA-15 was determined to be the narrowest, resulting in the highest utilization rate of visible light. This could be further analyzed by using the Kubelka-Munk formula (Eq. 2-1) [124]. The band gap energy spectra of different samples were obtained (Fig. 3-5(b)). It can be seen from Fig. 5(b) that the band gap energy of the samples decreased from about 3.30 eV to 3.10 eV with the increase of $Bi_4O_5Br_2$ loading ratio, and this may be caused by the agglomeration of nanoparticles [132].

3.3.2 Evaluation on photocatalytic performance

Fig. 3-6(a) demonstrates the photodegradation curves and degradation curves for Bi_{20}/SBA-15, Bi_{30}/SBA-15, Bi_{40}/SBA-15, and Bi_{50}/SBA-15 at 25 ℃, respectively. The abscissa was the

reaction time for dark adsorption and photodegradation, and the ordinate was the concentration of RhB remained. From Fig 3-6(a), it can be seen that the $Bi_4O_5Br_2$ at different loading ratio possessed strong absorption capacity for RhB, which could remove RhB from 30% to 65% within 1h of adsorption in dark, following a descending order of Bi_{30}/SBA-15 > Bi_{20}/SBA-15 > Bi_{40}/SBA-15>Bi_{50}/SBA-15. The residual RhB in solution was decolorated by photodegradation under visible light. During the whole reaction process, the removal of RhB with Bi_{30}/SBA-15 was the fastest. Although the band gaps of Bi_{50}/SBA-15 and Bi_{40}/SBA-15 were narrower than that of Bi_{30}/SBA-15, the RhB removal rates for Bi_{50}/SBA-15 and Bi_{40}/SBA-15 were lower than that for Bi_{30}/SBA-15. It might be the structure of SBA-15 was destroyed with big size nanoparticles which blocked the pores for adsorption of RhB onto the surface of SBA-15. Fig. 3-6(b) shows the fluorescence spectra of synthesized materials at different loading ratio of $Bi_4O_5Br_2$. The test was conducted at room temperature with the excitation wavelength of 250 nm. It can be seen that the peak shapes and positions of the four samples are similar, with the largest peak around 432 nm and another two weak peaks, indicating that the $Bi_4O_5Br_2$/SBA-15 was excited at 432 nm by the sunlight with the occurrence of electronic transitions and generation of photogenerated electron-hole pairs. Photoluminescence spectroscopy is an important approach to characterize the photoelectron-hole recombination rate of photocatalysts. The recombination rate of photoelectron-holes is proportional to the light intensity. Therefore, the photogenerated electron-holes of photocatalysts can be compared by using the light intensities. The light intensity of Bi_{50}/SBA-15 was the largest, followed by Bi_{40}/SBA-15, Bi_{30}/SBA-15, and Bi_{20}/SBA-15. The separation effect of Bi_{30}/SBA-15 was relatively high, which might be the major reason for its better photocatalytic effect than others. The reason was that the active sites were present inside and outside the SBA-15, which first increased with the increase of $Bi_4O_5Br_2$ loading, indicating the separation rate of electron and hole was enhanced, and then decreased, showing that the active sites decreased with the excess loading of nanoparticles of $Bi_4O_5Br_2$.

3.3.3 Active species analysis

$Bi_4O_5Br_2$ is a lamellar structure composed of a $[Bi_2O_2]^+$ layer and a double Br-layer interlaced, with an internal electrostatic field established between the layers. When a semiconductor was excited under visible light irradiation, photocurrent would produce and then the photoelectrons move in a fixed direction. A stronger photocurrent would bring more effective separation of electron-holes and higher photocatalytic performance of the

semiconductor as well. In the photocatalytic decolorization of RhB, the capture agents SO, IPA and p-BQ were individually added to capture the active species h^+, •OH and •O_2^- (Fig.3-7(a)). As shown in Fig. 3-7(a), the photocatalytic activity of Bi_{30}/SBA-15 slightly decreased when the capture agent IPA existed in the solution. In the case of capture agent p-BQ, the photocatalytic activity of the synthesized photocatalyst was significantly reduced after its addition in the photocatalytic process. However, when adding SO into the RhB solution, the photocatalyst showed almost no effect on the decolorization of RhB solution, implying the catalytic activity was significantly inhibited. The result indicated that h^+ played the main role in RhB decoloration under visible light.

For evaluation on the stability of the photocatalytic activity of the prepared $Bi_4O_5Br_2$/SBA-15, sample Bi_{30}/SBA-15 was applied to decolorize RhB for 5 times (Fig. 3-7(b)). Results showed that after 5 cycles of reutilization of Bi_{30}/SBA-15, its photocatalytic activity remained almost unchanged, and about 99.42% RhB was decolorized.

3.3.4 Evaluation of chromium photoreduction

Cr(VI) is a typical pollutant with unstable valence and high toxicity in wastewater. It is very difficult to remove from the wastewater. In this study, The photoreduction capacity of synthesized photocatalysts for Cr(VI) transformation was evaluated under visible light. Fig. 3-8(a) shows that Cr(VI) was photoreduced into Cr(III) under visible light. The figure also shows that the absorption ability of the new synthesized $Bi_4O_5Br_2$/SBA-15 photocatalysts for Cr(VI) was decreased with the increase of $Bi_4O_5Br_2$ loading within 30 min dark at an initial pH7, and Bi_{20}/SBA-15 obtaided the best absorption effect on Cr(VI) with 35% removal rate during dark reaction, indicating that the suitable mass ratio of Bi/SiO_2 is a key factor for Cr(VI) reduction. Excess mass ratio of Bi/SiO_2 may cause $Bi_4O_5Br_2$ agglomerate to form the big particles and blocked the porous structure (Fig. 3-8(a)). 100% Cr(VI) was photoruducted in the solution by using Bi_{30}/SBA-15 within 120 min at the initial pH=7. From Fig. 3-8(b), the Cr distribution shows the same enery spectrum of Cr2p by XPS as Chapter 2. The result demonstrated that the existence of Cr(VI) and Cr(III) on the surface of photocatalyst, which was attributable to the reduction of Cr(VI) with Bi_{30}/SBA-15.

Table 3-1 Surface area, pore volume and average pore size of the synthesized masterials

Samples	Specific area (m^2/g)	Pore volume (cm^3/g)	Average diameter (nm)
Bi_{20}/SBA-15	156	0.26	6.6
Bi_{30}/SBA-15	84	0.16	6.5
Bi_{40}/SBA-15	62	0.11	6.3
Bi_{50}/SBA-15	51	0.10	6.0

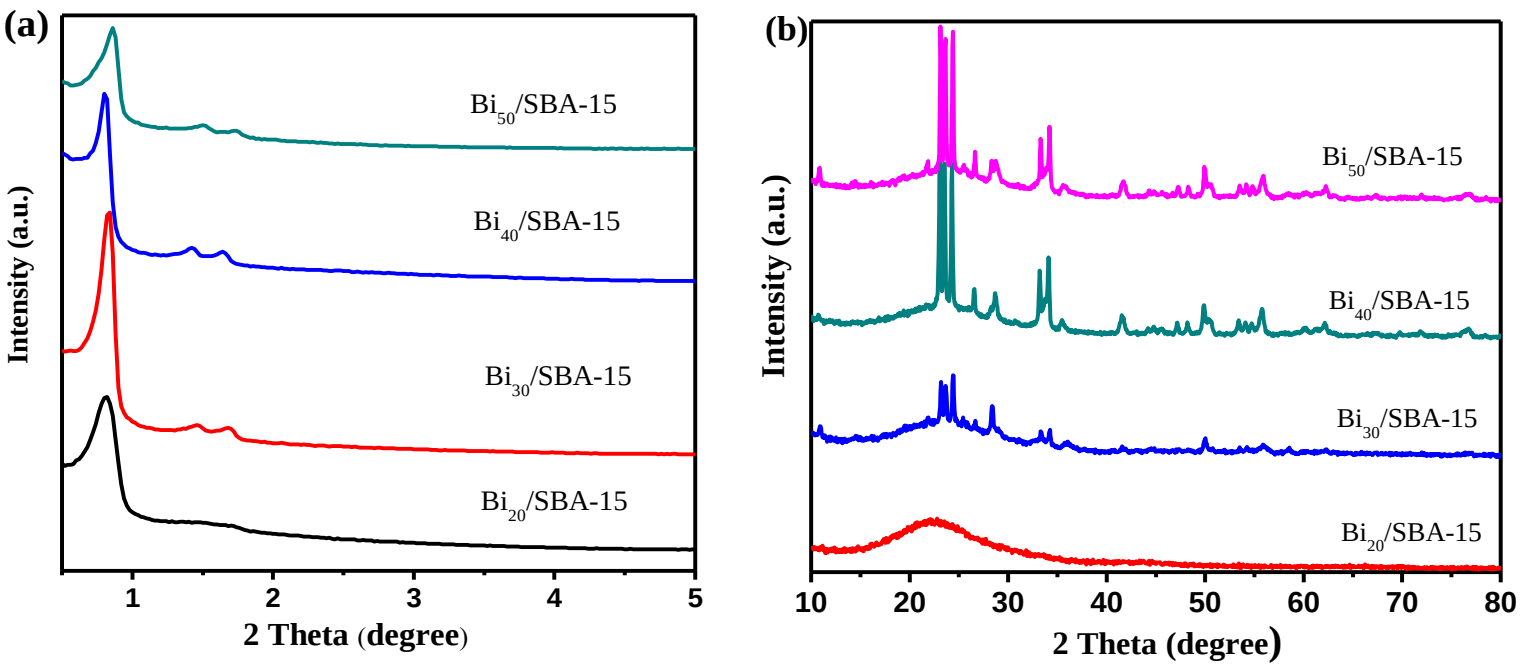

Fig. 3-1 Small angle XRD (a) and wide-angle XRD (b) of the synthesized materials

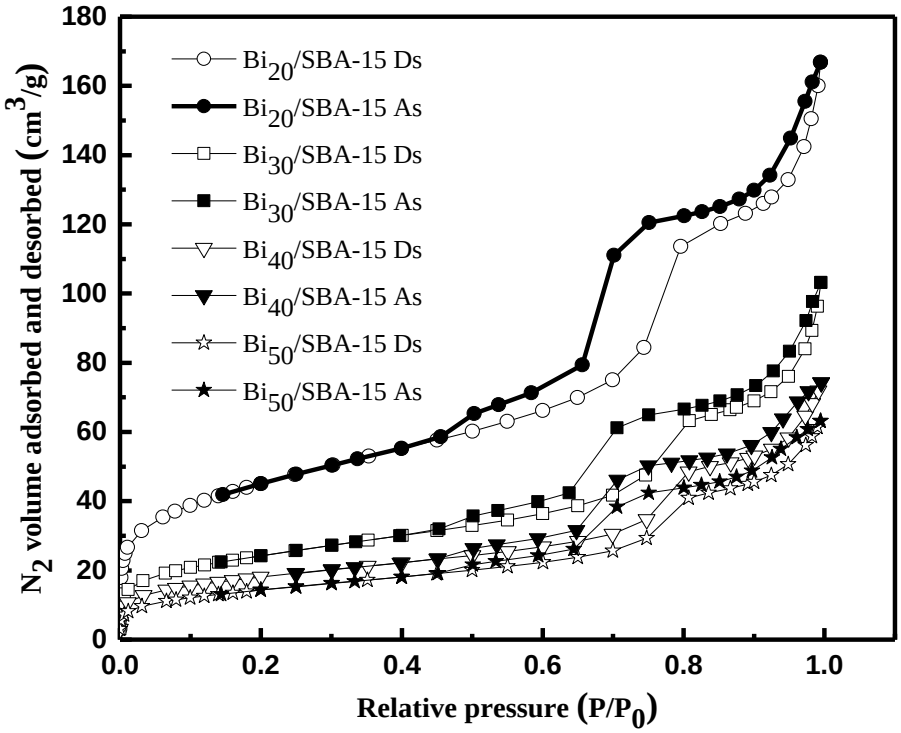

Fig. 3-2 Nitrogen adsorption-desorption isotherms of the samples (Notes: Ds and As were adsorbed and desorbed abbreviation)

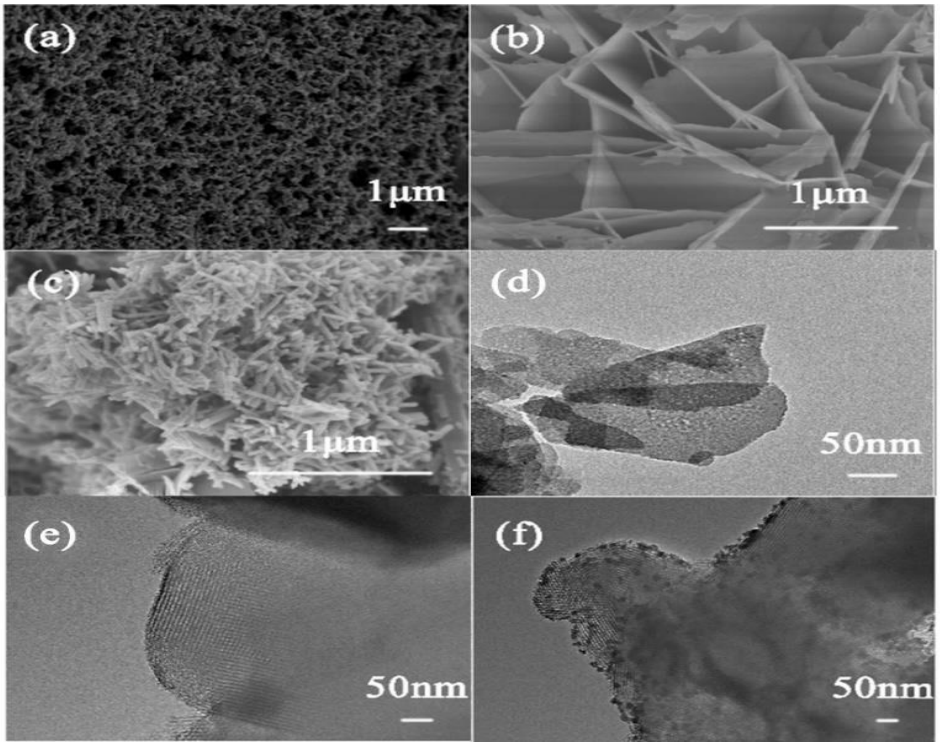

Fig. 3-3 SEM and TEM images of SBA-15 (a,d), $Bi_4O_5Br_2$ (b, e), and $Bi_4O_5Br_2$/SBA-15(c, f)

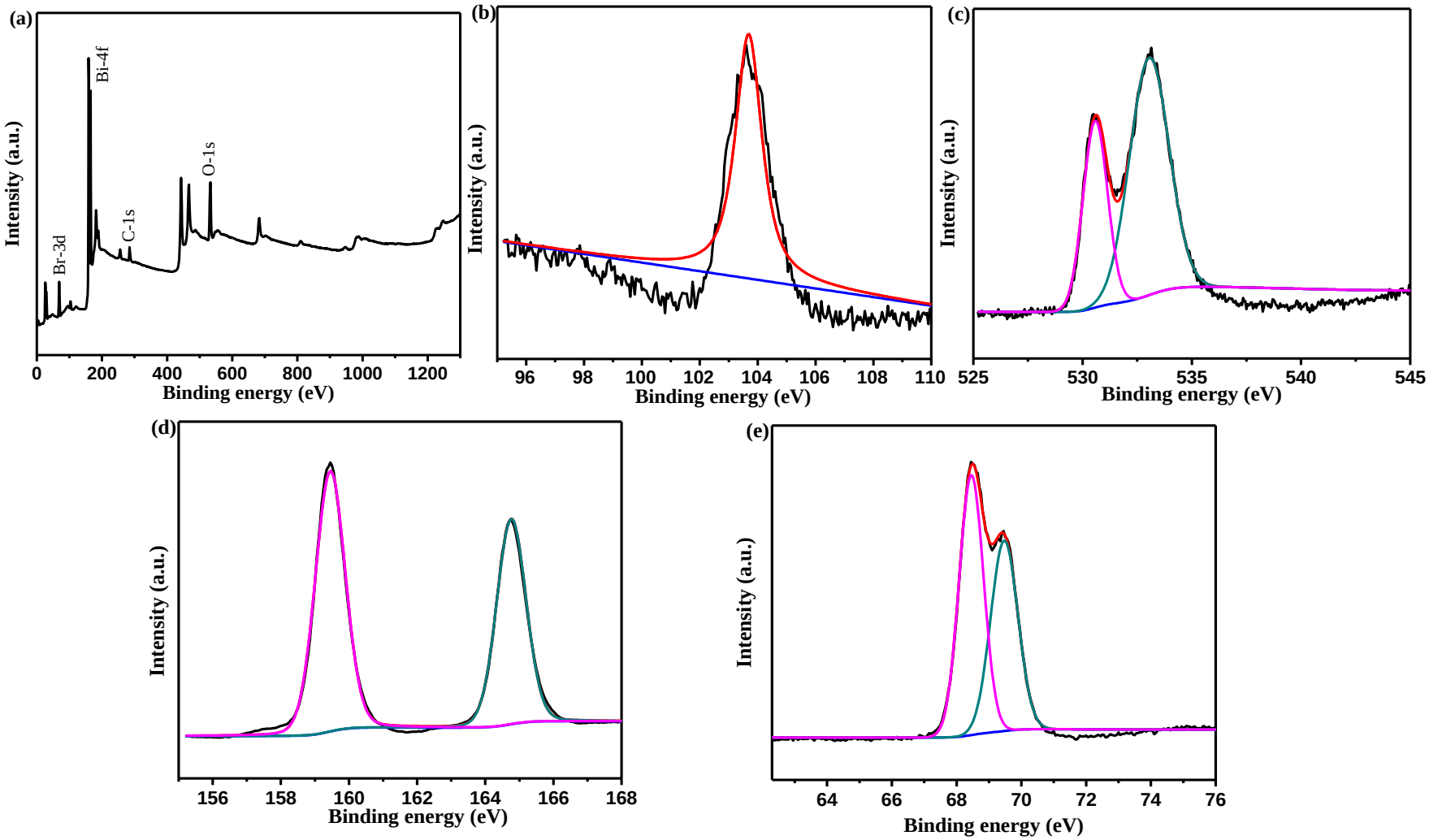

Fig. 3-4 XPS spectra of Bi_2/SBA-15: full spectrum (a), Si 2p(b), O 1s(c), Bi 4f (d), and Br 3d (e)

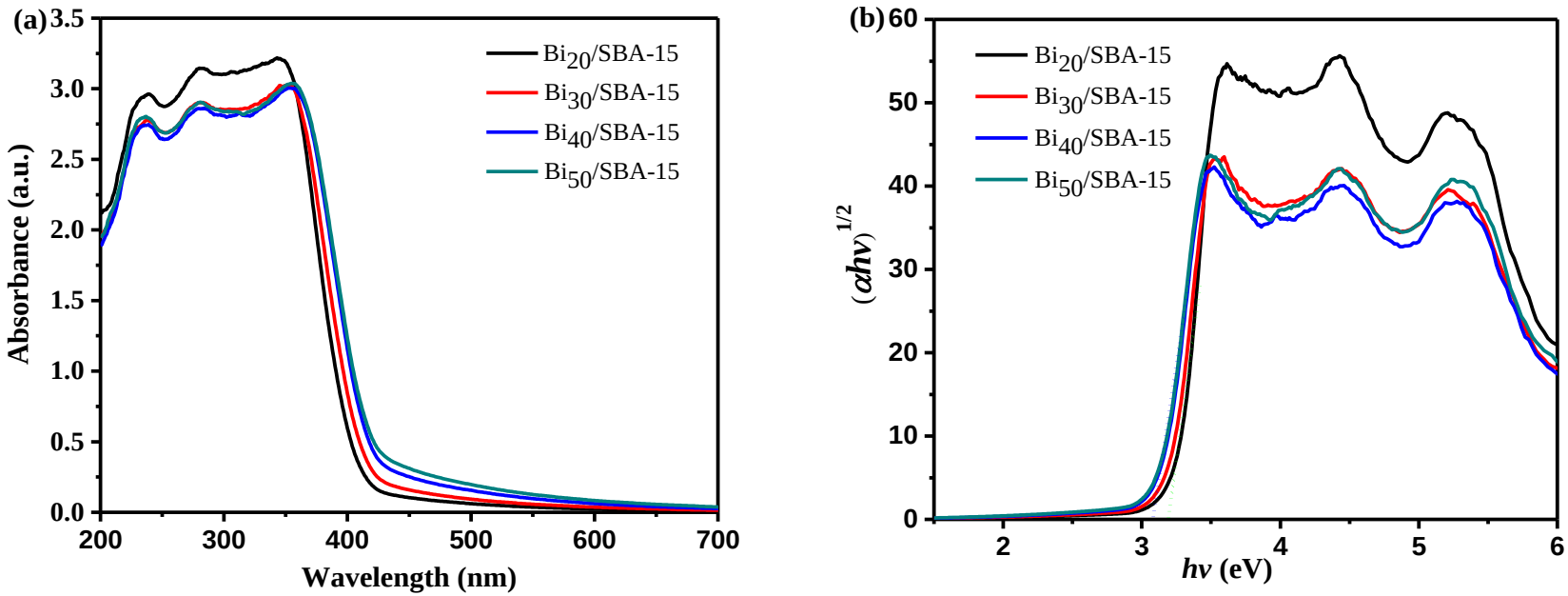

Fig. 3-5 UV-vis absorption spectrogram (a) and $(\alpha h\nu)^{1/2}$ -($h\nu$) curves (b) for different synthesized materials

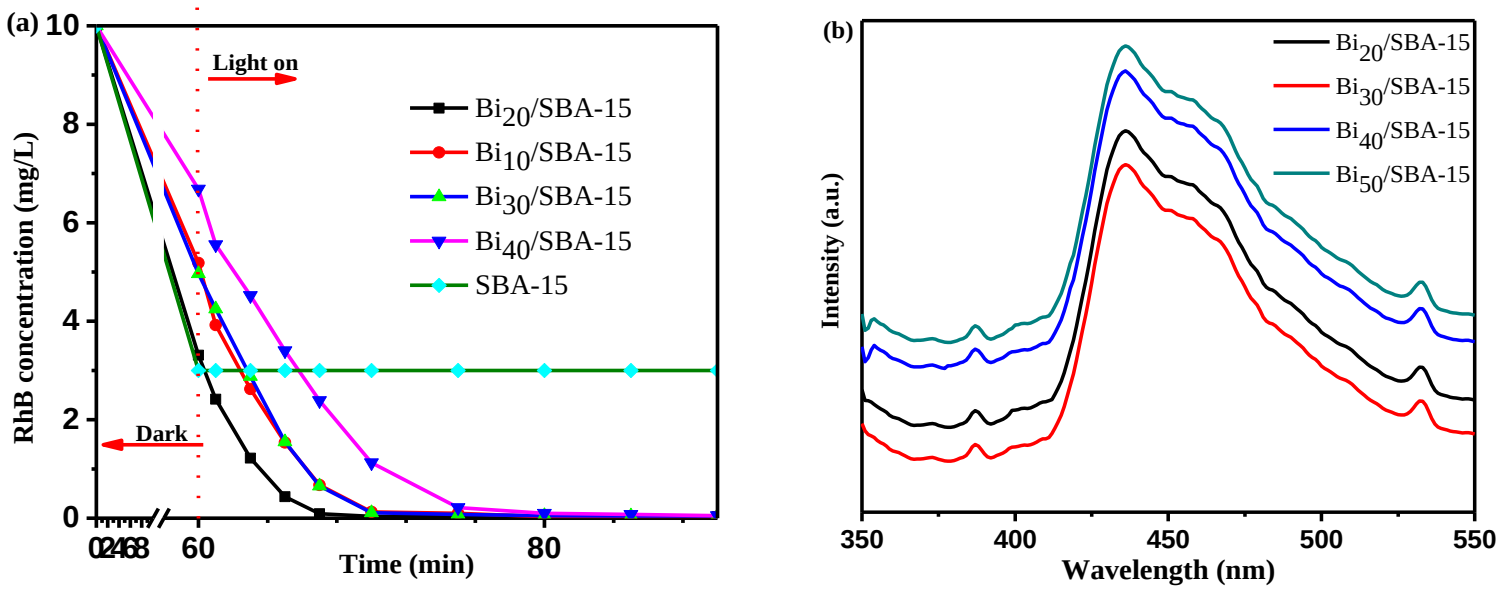

Fig. 3-6 Photocatalytic performance (a) and photoluminescence spectra (b) of the samples

3.3.5 Evaluation on ammonium removal by using $Bi_4O_5Br_2$/SBA-15 photocatalyst

In the past time, the adsorption method was usually adopted for ammonium removal. As we know, water pollution is not usually caused by single substance, while the most cases are by the co-existence of inorganic and organic components. Ammonium is almost existed in differents wastewaters. Based on the adsorption capacity of SBA-15, the ammonium removal was carried out by this new photocatalyst under visible light. In order to further evaluate the ammonium removal by using the synthesized $Bi_4O_5Br_2$/SBA-15 photocatalyst, a high concentration of ammonium solution, 500 mg/Lwas used for this test under the visible light. From Fig. 3-9, the whole process of ammonium removal was a rapid adsorption reaction within 20 min, and the adsorption equilibrium reached about 60 min. The removal rate of ammonium was increased with the increase of $Bi_4O_5Br_2$ iloading during the whole process. Bi_{50}/SBA-15 obtained the best removal rate with 81.3% ammonium removal in **(**Fig. 3-9(a)). The result showed the $Bi_4O_5Br_2$ loading could enhance the removal rate of ammonium due to the increase of specific surface area. The curves of $-\ln(C/C_0) \sim t$ (Fig. 3-9(b)) denoted a linear trend, which indicated that the removal ammonium followed the quasi-first-order kinetic equation.

3.4 Summary

The new mesoporous composite $Bi_4O_5Br_2$/SBA-15 was fabricated by loading the single phase photocatalyst on the mesoporous material SBA-15. The new photocatalyst was confirmed to be a mesoporous material with Langmuir type IV hysteresis loops, well-ordered mesoporous hexagonal arrays and one-dimensional channels. The new photocatalyst has the characteristics of $Bi_4O_5Br_2$ and SBA-15, and strong visible light responsiveness. The RhB decoloration rate had a positive relationship with the $Bi_4O_5Br_2$ loadings on SBA-15. The change trend of RhB decoloration was firstly increased and then decreased under visible light. The highest RhB decoloration rate was obtained at a mass ratio of Bi/SiO_2 of 30:100. $Bi_4O_5Br_2$/SBA-15 is also a good cocatalyst for ammonium removal and Cr(VI) photoreduction from syhthetic wastewater. This work shed new light on the design of new designing the photocatalysts with high efficiency and stability for environmental remediation.

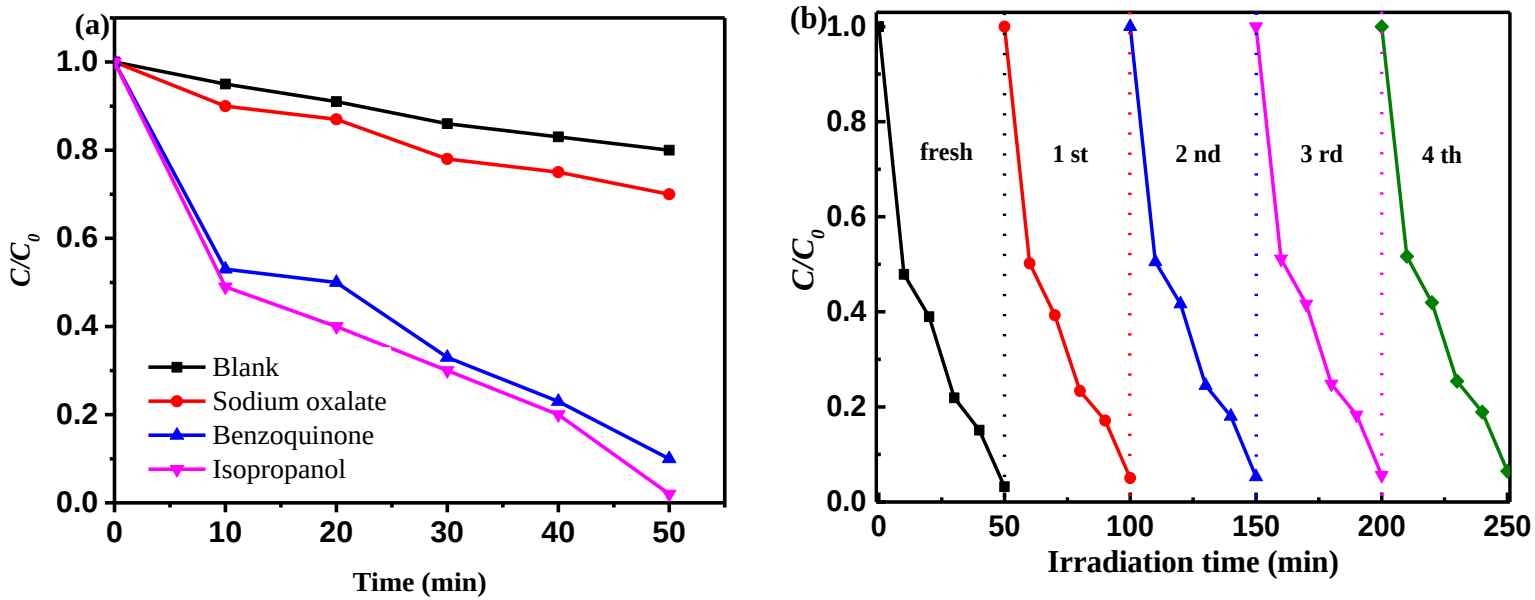

Fig. 3-7 Effects of various scavengers on RhB removal with synthesized photolyst $Bi_4O_5Br_2$

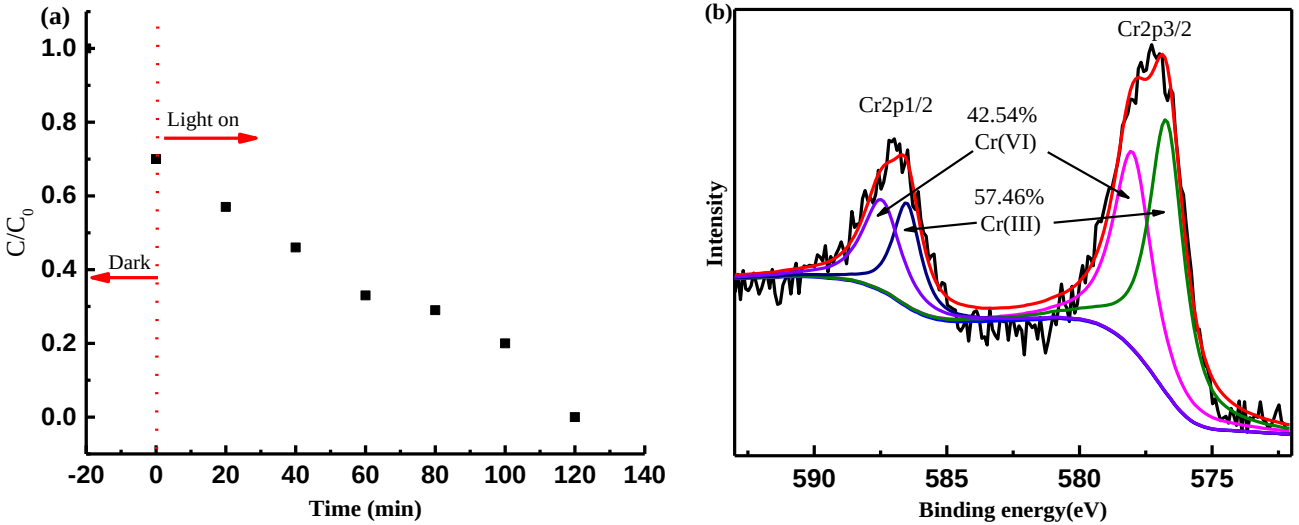

Fig. 3-8 Cr(VI) removal (a) and Cr distribution (b) over Bi_{30}/SBA-15 at pH=11 by XPS

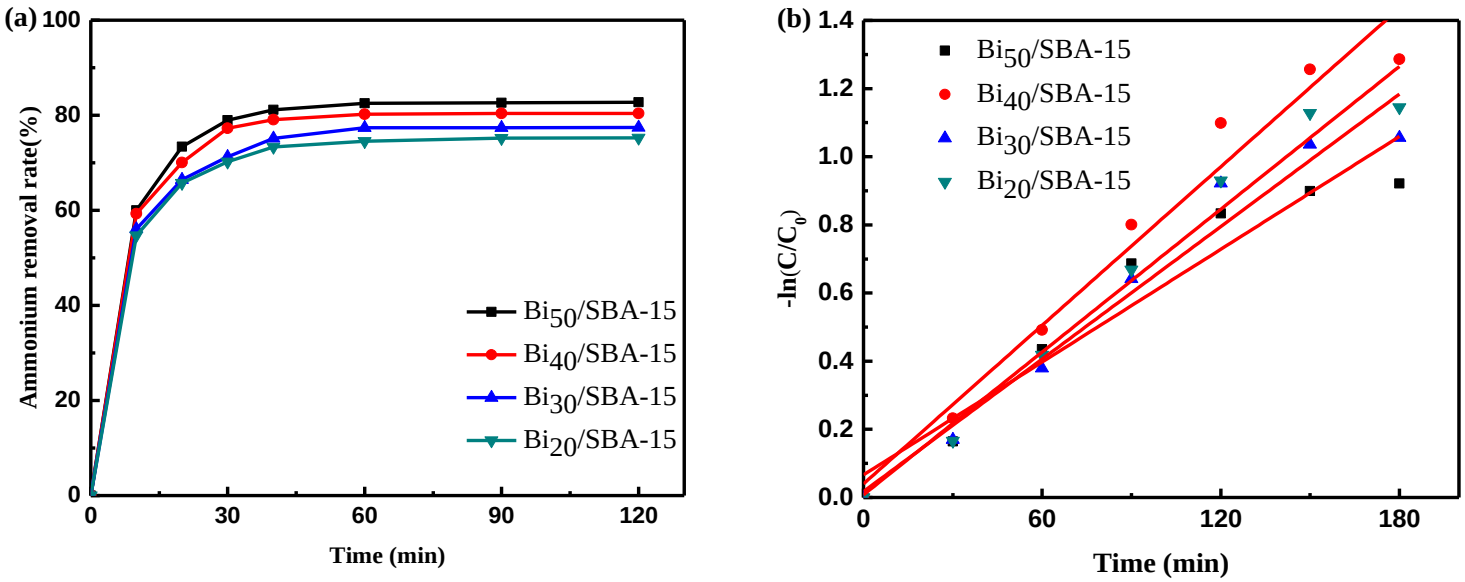

Fig. 3-9 Ammonium removal rate (a) and fit curve of $-\ln(C/C_0) \sim t$ (b) of the obtained samples

Chapter 4 Synthesis of $Bi_4O_5Br_2/ZrO_2$-WO_3/SBA-15 semiconductor and its co-catalytic performance

4.1 Introduction

As shown in Chapter 3, $Bi_4O_5Br_2$/SBA-15 has better photocatalytic performance for RhB decoloration, ammonium removal and chromium detoxification under visible light. However, the band gap of $Bi_4O_5Br_2$/SBA-15 is still wide (from 3.10 to 3.30 eV), which influences the separation rate of photogenerated electron and holes.

WO_3 is a typical n-type metal oxide semiconductor with a band gap of 2.4~2.8 eV, high photosensitivity, low photoluminescence and special atom conduction [143, 144]. In addition, it has some advantages such as non-toxicity, chemical stability, redox of charge carriers, capacibility of various scaffolds, and better electronic band structure, which can promote its application in wastewater treatment [145, 146]. ZrO_2 is a common transition metal oxide with good acid resistance, thermal stability, and surface defects [147-149]. It is important that ZrO_2 can interact with active components and some loading materials to form excellent catalyst. Recently, ZrO_2-WO_3/SBA-15 has been successfully synthesized, which could enhance the photocatalytic performance. Untill now, however, there is no reporte on coupling with ternary metal to form catalyst by using ZrO_2-WO_3 and $Bi_4O_5Br_2$/SBA-15 [150]. In this chapter, the new photocatalyst $Bi_4O_5Br_2/ZrO_2$-WO_3/SBA-15 was prepared by one-step solvothermal method. The morphology, specific surface area, loading ratio and optical properties of $Bi_4O_5Br_2/ZrO_2$-WO_3/SBA-15 were characterized by XRD, BET, TEM, XPS, DRS and other methods. Using Rhodamine B (RhB), chromium and ammonium as target contaminants, the different decolorization capacities and detoxification of the synthesized photocatalysts (obtained under different loading mass ratios of ZrO_2-$WO_3/Bi_4O_5Br_2$/SBA-15) were investigated. At the same time, the photocatalysis stability and reusability of the newly synthesized $Bi_4O_5Br_2/ZrO_2$-WO_3/SBA-15 were also evaluated.

4.2 Materials and methods

4.2.1 Synthesis of mesoporous $Bi_4O_5Br_2/ZrO_2$-WO_3/SBA-15 composite

$Bi_4O_5Br_2/ZrO_2$-WO_3/SBA-15 was prepared through the following two steps. The first step was to synthesize ZrO_2-WO_3/SBA-15 with solvothermal method. 2.0 g P_{123} was dissolved in 65 ml of deionized water at room temperature for 3 h, and 10 ml of 2 mol/L hydrochloric acid

solution was added and stirred vigorously at 40 ℃ for 1 h. 0.72 g sodium tungstate dihydrate was added into the above solution under stirring for 1 h. After that, 4.5 g tetraethyl orthosilicate (TEOS) and 0.2139 g zirconium oxychloride octahydrate were slowly added in the mixture with rapid speed stirring at 40 ℃ for 24 h. The solution was treated at 100 ℃ for 24 h, centrifuged, washed and dried at 60 ℃ for 8 h. The obtained solid samples were calcined at 550 ℃ in air atmosphere for 6 h, which were labelled as ZrO_2-WO_3/SBA-15.

In the second step, $Bi_4O_5Br_2$/ZrO_2-WO_3/SBA-15 was prepared by sol-gel method. 30 ml glycerin and 30 ml deionized water were dropped into a 500ml beaker under stirring for 20 min. After that, $Bi(NO_3)_3$•$5H_2O$ and NaBr was added into the above solution under stirring for 1 h and then PEG-10000 was added into the mixture with pH adjusted to 11 under rapid stirring for 30 min. 0.1 g of ZrO_2-WO_3/SBA-15 was added into the reaction system. After 3 h, the solution was treated at 140 ℃ for 18 h. Then the solids were centrifuged and washed three times with deionized water and ethanol, and dried at 60 ℃ for 8 h. Different mass ratios of Bi/SiO_2 were designed at 10:100, 20:100, 30:200 and 40:100, respectively to test its effect on the synthesized composite, which were labelled as Bi_1/ZrW/SBA-15, Bi_2/ZrW/SBA-15, Bi_3/ZrW/SBA-15 and Bi_4/ZrW/SBA-15, respectively.

4.2.2 Characterization and evaluation of the photocatalysts

All the experiments and analytical methods were similar to section 2.2.3. In this study, the ammonium removal with the new synthesized tenary metal coposites $Bi_4O_5Br_2$/ZrW/SBA-15 was also inverstigated in wastewater treatment, and the batch experiments were similar to section 3.2.6. Namely, besides RhB decoloration, chromium and ammonium as the target pollutants were investigated by using the new synthesized photocatalysts**.**

4.3 Results and discussion

4.3.1 Characterization of $Bi_4O_5Br_2$/ZrO_2-WO_3/SBA-15 composite

The small angle XRD of ZrO_2-WO_3/SBA-15 with different $Bi_4O_5Br_2$ loadings was shown in Fig. 4-1. A large diffraction peak (2θ=0.9°~1.0°) and two small diffraction peaks (2θ=1.3~1.8°) were obtained in the small angle of 0.3°~5°, respectively. The crystal diffraction peaks of (100), (110), and (200) were obaerved in the two-dimensional hexagonal structure of ZrO_2-WO_3/SBA-15, indicating that the mesoporous structure of the synthesized photocatalyst didn't change with the increase of of $Bi_4O_5Br_2$ loading. However, the intensity of the diffraction peaks was gradually decreased until disappearance (Fig. 4-1(a)). The main reason was that the

mesoporous structure was destroyed and blocked with the increase of $Bi_4O_5Br_2$ loading. Compared with the small-angle XRD patterns of WO_3/SBA-15 and ZrO_2-WO_3/SBA-15 in Fig. 4-1(b), it is clear to observe the pore change and the atom interaction of the new synthesized material. This phenomenon signals the formation of p-n heterrojunction.

Fig. 4-2 shows the wide-angle XRD diffraction pattern of $Bi_4O_5Br_2$/ZrO_2-WO_3/SBA-15 with different $Bi_4O_5Br_2$ loadings. From (Fig. 4-2(a)), it could be found that all the samples had characteristic peak spectra at 11.2 º, 25.0 º, 32.0 º, respectively. Based on the special crystal position of the tetragonal phase of $Bi_4O_5Br_2$ (standard card JCPDS No. 09-0699) [130], it was found that the characteristic peak disappeared at the corresponding position of 29.0 º, which confirmed that the interraction between $Bi_4O_5Br_2$ and ZrO_2-WO_3/SBA-15 by chemical bonds and then the formation of Schottky barrier [151]. This result first ascertained that the p-n heterojunction structure of the new synthesized photocatalyst was formed by staggered band gap between $Bi_4O_5Br_2$ and ZrO_2-WO_3/SBA-15. The strongest intensity of the diffraction peak was observed at the corresponding position of 32.0 °, indicating that the (012) crystal plane was the main and tetragonal phase $Bi_4O_5Br_2$. In (Fig. 4-2(a)), the characteristic peak of WO_3 was not observed, which indicated that WO_3 could interact with ZrO_2 and $Bi_4O_5Br_2$ to form special heterojunction. Compared with the wide-angle XRD patterns of $Bi_4O_5Br_2$/SBA-15 in Fig. 4-2(b), the peaks of $Bi_4O_5Br_2$/ZrO_2-WO_3/SBA-15 were found to shift from $Bi_4O_5Br_2$/SBA-15, further reflecting the interaction between $Bi_4O_5Br_2$ and ZrO_2-WO_3. In addition, the characteristic peak of Si completely disappeared in (Fig. 4-2(a)).

Fig. 4-3 shows the nitrogen adsorption-desorption isotherm curve of $Bi_4O_5Br_2$/ZrO_2-WO_3/SBA-15. All the curves exhibit the Langmuir type IV hysteresis loops, suggesting that the synthesized Bi_1/ZrW/SBA-15, Bi_2/ZrW/SBA-15, Bi_3/ZrW/SBA-15, and Bi_4/ZrW/SBA-15 had the characteristics of mesoporous materials with ordered mesoporous structures.

In order to further confirm the mesopore structure, BJH adsorption pore distribution curves of the samples were performed (Fig. 4-4). The curves of pore size distribution showed that the pore size of the samples was between 3 and 4 nm. Although their pore size was relatively small, they are still within the range of mesopores (2~50 nm).

The morphology of Bi_1/ZrW/SBA-15 was measured by TEM and HRTEM (Fig. 4-5), which revealed that Bi_1/ZrW/SBA-15 had the topographical and structural features of the nanostructures and the lattice fringes of the crystalline phase. It can be seen from Fig. 4-5(a) that the synthesized Bi_1/ZrW/SBA-15 has a long-range ordered structure with a pore size of about 3.5 nm, which coincides with the above BJH pore size distribution. The black spots are

$Bi_4O_5Br_2$/ ZrO_2-WO_3 nanoparticles. Fig. 4-5(b) show that the lattice fringe spacing d = 0.35 nm of $Bi_4O_5Br_2$/ ZrO_2-WO_3 /SBA-15 is consistent with the lattice fringe of the SiO_2 (101) plane, indicating that the sample has a complete mesopore structure. The lattice fringe spacing was 0.24 nm, in agreement with that of $Bi_4O_5Br_2$ nanoparticles, indicating that the typical layered structure of $Bi_4O_5Br_2$ has not been destroyed during the synthesis process.

In order to further study the elemental composition and valence state of $Bi_4O_5Br_2$/ZrO_2-WO_3/SBA-15, X-ray photoelectron spectroscopy analysis of Bi_1/ZrW/SBA-15 was carried out (Fig. 4-6). Fig. 4-6(a) shows the full spectrum of Bi_1/ZrW/SBA-15 with the characteristic peaks of Si, C, O, Bi, Br, W, Zr and other elements. In this spectrum, the appearance of element C was caused by CO_2 from the sample absorption of air during the analysis. A high-resolution energy spectrum of Si 2p, O 1s, Bi 4f and Br 3d was the same as in Fig. 3-4 (Chapter 3). Fig. 4-6(b) shows the high-resolution energy spectrum of W 4f. The two peaks were 36.1 and 38.0 eV, respectively; the former was corresponded to the 4f7/2 characteristic peak of W^{6+}, and the latter was the characteristic peak of 4f5/2 of W^{5+}. Compared with the characteristic peaks of W elements, we found that two peaks were missing, attributable to the special facets interaction among three metal oxides. According to the high-resolution energy spectrum of Zr 3d Fig. 4-6(c), three characteristic peaks of 181.79, 182.35 and 188.47 eV were observed respectively. According to the high-resolution energy spectrum of Zr 3p Fig. 4-6(d), a peak at 333.6 eV was found to be the corresponding spectrum of 3p3/2. From Fig. 4-6(c) and Fig. 4-6(d), Zr valance was determined as tetravalent. In addition, due to the change in the spectrum of Zr, a part of Zr transfermation from 3d to 3p orbital occurred between WO_3 and $Bi_4O_5Br_2$. Results from the XPS spectra indicated that the detected elements were corresponding to the elements in the synthesized samples.

Fig. 4-7 shows the UV-vis DRS of $Bi_4O_5Br_2$/SBA-15 with different loadings rates of the two major materials. Fig. 4-7(a) illustrates the absorption spectra of $Bi_4O_5Br_2$/ZrO_2-WO_3/SBA-15 at different loadings of $Bi_4O_5Br_2$. All the samples had a certain visible absorption under UV light at the same time, with the highest absorption efficiency of samples obtained at a Bi/SiO_2 of 40/100, indicating that the separation rate of photogenerated electron-hole pairs of this new sample would be the highest under the visible light due to its highest light responsiveness.

As shown in Fig. 4-7(a), all the composite samples exhibited significant absorption side bands in the visible range at around 442, 451, 456, and 465 nm, respectively. In addition, with the increase of the loading ratio, the absorption wavelength of visible light by the photocatalytic material was red-shifted, indicating that the light response range expanded. Among them, the

band gap of Bi_1/ZrO_2-WO_3/SBA-15 was determined to be the narrowest, resulting in the highest utilization efficiency of visible light. From Fig. 4-7(b), the band gap energies of samples were calculated from 2.98 eV to 3.43 eV by using Eq. (2-1). The value of band gap energy increased with the increase of $Bi_4O_5Br_2$ loading, suggesting that the low band gap energy values of samples may bring about the agglomeration of $Bi_4O_5Br_2$ nanoparticles during the synthesis process. Bi_1/ZrW/SBA-15 had the lowest band gap energy, signalling that the suitable mass ratio of the three metals was a key factor for the photogenerated carriers separation.

Photoluminescence spectroscopy is an important approach for characterization of the recombination rate of photocatalysts photoelectron-hole pairs. Fig. 4-8 shows the fluorescence spectra of the synthesized materials at different loadings. The experiments were carried out at room temperature with the excitation wavelength at 250 nm. The peak shapes and positions of the four samples were similar, with the largest peak observed at around 432 nm, indicating that the electronic transitions happened and the photogenerated electron-hole pairs were separated at 432 nm. The separation rate of Bi_1/ZrW/SBA-15 was relatively high, which confirmed that Schottky barrier was formed between ZrO_2-WO_3 and $Bi_4O_5Br_2$/SBA-15 semiconductor.

4.3.2 Evaluation of photocatalytic performance

Fig. 4-9(a) shows the photodegradation curves of Bi_1/ZrW/SBA-15, Bi_2/ZrW/SBA-15, Bi_3/ZrW/SBA-15, and Bi_4/ZrW/SBA-15 at 25 ℃, respectively. Clearly, the reaction process of RhB decoloration can be explained as dark adsorption during the first phase and photocatalytic reaction during the second phase. The order of of RhB decoloration efficiency was as Bi_1/ZrW/SBA-15 > Bi_2/ZrW/SBA-15 > Bi_3/ZrW/SBA-15 > Bi_4/ZrW/SBA-15. The best decoloration capacity of RhB was obtained within 10 min with the composite at a mass ratio of Bi/SiO_2 at 10:100 under visible light. Among the synthesized samples, the band gap of Bi_1/ZrW/SBA-15 was the narrowest, indicating that the photocatalytic performance of Bi_1/ZrW/SBA-15 was better than others. In order to evaluate the reusability of Bi_1/ZrW/SBA-15, the cycling photodegradation experiment of the new photocatalyst Bi_1/ZrW/SBA-15 was carried out for 5 times. From Fig. 4-9(b), it can be seen that the decolorization efficiency of Bi_1/ZrW/SBA-15 decreased to 97.98% after 5 cycles' utilization, possibly due to some deactivation because of adsorption of some by-products or dyes on the active sites of the photocatalyst during the treatment process.

4.3.3 Photoelectrochemical analysis

In the photocatalytic decolorization of RhB, the capture agents SO, IPA and p-BQ were individually added to capture the active species h^+, •OH and/or $•O_2^-$ (Fig. 4-10). As shown, the photocatalytic activity of Bi_1/ZrW/SBA-15 slightly decreased when the capture agent IPA was added. In the case of capture agent p-BQ, the photocatalytic activity of the synthesized photocatalyst was significantly reduced after its addition in the photocatalytic process. When adding SO, the photocatalyst showed almost no effect on the decolorization of RhB, implying that the catalytic activity was significantly inhibited. The electron on the CB of WO_3 may contact with O_2, and finally form a strong oxidizing $•O_2^-$. Both $•O_2^-$ and H_2O_2 have strong oxidation properties, so they can decompose RhB into CO_2 and H_2O. The strong oxidant of •OH can be formed by the holes in the $Bi_4O_5Br_2$ VB with H_2O, then RhB is decolorated into CO_2 and H_2O. Therefore, the photogenerated electron-hole pairs on the surface of the composite photocatalyst can continuously migrate, and thus the photoelectron-hole pair separation ratio of the single photocatalyst is greatly improved.

4.3.4 Evaluation on detoxicification of special pollutants

In this study, ammonium and chromium were used as the toxic target pollutants in wastewater. Chapter 2 and Chapter 3 have already studied the detoxification of chromium and ammonium removal, which also confirmed that the new photocatalyst has co-catalytic performance in wastewater treatment. In this chapter, the tenary metal composite was used for targeting the same pollutants removal. From Fig. 4-11, Cr(VI) can be transferred into stable Cr(III) under visible light. The detoxification rate of the tenary metal composite Bi_1/ZrO_2-WO_3/SBA-15 photocatalyst for Cr(VI) increased with the increase of $Bi_4O_5Br_2$ loading during the 30 min dark adsorption process at the initial solution pH of 7. 99% Cr(VI) was detoxificated with Bi_1/ZrO_2-WO_3/SBA-15 under visible light during the whole process (Fig. 4-11(a)), which indicated that the tenary metal composite has good reduction and adsorption capacity on Cr(VI).

In order to further evaluate the practical application values of $Bi_4O_5Br_2/ZrO_2$-WO_3/SBA-15 photocatalyst, the experiment was carried out with high concentration of ammonium nitrogen as another target pollutant under the visible light (Fig. 4-12). As seen, the adsorption capacity decreased with the increase of $Bi_4O_5Br_2$ loading during the dark reaction. Compared with $Bi_4O_5Br_2$//SBA-15 in Chapter 3, the adsorption capacity of the synthesized $Bi_4O_5Br_2/ZrO_2$-WO_3/SBA-15 was much lower, indicating that the porous and specific surface area of $Bi_4O_5Br_2/ZrO_2$-WO_3/SBA-15 became smaller, attributable to the internal intereaction between

$Bi_4O_5Br_2$ and ZrO_2-WO_3. This phenomenon suggests that the photocatalytic performance of the synthesized material was enhanced by the special distribution of Zr. Bi_2/ZrO_2-WO_3/SBA-15 obtained 84.3% removal rate of ammonium in this study (Fig. 4-12(a)), which is the optimal mass ratio of $Bi_4O_5Br_2$ loading. All the curves of $-\ln(C/C_0) \sim t$ (Fig. 4-12(b)) exhibited a linear trend, indicating that the ammonium removal by using this photocatalyst follows the quasi-first-order kinetic model.

4.4 Summary

In this chapter, $Bi_4O_5Br_2/ZrO_2$-WO_3/SBA-15 was successfully synthesized by coupling with tenary metal semiconductor. The new photocatalyst was confirmed to have p-n heterojunction and mesoporous structure. The UV-vis analysis revealed that all the samples had better light absorption and their band gap energies ranged from 2.49 eV to 3.25 eV. The order of photocatalytic ability of synthesied composites with different $Bi_4O_5Br_2$ loadings was determined as: Bi_1/ZrW/SBA-15 > Bi_2/ZrW/SBA-15 > Bi_3/ZrW/SBA-15 > Bi_4/ZrW/SBA-15. The photocatalyst can be recycled and reused for 5 times without significant loss of photoactivity when dealing with RhB decolorization. The new synthesized photocatalyst can be applied for Cr(VI) detoxification and high concentration of ammonium nitrogen removal in wastewater under visible light. The new photocatalyst as a co-catalyst is promising for the removal of co-existing pollutants from wastwater.

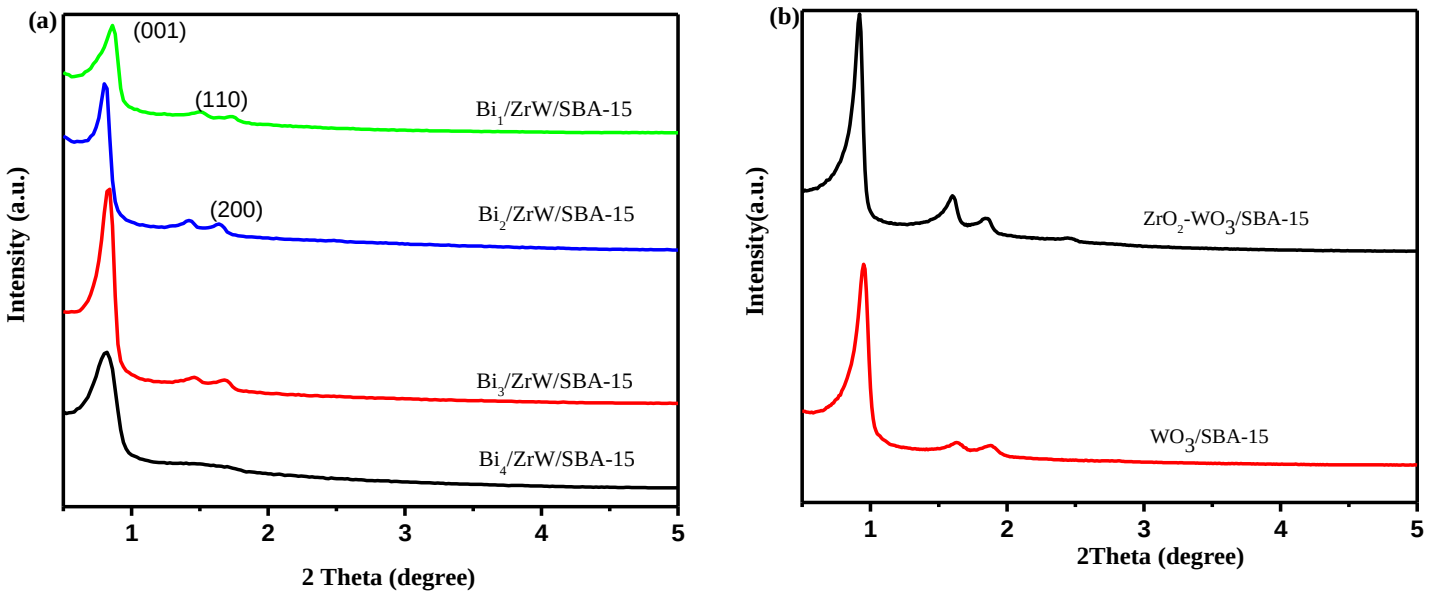

Fig. 4-1 Small angle XRD patterns of $Bi_4O_5Br_2/ZrO_2$-WO_3/SBA-15 (a) and control samples of WO_3/SBA-15 and ZrO_2-WO_3/SBA-15 (b)

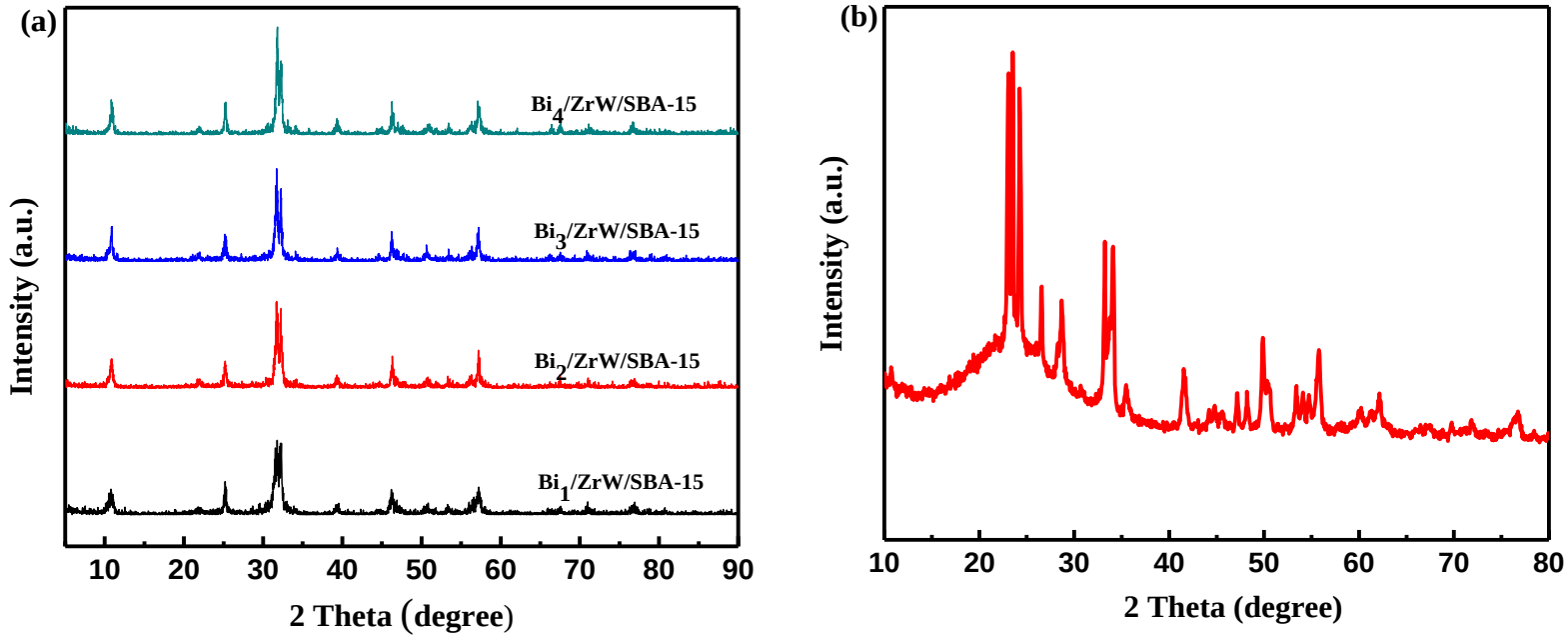

Fig. 4-2 Wide-angle XRD patterns of $Bi_4O_5Br_2/ZrO_2$-WO_3/SBA-15 (a) and ZrO_2-WO_3/SBA-15 (b)

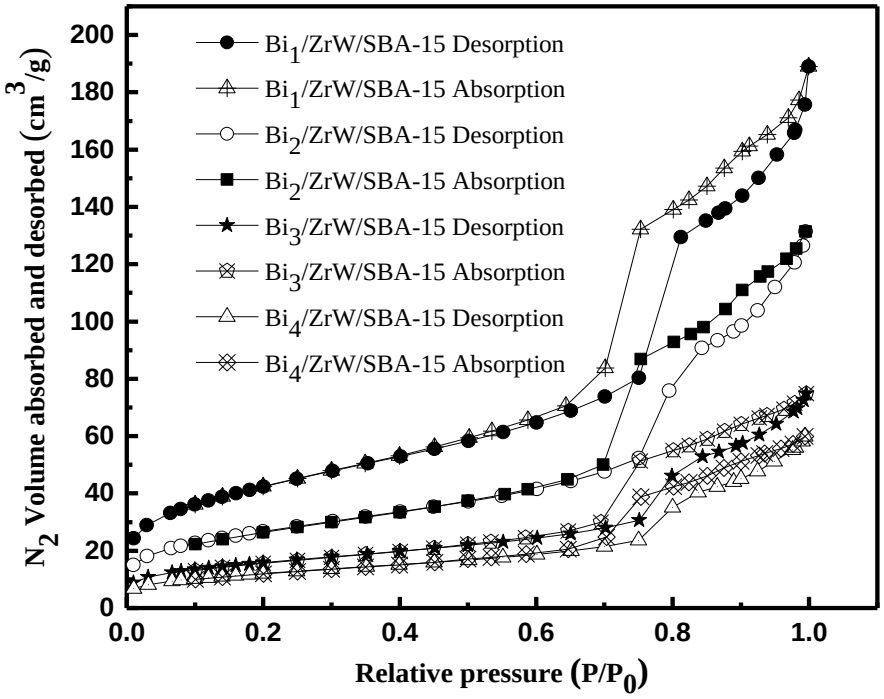

Fig. 4-3 Nitrogen adsorption-desorption isotherms of samples

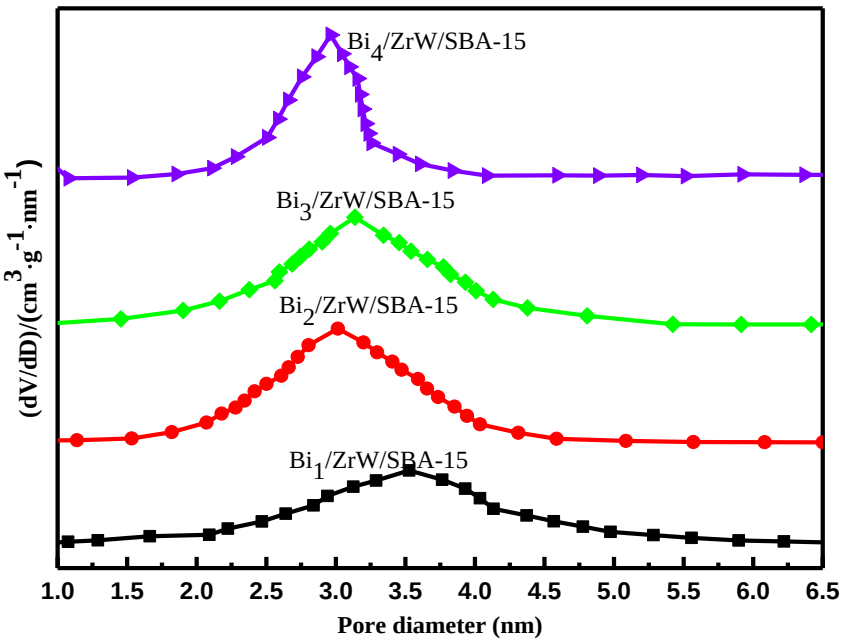

Fig. 4-4 BJH adsorption pore distribution curves of samples

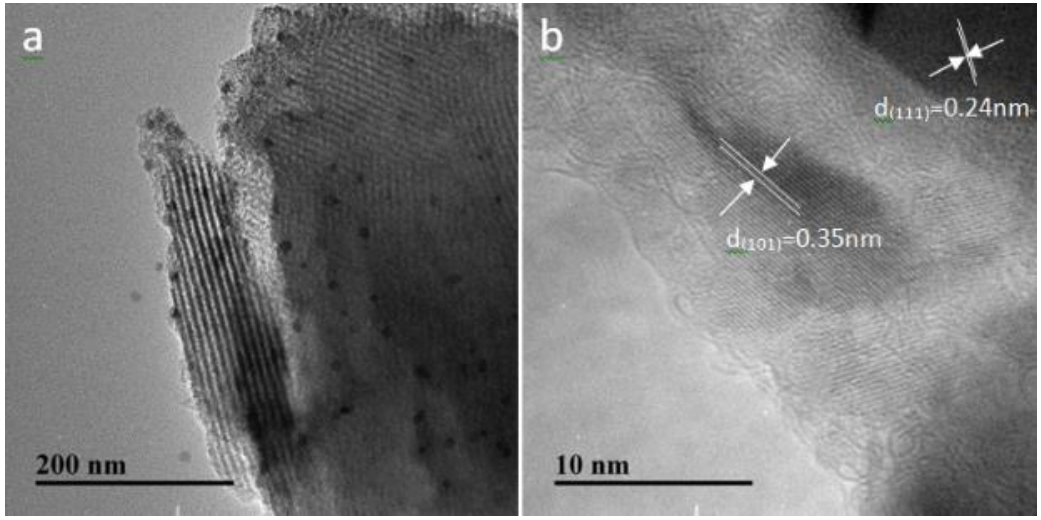

Fig. 4-5 (a) TEM image and (b) HRTEM images of Bi_1/ZrW/SBA-15

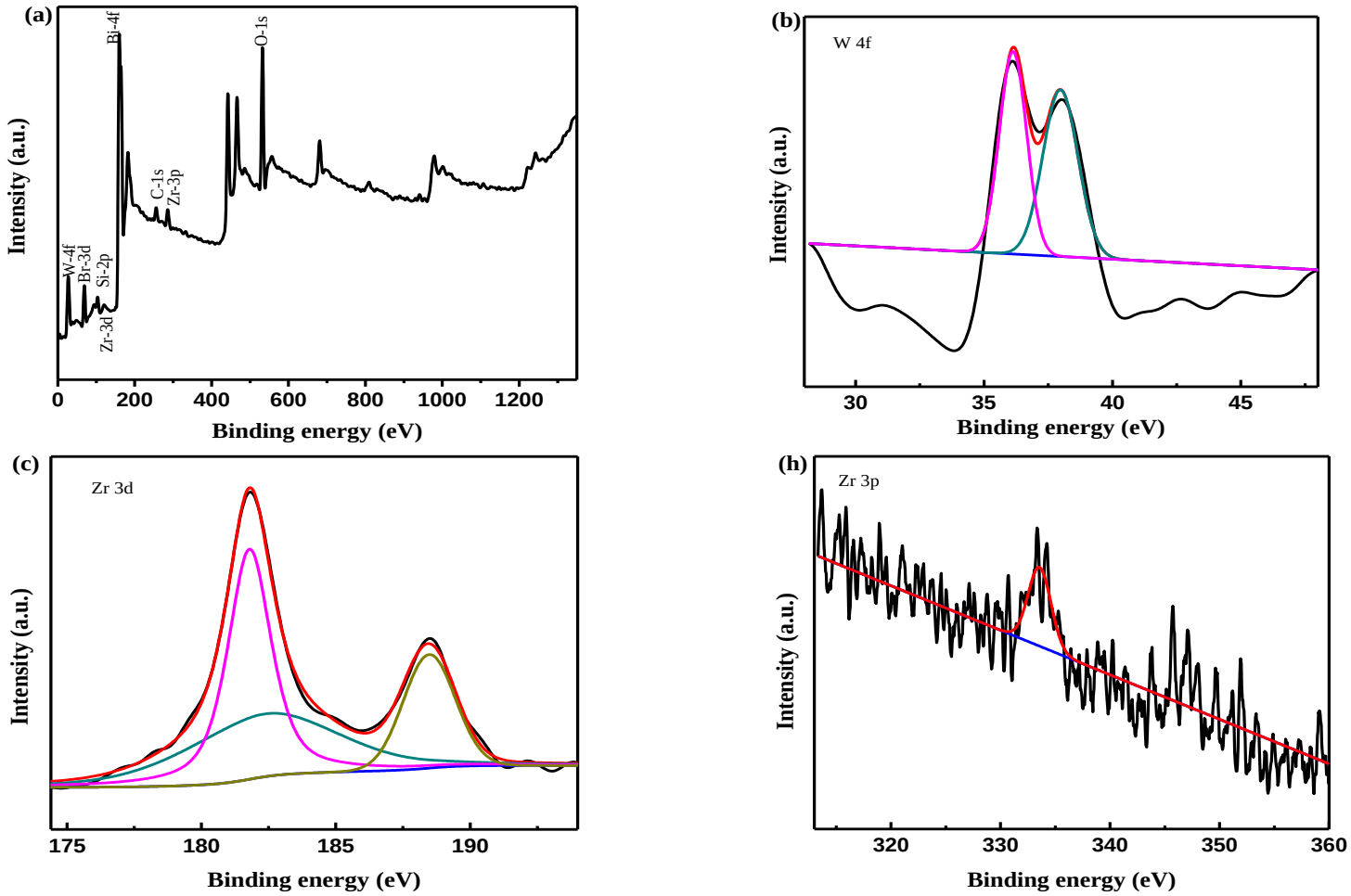

Fig. 4-6 XPS spectra of Bi_1/ZrW/SBA-15: (a)full spectrum, (b)W 4f, (c) Zr 3d and (d) Zr 3p (Note: Si 2p, O 1s, Bi 4f and Br 3d is the same as Fig. 3-4 in Chapter 3)

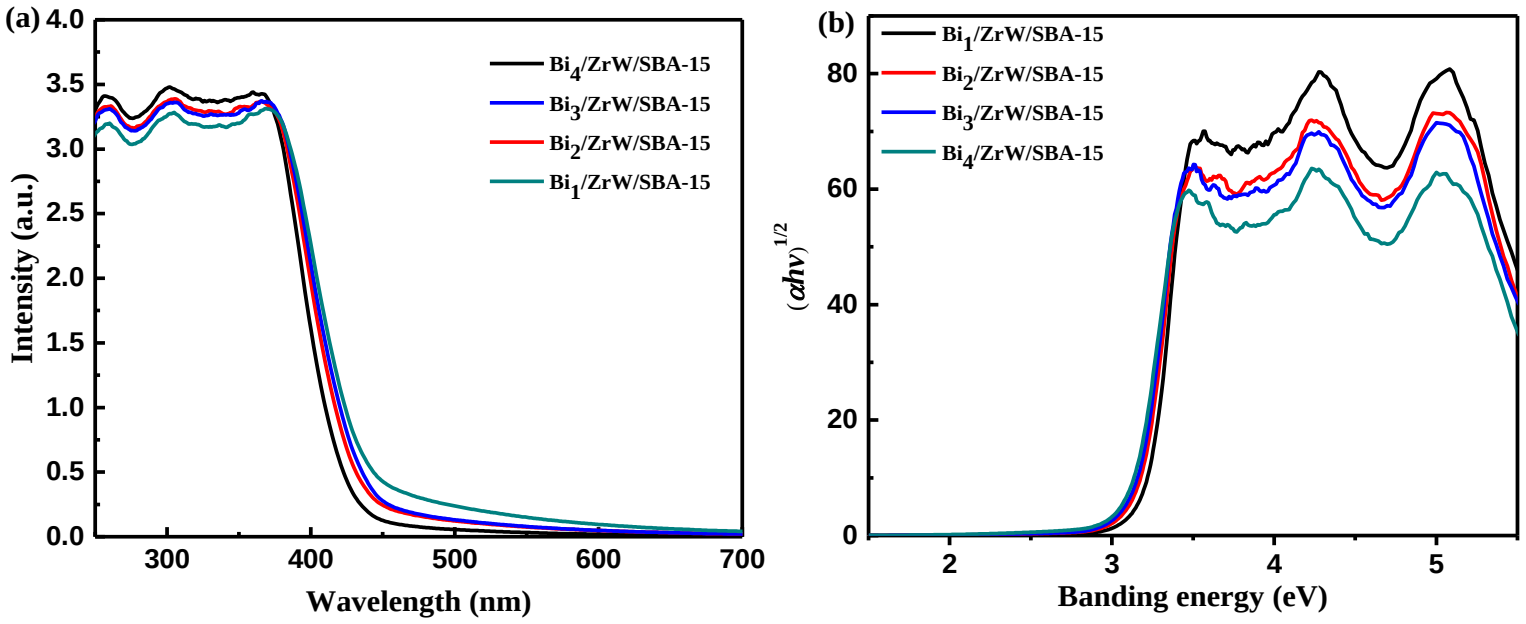

Fig. 4-7 UV–vis diffuse reflectance spectra (a) and $(\alpha h\nu)^{1/2}$ - ($h\nu$) curves (b) of samples

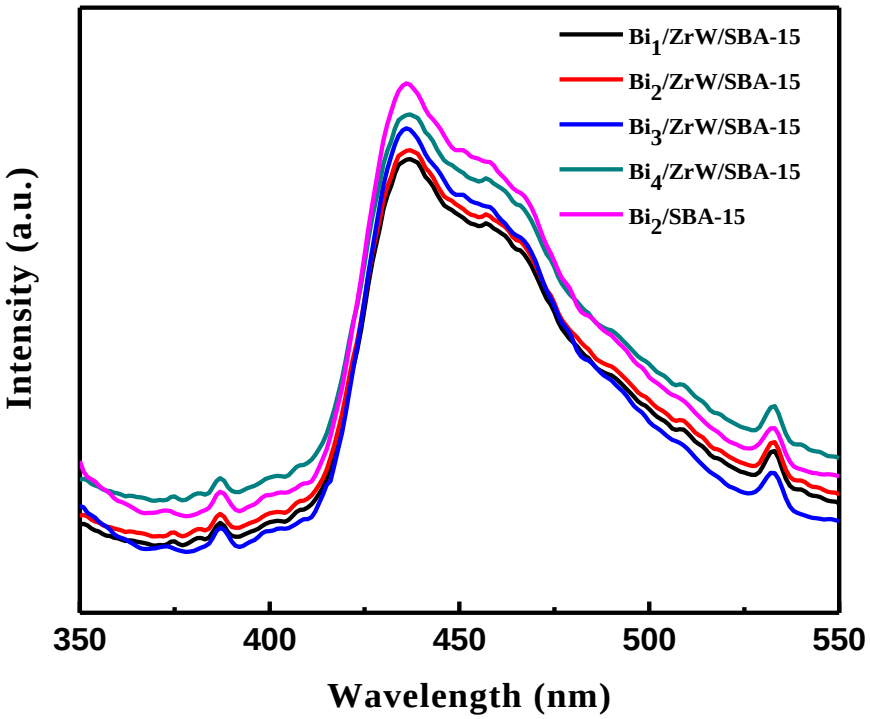

Fig. 4-8 Photoluminescence spectra of different samples

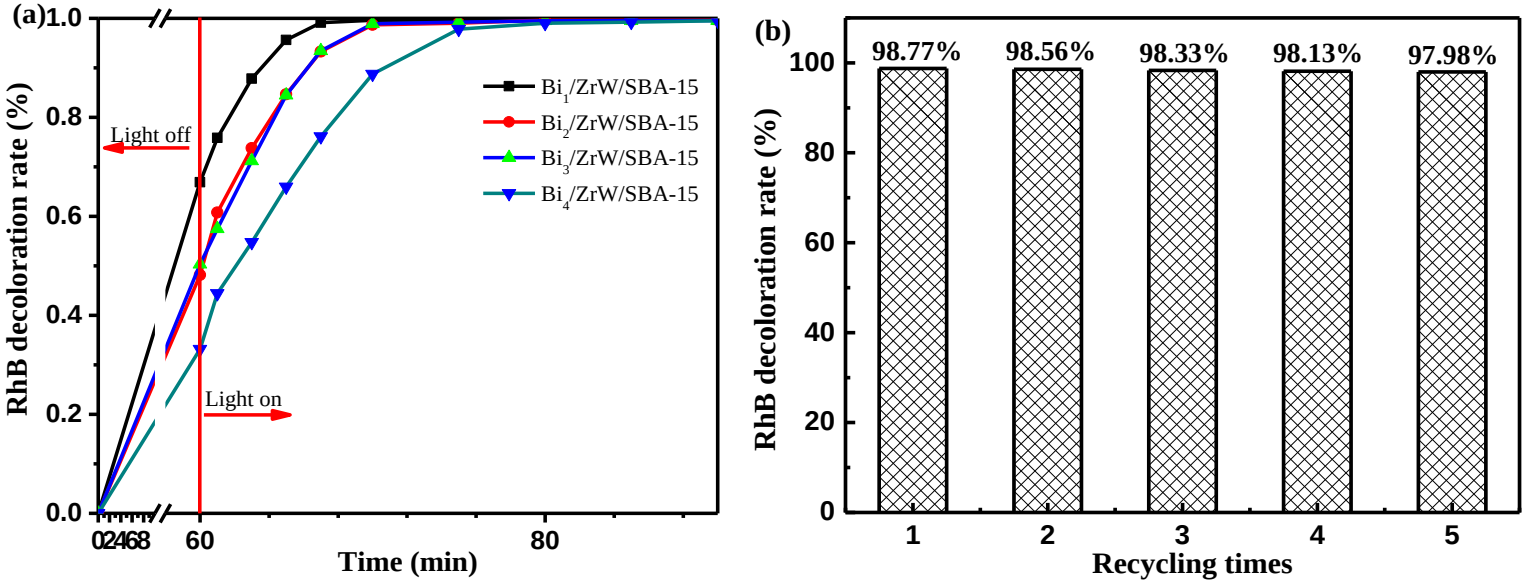

Fig. 4-9 Photocatalytic degradation rate curves of samples (a) and cyclic stability testing of Bi_1/ZrW/SBA-15 (b)

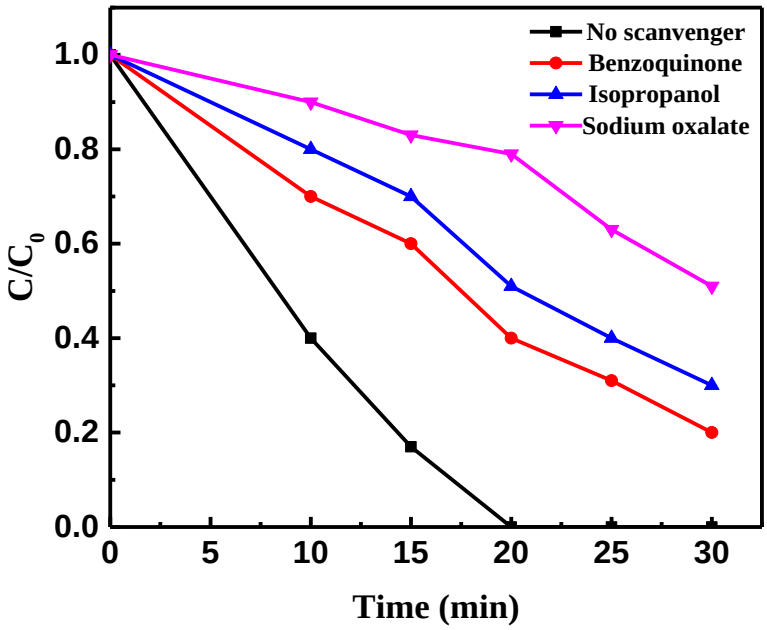

Fig. 4-10 Effects of the synthesized materials on various scavengers

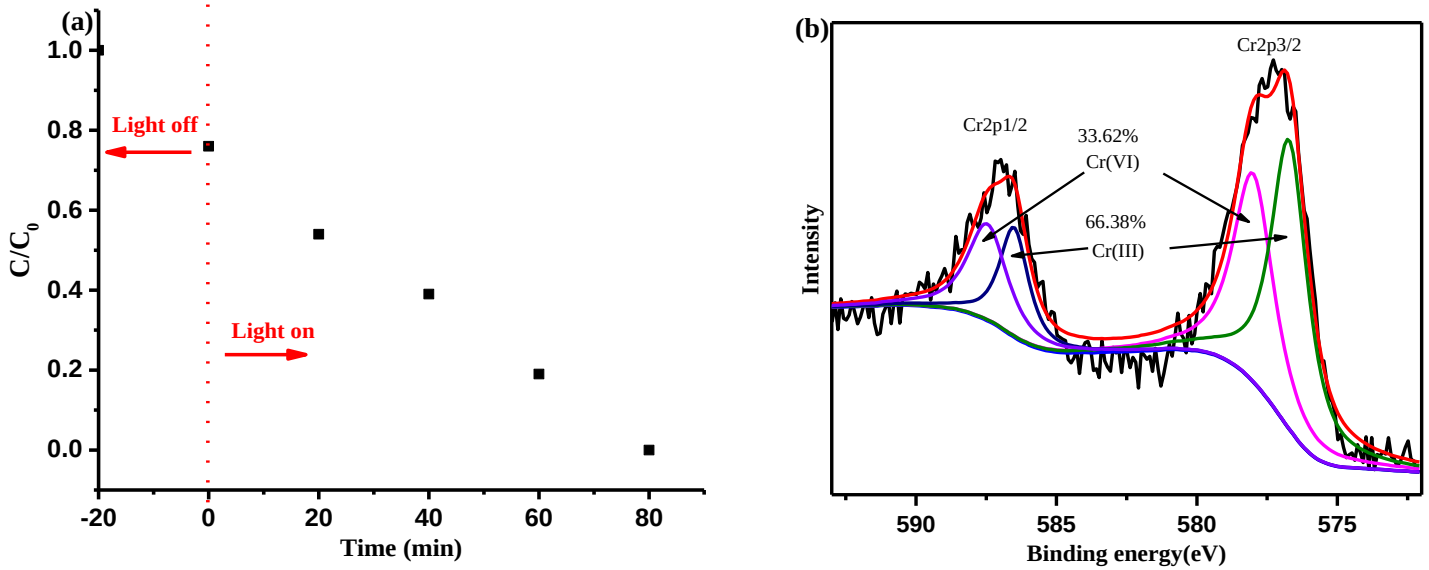

Fig. 4-11 Cr(VI) removal by the synthesized Bi_1/ZrO_2-WO_3/SBA-15 samples (a) and the Cr distribution on Bi_1/ZrO_2-WO_3/SBA-15 by XPS analysis (b)

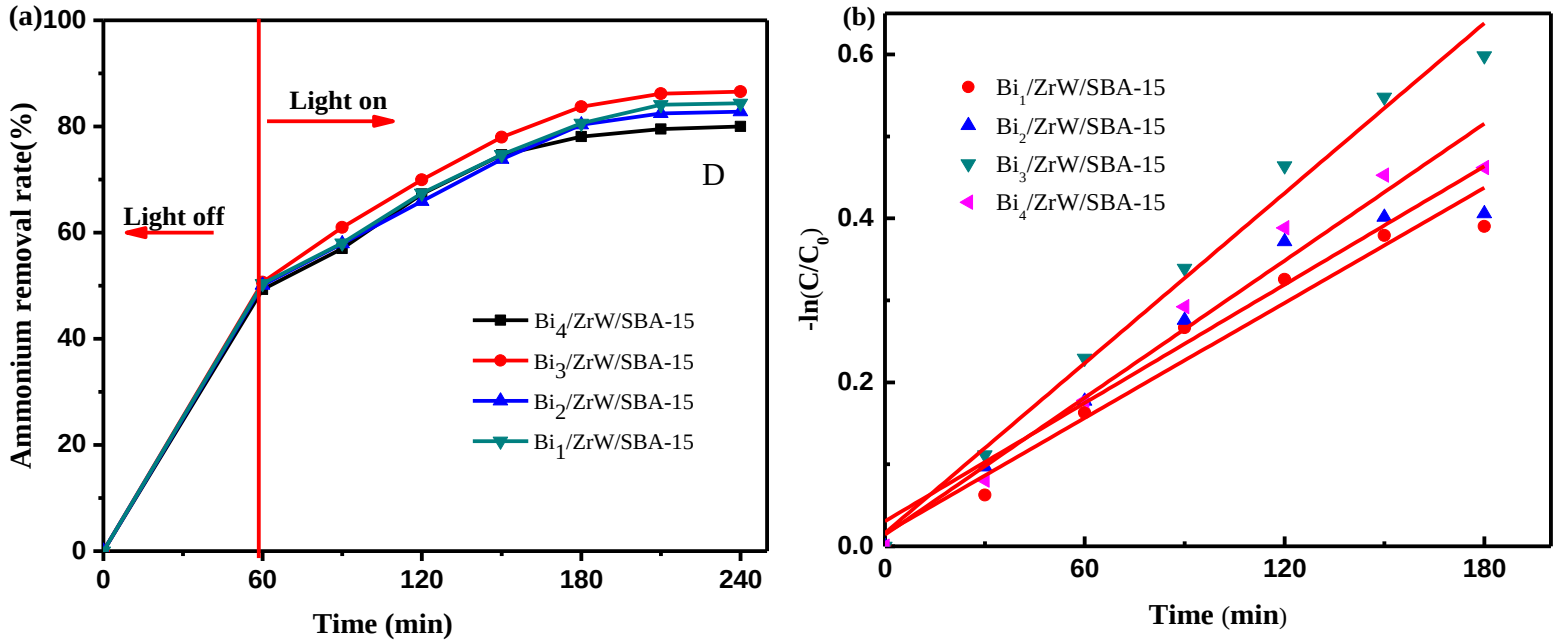

Fig. 4-12 Ammonium removal by using the synthesized $Bi_4O_5Br_2/ZrO_2$-WO_3/SBA-15 samples (a) and the kinetic model under visble light (b)

Chapter 5 Preparation of g-C_3N_4/$Bi_4O_5Br_2$ photocatalyst and its application in synthetic wastewater treatment

5.1 Introduction

Single-phase photocatalysts g-C_3N_4 and $Bi_4O_5Br_2$ have good photoctalytic performance. However, some bottlenecks still exist in thei development of their synthesis technology and application for wastewater treatment. In order to overcome these problems, semiconductor compound has been considered as an effective solution. Generally, compared with the single-phase photocatalysts, the compound semiconductor photocatalyst can realize the synergistic effect on pollutants removal or transformation. In addition, the semiconductor photocatalyst can expand the light absorption edge and improve the separation rate of the electron holes.

The single-phase $Bi_4O_5Br_2$ was firstly synthesized with the direct reagent by breaking the layered structure in Chapter 2, which showes the excellent photocatalytic performance on RhB decoloration and chromium detoxifictation. In practice, it also has some disadvantages such as large particle size, small specific surface area, and high electron-hole recombination rate [152]. Semiconductor recombination is an effective method for improving the photogenerated electron-hole pairs separation by double layer electronic overlay field to form Schottky barrier. Therefore, coupling the single-phase $Bi_4O_5Br_2$ with suitable semiconductor is the key to the enhancemeng of the photocatalytic performance.

g-C_3N_4 has a two-dimensional structure similar with graphene. In addition, g-C_3N_4 has a semiconductor structure with a band gap value of 2.7 eV, water stability (insoluble at pH = 0-14), non-toxicity because of no metal elements and other properties. Compared with other photocatlysts, g-C_3N_4 has been confirmed to have broader application prospects in the field of catalysis [153,154]. The excellent photocatalytic performance of g-C_3N_4 is mainly dependent on its porosity and high degree of condensation. The combination of g-C_3N_4 and $Bi_4O_5Br_2$ semiconductor are expected to improve $Bi_4O_5Br_2$ distribution and accelerate electron hole separation with enhanced photocatalytic activity [155]. However, up to now, there was no report on coupling the single-phase g-C_3N_4 with $Bi_4O_5Br_2$ semiconductors, and the photoelectron migration on the surface of the photocatalyst, the recombination rate of photogenerated electrons and holes have not been studied yet.

In this study, the band overlap structure of $Bi_4O_5Br_2$ and g-C_3N_4 (graphite phase carbonitride) was prepared, and the mechanisms of accelerating the carrier migration rate and reducing the

recombination rate of photogenerated electron hole pairs were investigated by using this new synthesized photocatalyst. The nanosheet of g-C_3N_4 was peeled off by in-situ composite method and introduced onto the surface of $Bi_4O_5Br_2$ to prepare different photocatalysts of g-C_3N_4/$Bi_4O_5Br_2$ composite photocatalysts. The structure, morphology, optical properties and specific surface area of the prepared materials were investigated. Rhodamine B (RhB), phenol and chromium were used as target contaminants to evaluate its practical application in wastewater treatment. At the same time, the used g-C_3N_4/$Bi_4O_5Br_2$ was recovered, and tested for its photocatalytic stability and reusabililty.

5.2 Material and methods

5.2.1 Synthesis of g-C_3N_4/$Bi_4O_5Br_2$

Firstly, g-C_3N_4 was synthesized: 3g melamine powder was added into a 30 ml capped alumina crucible, and then calcinated at 550 ℃ in a muffle furnace for 4 hours at a heating rate of 2 ℃/min from the beginning of room temperature. After that, the muffle furnace was naturally cooled to room temperature, and the sample was taken out and ground to obtain a pale yellow powder g-C_3N_4.

The second step was to couple the single phase photocatalyst $Bi_4O_5Br_2$ with g-C_3N_4. The synthesis method was described as follows: 15 ml glycerol and 15 ml deionized water were added into a beaker with magnetic stirring until the solution completely dissolved. After that cetyltrimethylammonium bromide (CTAB, 1.5 mmol) and 1.5 mmol $Bi(NO_3)_3$•$5H_2O$ was dropped into the above solution under stirring until the formation of a milky white mixture. 0.1 g polymer (PEG-10000) was added into the reactor system under stirring for 1 h. The reactor system pH was adjusted to 11 by using 1 mol•L^{-1} NaOH or ammonium solution. In this study, in order to avoid the metal ions' entering into the layered structure and destroy the force intereaction between the layered structures, ammonium solution was mainly selected during the synthesis process for the alkalinity adjustment of the mixture system. After 1h, the solution was placed in a stainless steel reaction vessel with 50 ml of Teflon-lined at 140 ℃ for 24 h. Then the oven was powered off and cooled to room temperature, and centrifuged. The solid powder was washed 5 times with deionized water and absolute ethanol, and dried in an air oven at 60 ℃ for 12 h, and the samples were collected and weighed.

Finally, the coupling process of g-C_3N_4/$Bi_4O_5Br_4$ composite photocatalyst was conducted following the steps below: 15 ml glycerol and 15 ml deionized water were added into a beaker under stirring until it became clarified. Accurately weighed 1.5 mmol of

cetyltrimethylammonium bromide (CTAB) and 1.5 mmol of $Bi(NO_3)_3 \cdot 5H_2O$ and then added into the above solution with magnetic stirring until the formation of a milky white suspension. After that, 0.1 g of polymer (PEG-10000, respectively) was added into the above mixture system and the solution pH was adjusted to 11 by 1 mol•L^{-1} ammonium solution. Different mass ratios of g-C_3N_4 were added to the above mixture under stirring for 1 h, and then transferred to a 50 mL reactor and heated at 140 ℃ for 24 h. The obtained products were washed three times with deionized water and ethanol subsequencially, and dried at 60 ℃ for 6 h. The samples with different ratios of g-C_3N_4 and $Bi_4O_5Br_4$ were recorded as 1:9, 3:7, 5:5, 7:3 and 9:1 (g-C_3N_4/ $Bi_4O_5Br_4$).

5.2.2 Characterization

In this chapter, the new semiconductor composite g-C_3N_4/$Bi_4O_5Br_2$ was characterized from morphology, XRD pattern, optical property, photocurrent, active species measurement and photocatalytic performance. The detail methods have been described in Chapter 2 and Chapter 3.

5.3 Results and discussion

5.3.1 Characterization of g-C_3N_4/$Bi_4O_5Br_2$ composites

Fig. 5-1 shows the FT-IR spectra of $Bi_4O_5Br_2$, g-C_3N_4 and the composited samples from different mass ratio of g-C_3N_4 and $Bi_4O_5Br_2$. Bi-Br vibration absorption peak was observed at 500-1000 cm^{-1}, and the peak intensity was decreased with the decrease of $Bi_4O_5Br_2$ mass ratio. The asymmetric stretching vibration peaks of C-N (-C)-C and C-NH-C were observed at 800-4000 cm^{-1} [155]. The absorption peak sof N-H and C-H were at 3000-3500 cm^{-1}, and the carbon-nitrogen heterocycle absorption peaks were observed at 1236, 1320, 1404, 1567 and 1626 cm^{-1} [155], respectively. The absorption peak at 800 cm^{-1}, could be ascribed to the triazine ring vibration. In summary, the main characteristic peaks of $Bi_4O_5Br_2$ and g-C_3N_4 were existed in the composites, indicating that the semiconductors were successfully compounded.

Fig. 5-2 shows the XRD patterns of g-C_3N_4, $Bi_4O_5Br_2$ and g-C_3N_4/$Bi_4O_5Br_2$. As seen, a strong peak of g-C_3N_4 was at 27.5 ° in the XRD pattern, which corresponds to the (002) interlayer reflection of a graphitic-like structure [156-158]. Another special characteristic peak was observed at around 13.2 °, which suggested the (100) crystal plane of melon-like substance in g-C_3N_4 [159, 160]. It also reflected that the characteristic peaks of $Bi_4O_5Br_2$ (JCPDS standard

card No. 37-0699) [63], attributable to the (101) and (110) facets of tetragonal $Bi_4O_5Br_2$ at around 29 °and 32 °, respectively. The diffraction peaks of $Bi_4O_5Br_2$ can also be seen at 15.72 °, 17.70 °, 22.42 °, 23.72 °, 25.08 °, 35.70 °, 39.04 °, 40.08 °, 45.54 °, 46.66 °and 52.68 °, respectively, indicating that the $Bi_4O_5Br_2$ photocatalyst sample has good crystallinity under the designed conditions in the synthesis process. Compared with g-C_3N_4, the diffraction peak of g-C_3N_4 was relatively weaker in the g-C_3N_4/$Bi_4O_5Br_2$ samples, suggesting that the crystallinity of g-C_3N_4 was covered by the diffraction peaks of $Bi_4O_5Br_2$. In addition, the best crystallinity phase was obtained at the mass ratio of $Bi_4O_5Br_2$ to g-C_3N_4 of 5:5.

Fig. 5-3 shows the SEM images of $Bi_4O_5Br_2$, g-C_3N_4, and g-C_3N_4/ $Bi_4O_5Br_2$ (5:5) samples. It was observed that g-C_3N_4 photocatalyst had a block lamination nanosheets structure (Fig. 5-3(a)), while $Bi_4O_5Br_2$ was dimensional flower-like (Fig. 5-3(b)). Figs. 5-3 (c) and (d) demonstrate the SEM and TEM images of g-C_3N_4/$Bi_4O_5Br_2$ (5:5) composite photocatalyst. It can be seen that the flower-like structure of $Bi_4O_5Br_2$ was coated with plurality superposed sheet structure of g-C_3N_4. Moreover, g-C_3N_4 was seen to attach onto the surface of $Bi_4O_5Br_2$. It was speculated that this morphology can greatly increase the specific surface area of g-C_3N_4/ $Bi_4O_5Br_2$ composite photocatalyst, resulting in enhanced adsorption performance of g-C_3N_4/ $Bi_4O_5Br_2$. The synergistic effect of adsorption may also improve the decoloration rate of organic dyes and detoxicification of heavy metals.

The optical properties of the $Bi_4O_5Br_2$, g-C_3N_4 and g-C_3N_4/$Bi_4O_5Br_2$ (5:5) samples were tested by using UV-visible diffuse reflectance spectroscopy. Fig. 5-4(a) shows the diffuse reflectance spectra of $Bi_4O_5Br_2$, g-C_3N_4 and g-C_3N_4/$Bi_4O_5Br_2$ (5:5) samples of the absorption band edge at 510 nm, 467 nm and 532 nm, respectively. The g-C_3N_4/$Bi_4O_5Br_2$ (5:5) composite obtained the largest absorption band edge under visible light. From Fig. 5-4(b), the band gap of $Bi_4O_5Br_2$, g-C_3N_4 and g-C_3N_4/$Bi_4O_5Br_2$ (5:5) samples approximately changed from 2.51 eV to 2.65 eV. g-C_3N_4/$Bi_4O_5Br_2$ (5:5) composite had the lowest band gap, indicating that the g-C_3N_4/$Bi_4O_5Br_2$ (5:5) composite had strong absorption of visible light with excellent photocatalytic properties.

Fig. 5-5 illustrates the nitrogen sorption-desorption isotherm curves of the $Bi_4O_5Br_2$, g-C_3N_4 and g-C_3N_4/$Bi_4O_5Br_2$ (5:5). The curves of g-C_3N_4 and g-C_3N_4/$Bi_4O_5Br_2$ (5:5) sample exhibited the Langmuir type IV hysteresis loops, which suggested that the synthesized g-C_3N_4 and g-C_3N_4/$Bi_4O_5Br_2$ (5:5) samples had the characteristics of mesoporous materials with ordered mesoporous structures [136]. From Table 5-1, it can be found that the specific surface area of g-C_3N_4/$Bi_4O_5Br_2$ (5:5) composite photocatalyst was 26.90 m^2/g, much higher than those of

single-phase $Bi_4O_5Br_2$ and g-C_3N_4, indicating that the composite photocatalyst could have significantly improved photocatalytic performance.

In the photoluminescence spectrum (PL), the lower the PL intensity, the lower he recombination rate of photo-generated e^- and h^+, and the stronger photocatalytic activity. In order to explore the photocatalytic activity of g-C_3N_4 before and after $Bi_4O_5Br_2$ recombination, the PL spectra of $Bi_4O_5Br_2$, g-C_3N_4 and g-C_3N_4/$Bi_4O_5Br_2$ (5:5) were measured at 388 nm (Fig. 5-6). From Fig. 5-6, it can be seen that g-C_3N_4 had a strong emission peak at 453 nm, while g-C_3N_4/$Bi_4O_5Br_2$ obtained the lowest emission peak, suggesting that the recombination of photogenerated e^- and h^+ could be effectively inhibited by $Bi_4O_5Br_2$, and the photocatalytic activity of g-C_3N_4/$Bi_4O_5Br_2$ was improved.

In order to further explore the separation efficiency of e^- and $h^+$by g-C_3N_4/$Bi_4O_5Br_2$, the photocurrent indesity of the synthesized photocatalysyt was investigated in this study. Once the density of photocurrent is higher than the excited CB band energy, a higher the separation rate of e^- and h^+ would occur under visible light. Meanwhile, this result means that the band gap of the composite photocatalyst is narrower. Fig. 5-7 shows that the current density of g-C_3N_4/$Bi_4O_5Br_2$ was the strongest, four times that of g-C_3N_4. This phenomenon can be ascribed to the formation of heterojunction between $Bi_4O_5Br_2$ and g-C_3N_4. On the other hand, the metal atoms of $Bi_4O_5Br_2$ are exposed to the surface of photocatalyst, which can have SPR effect during the light irradiation. The composite photocatalyst g-C_3N_4/$Bi_4O_5Br_2$would obtain a lower recombination rate of e^- and h^+ than $Bi_4O_5Br_2$ and pure g-C_3N_4, which coincides with the analysis of the PL spectrum.

Fig. 5-8 shows the time-resolved fluorescence spectra of g-C_3N_4 and g-C_3N_4/$Bi_4O_5Br_2$ composites at 453 nm by time-dependent single photon counter (TCSPC), with the corresponding parameters of g-C_3N_4 and g-C_3N_4/$Bi_4O_5Br_2$ composites being generated by the light excitation at 388 nm as the excitation wavelength by the carriers. According to the triple exponential decay model, τ_1 and τ_2 are the fluorescence lifetimes of g-C_3N_4 and g-C_3N_4/$Bi_4O_5Br_2$, and τ is the average fluorescence lifetime, α_1 and α_2 are the factors of the corresponding fluorescence lifetime. It can be seen from Fig. 5-8 that τ of g-C_3N_4 and g-C_3N_4/$Bi_4O_5Br_2$ was 2.98 ns and 1.25 ns, respectively, indicating that g-C_3N_4/$Bi_4O_5Br_2$ could prolong the lifetime of photo-generated e^- and h^+ carriers and enhance separation rate of the photo-generated e^- and h^+. In addition, this result also confirmed the formation of heterojunction between $Bi_4O_5Br_2$ and g-C_3N_4.

Fig. 5-9 shows the chemical structure and valence state of the new synthesized photocatalyst.

Fig. 5-9(a) is the full spectrum of g-C_3N_4/$Bi_4O_5Br_2$ (5:5) with the characteristic peaks of Bi4f, O1s, Br3d, C 1s and N 1s. Fig. 5-9(b) is the high-resolution energy spectrum of Bi 4f. As seen from Fig. 5-9b, there are two strong main peaks, 159.4 and 164.8 eV, respectively, and the corresponding spectra are 4f7/2 and 4f5/2. Bi can be characterized as Bi^{3+}. A high resolution energy spectrum of O 1s with two main peaks (Fig. 5-9(c)) was obtained at 530.6 and 533.0 eV, respectively. The main peak 530.6 eV is the Bi-O bond in $[Bi_2O_2]^{2+}$ in the layered $Bi_4O_5Br_2$/SBA-15, while the peak at 533.0 eV represents H_2O or OH^- adsorbed on the surface of the material. Fig. 5-9(d) shows that the high-resolution energy spectrum belongs to Br 3d. As its two partial peak positions are 68.4 and 69.5 eV, respectively, and its corresponding spectra are 3d5/2 and 3d3/2, thus its valence is -1. Fig. 5-9(e) is the high-resolution energy spectrum of C 1S. As seen from Fig. 5-9(e), there are three main characteristic peaks at 289.5 eV, 284.8 eV and 287.0 eV, respectively. The corresponding spectra are the carbon of sp2 hybrid triazine ring (N=CN), the carbon-carbon single bond (CC) or exogenous carbon and the carbon=carbon bond (C=C). Fig. 5-9(f) shows the N 1s high resolution spectrum, in which three main characteristic peaks may occur by Gaussian distribution at 398.9 eV, 400.00 eV, and 401.10 eV. The peak at 398.9 eV may be attributable to the C=N-C binding energy by N sp2 hybridization, and the peak at 400.10 eV is attributed to the binding energy of N sp3 hybridized N $(N\text{-}(C)_3)$. The peak at 401.10 eV is a structural defect of C-N-H, resulting from incomplete condensation from the high-resolution spectrum of carbon and the high-resolution spectrum of nitrogen, which are consistent with g-C_3N_4. Results from the XPS spectra indicate that the measured elements are in agreement with the elements in the synthesized samples.

5.3.2 Photocatalytic performance

Fig. 5-10 illustrated the photodegradation effect of g-C_3N_4 and g-C_3N_4/$Bi_4O_5Br_2$ composite photocatalysts at different mass ratio on RhB decoloration under visible light, in which C is the concentration of RhB solution during the reation process and C_0 is the initial concentration of RhB. It can be seen that the decolorization rate was first decreased and then increased with the increase of mass ratio of g-C_3N_4:$Bi_4O_5Br_2$ (Fig. 5-10(a)). The highest decoloration rate of RhB was achieved at the mass ratio of g-C_3N_4:$Bi_4O_5Br_2$ of 5:5, 100% in 20 min under visible light irradiation. And the new synthesized photocatalyst g-C_3N_4/$Bi_4O_5Br_2$ exhibited the fasted decolorization rate among the tested materials. Fig. 5-10(a) also shows that the photocatalytic effeciency of pure g-C_3N_4 was not so ideal, about 69.3 % during 20 minutes under visible light. Moreover, it is clearly to see that the introduction of $Bi_4O_5Br_2$ had a positive effect on RhB

decolorization under visible light. As the content of g-C_3N_4 was increased from 10% to 50%, the decolorization rate of RhB was increased from 40% to 100%. This phenomenon indicated that g-C_3N_4 could enhance photocatalytic effect on $Bi_4O_5Br_2$. However, when further increasing the content of g-C_3N_4, the effect of the composite photocatalyst on RhB decolorization remained almost unchanged.

In order to analyze the kinetics of the decolorization of RhB by using g-C_3N_4/$Bi_4O_5Br_2$ composite photocatalyst, the quasi-first-order kinetic equation (Eq. 2-2) was used to fit the experimental data. The curves of $\ln(C/C_0)$~t showed a linear trend, indicating that the decolorization of RhB followed the quasi-first-order kinetic equation (Fig. 5-10(b)). Fig. 5-10(c) shows that the rate constants (k) during RhB decolorization were 0.1867, 0.2578, 0.2979, 0.3987, 0.3368, 0.3481 and 0.1987 min^{-1}, respectively, and the highest k value was obtained at the mass ratio of g-C_3N_4:$Bi_4O_5Br_2$ of 5:5. The rate constants (k) of single-phase g-C_3N_4 and $Bi_4O_5Br_2$ were lower than that of g-C_3N_4:$Bi_4O_5Br_2$ composites, indicatting that synergistic effects could be obtained by loading g-C_3N_4 on to $Bi_4O_5Br_2$.

Fig. 5-11 (a) shows the photo-degradation effect of $Bi_4O_5Br_2$, g-C_3N_4 and g-C_3N_4/$Bi_4O_5Br_2$ composite photocatalysts at different mass ratio on phenol removal, in which C is the concentration of phenol in the solution during photodegradation and C_0 is the initial phenol concentration. It can be seen that the pure $Bi_4O_5Br_2$ had a low phenol removal efficiency of only 5% after 2 hours under visible light irradiation. As for the g-C_3N_4/$Bi_4O_5Br_2$ composite photocatalyst, the phenol removal efficiency increased with the increase of g-C_3N_4 content. Similarly, when the mass ratio of g-C_3N_4:$Bi_4O_5Br_2$ was 5:5, 77% of phenol removal rate was obtained in 2 hours under visible light irridiation. This result is consistent with the result from the catalytic decolorization of RhB under visible light. In order to further understand the reaction kinetics of photocatalytic degradation of phenol, the rate constant (k) of photocatalytic degradation was also calculated. From Fig. 5-11 (b), the highest photodegradation rate constant (k) was obtained from the g-C_3N_4/$Bi_4O_5Br_2$ (5:5) composite photocatalyst, which was 30 times that of $Bi_4O_5Br_2$. This result is also in agreement with the result from RhB decolorization under visible light. With the increase of g-C_3N_4 content, the photocatalytic effect of the composite photocatalyst gets better, with highest RhB decolorization and phenol removal obtained at the mass ratio of g-C_3N_4:$Bi_4O_5Br_2$ of 5:5.

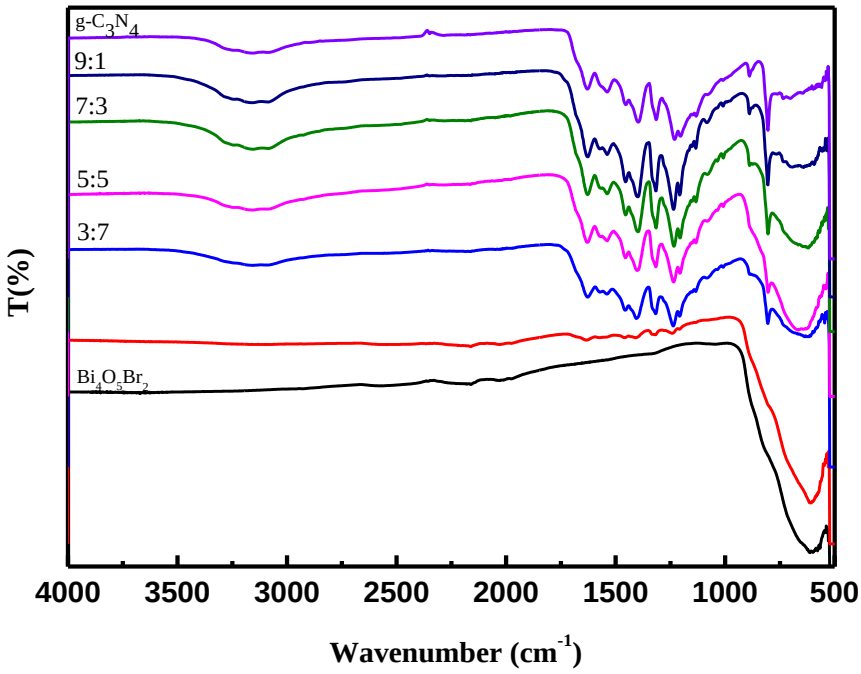

Fig. 5-1 FT-IR spectrum of photocatalyst $Bi_4O_5Br_2$, g-C_3N_4 and g-C_3N_4/$Bi_4O_5Br_2$ (1:9, 3:7, 5:5, 7:3, 9:1)

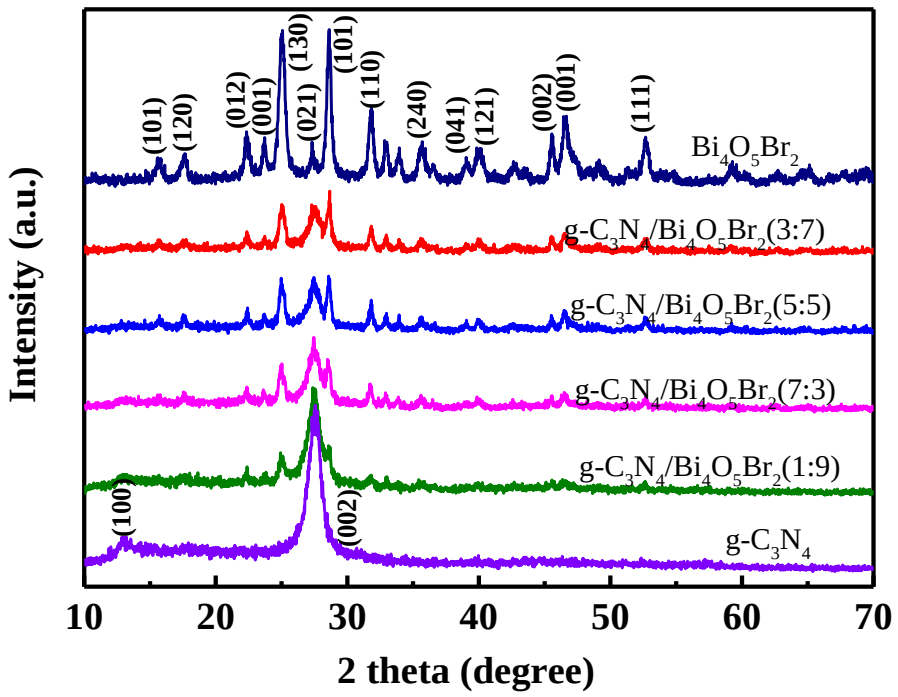

Fig. 5-2 XRD patterns of g-C_3N_4, g-C_3N_4/$Bi_4O_5Br_2$ and $Bi_4O_5Br_2$

Table 5-1 BET surface areas of g-C_3N_4, g-C_3N_4/$Bi_4O_5Br_2$(5:5) and $Bi_4O_5Br_2$

Sample	Surface area (m²/g)
g-C_3N_4	9.96
g-C_3N_4/$Bi_4O_5Br_2$ (5:5)	26.90
$Bi_4O_5Br_2$	1.77

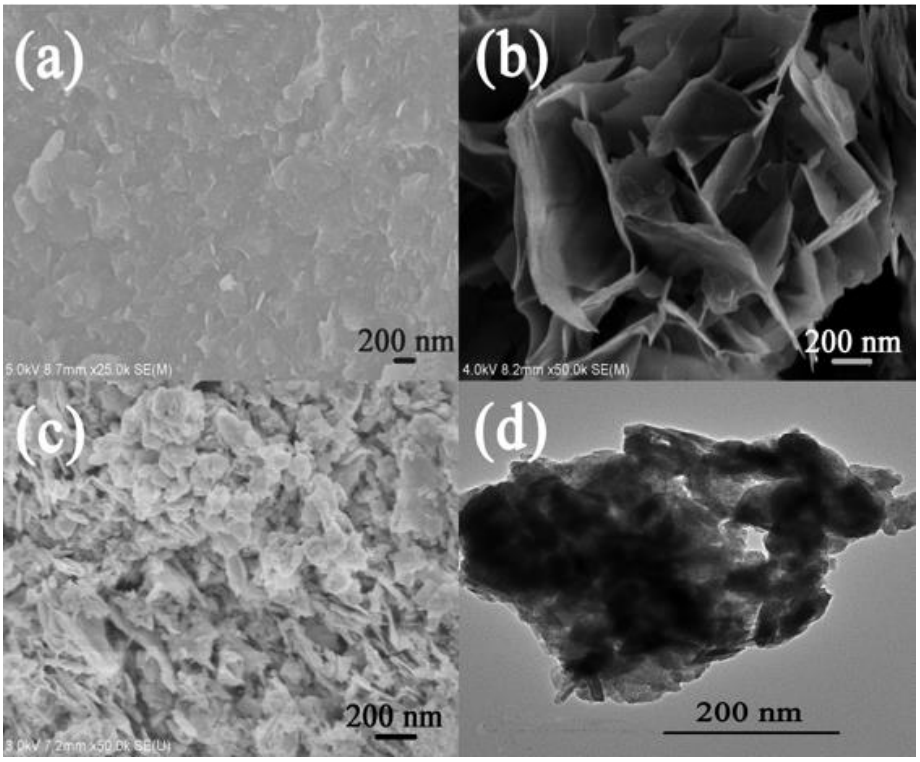

Fig. 5-3 SEM images of (a) $Bi_4O_5Br_2$, (b) g-C_3N_4 and (c) g-C_3N_4/ $Bi_4O_5Br_2$ (5:5) samples; (d)TEM image of g-C_3N_4/ $Bi_4O_5Br_2$ (5:5)

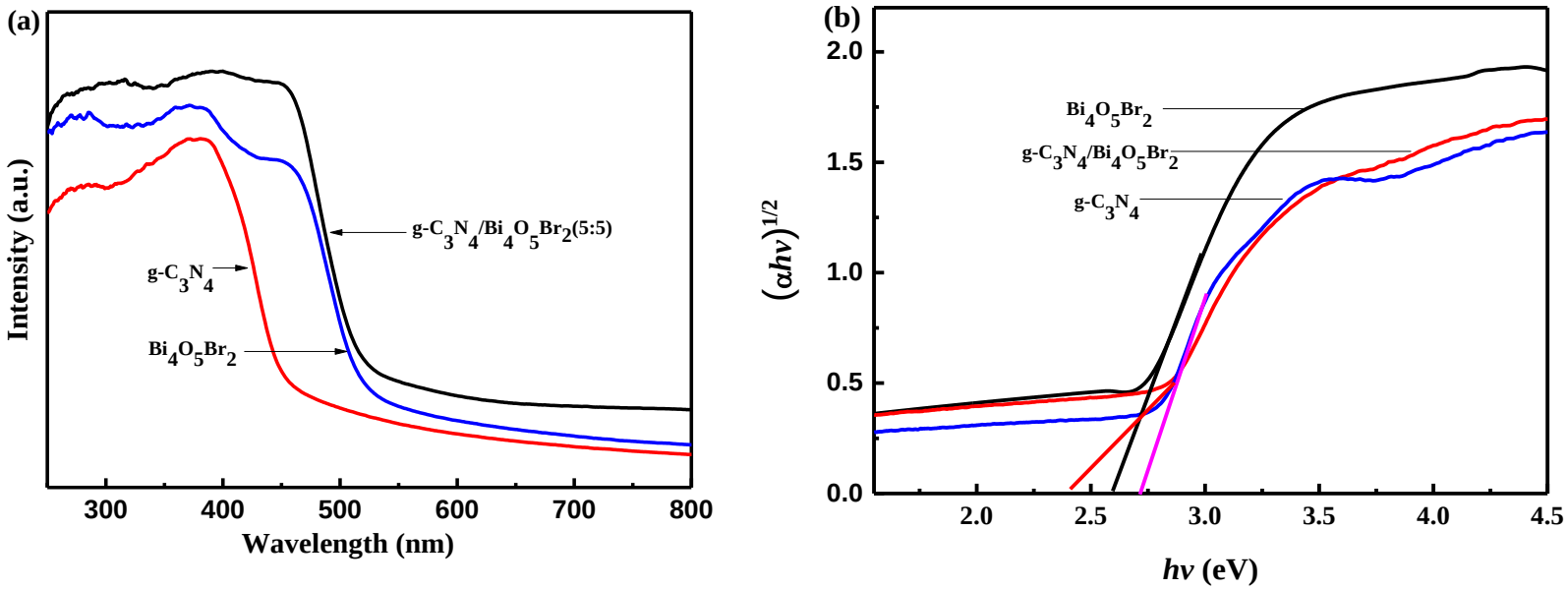

Fig. 5-4 UV–vis diffuse reflectance spectra (a) and $(\alpha h\nu)^{1/2}$ - ($h\nu$) curves (b) of samples

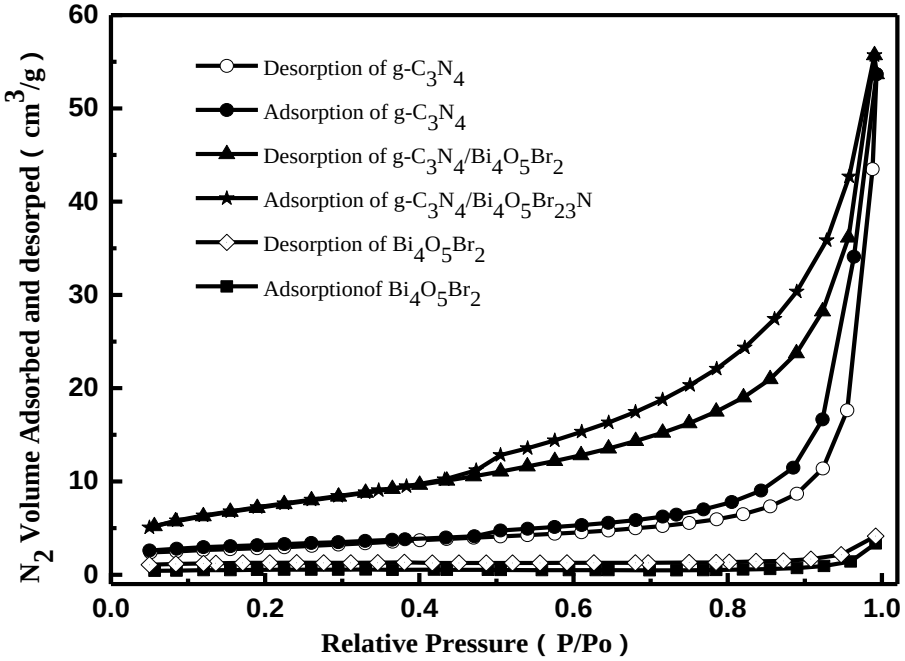

Fig. 5-5 Nitrogen adsorption and desorption isotherms of samples

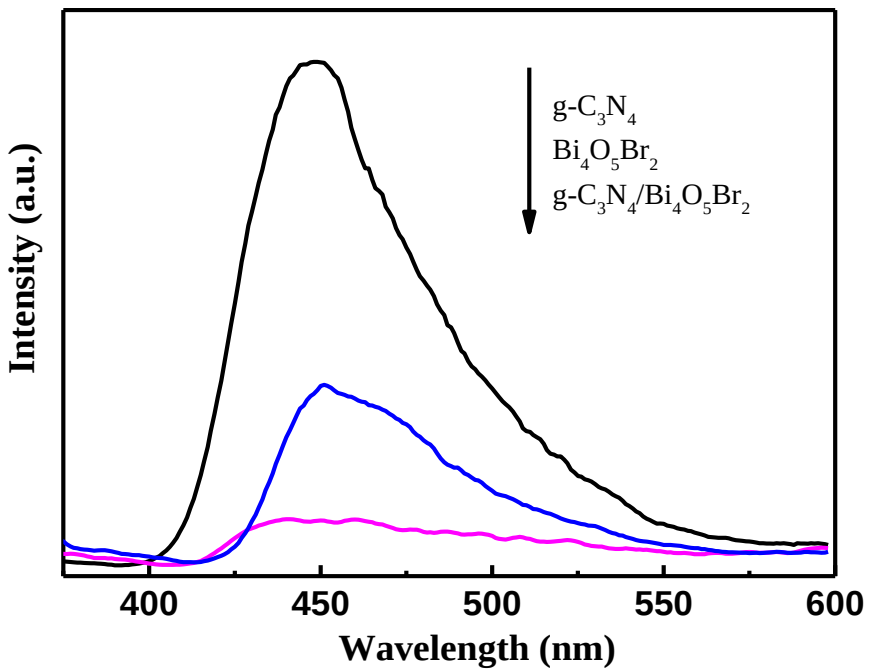

Fig. 5-6 PL spectra of $Bi_4O_5Br_2$, g-C_3N_4/$Bi_4O_5Br_2$ (5:5) and g-C_3N_4 samples

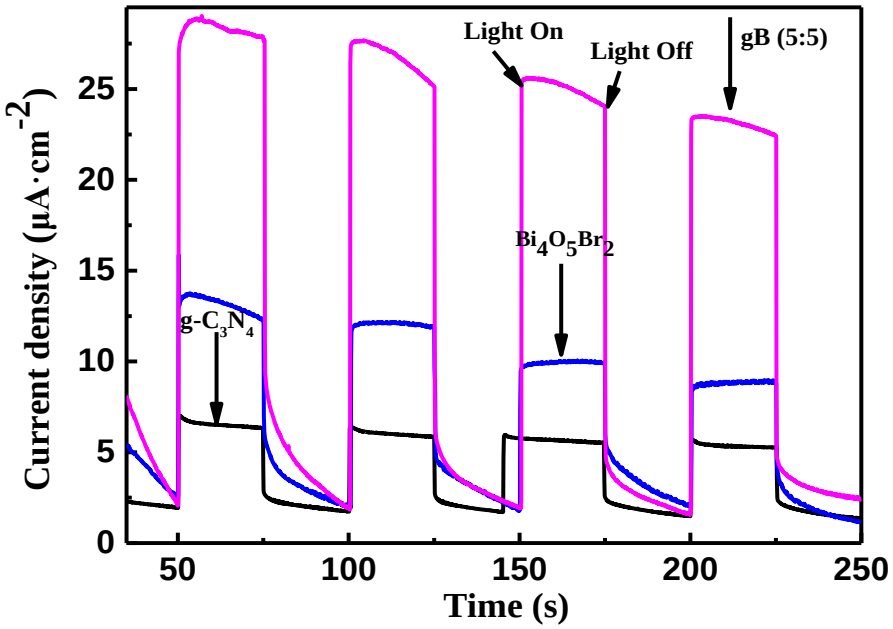

Fig. 5-7 Photocurrent response of $Bi_4O_5Br_2$, g-C_3N_4/$Bi_4O_5Br_2$ (gB, 5:5)) and g-C_3N_4 samples

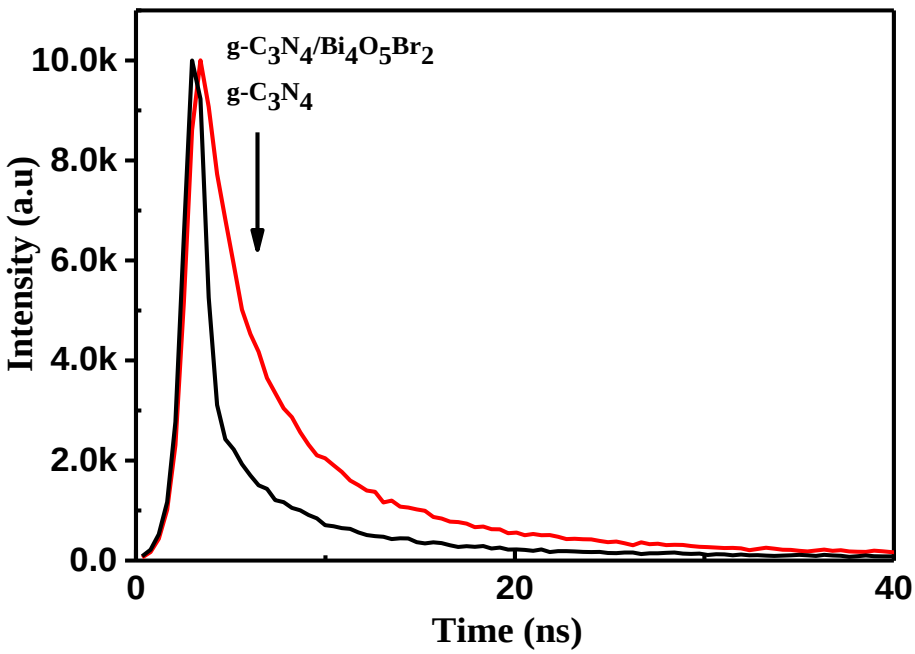

Fig. 5-8 Time-resolved fluorescence decay detected at 453 nm of g-C_3N_4 and g-C_3N_4/$Bi_4O_5Br_2$(5:5) composites

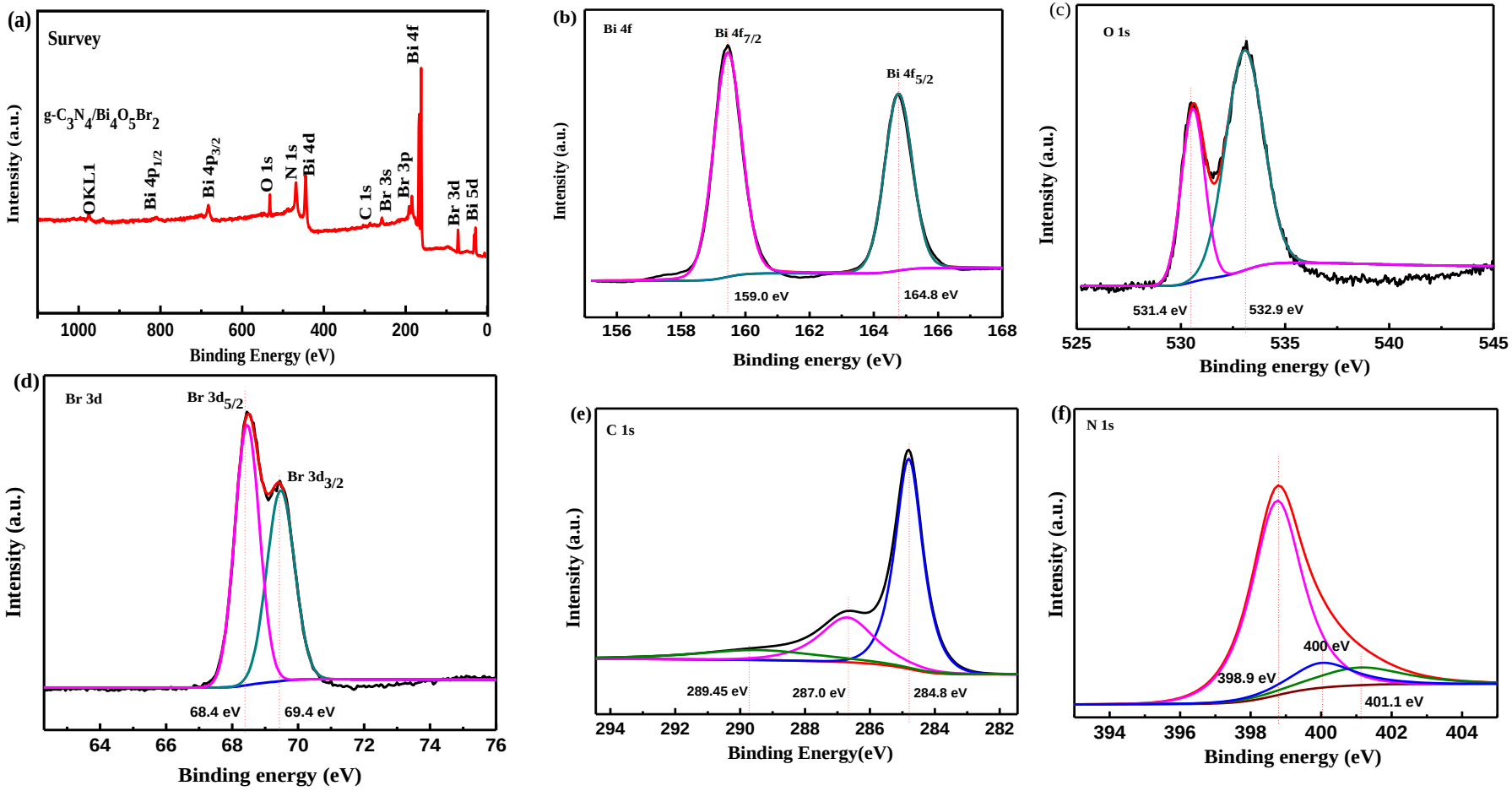

Fig. 5-9 Survey scan and high-resolution XPS spectra of the (b) Bi4f, (c) O1s and (d) Br3d, (e) C 1s, (f) N 1s regions for g-$C_3N_4/Bi_4O_5Br_2$

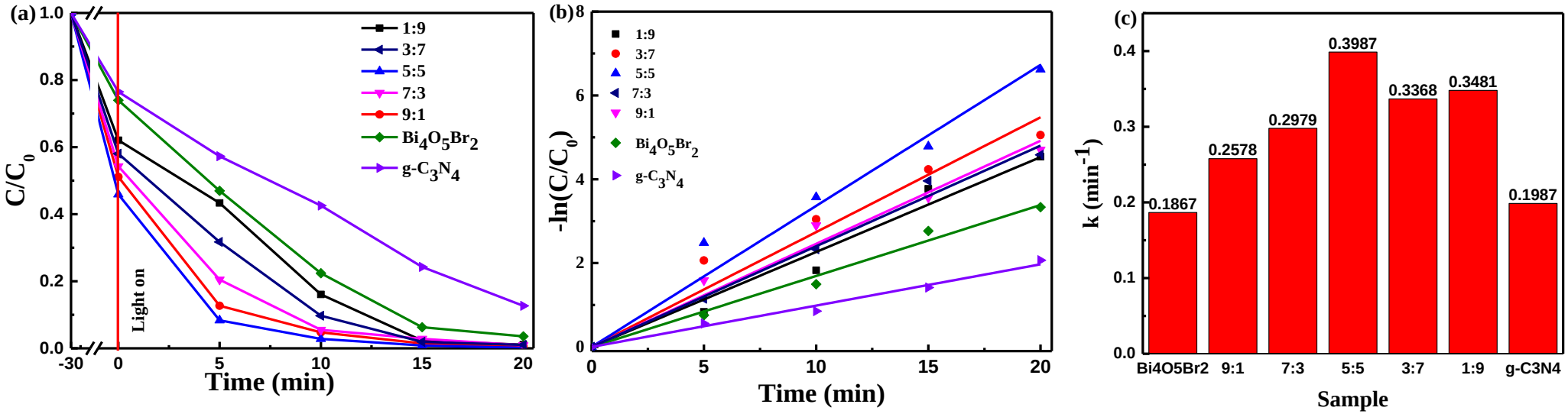

Fig. 5-10 Decolorization of RhB with different photocatalysts: (a) decolorization rate, (b) kinetics, and (c) rate constant (k)

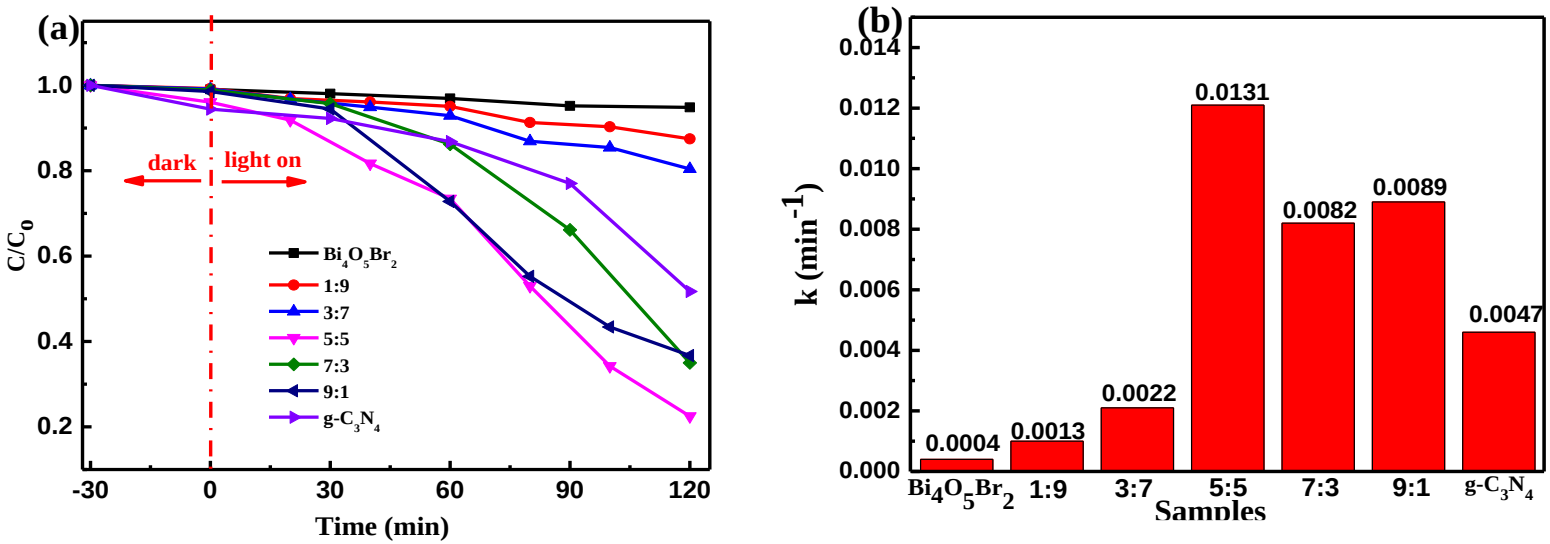

Fig. 5-11 Removal rate of phenol with different photocatalysts (a) and the rate constant (k) (b)

5.3.3 Measurement of active species during photocatalytic reaction

The synthesized samples can be excited to generate photo-generated $e^-$and h^+ under visible light irradiation during the photocatalytic process of pollutants, and e^- and oxygen are adsorbed on the surface of the sample to generate superoxide anion radicals on the CB, thereby oxidizing the adsorbed dye. Thus the toxic organics can be mineralized into CO_2 and H_2O. At the same time, h^+ on the VB could directly react with the pollutants like RhB, and form hydroxyl radicals with water molecules and hydroxyl anions. This effect can bring about indirect removal of pollutants under visible light. In order to clarify the role of various active substances in the process of pollutants removal after the catalyst absorbs light, the active species in the photocatalytic system were measured and discussed.

The free radical of •OH was determined by terephthalic acid-fluorescence spectroscopy (TA-PL) as shown in Fig. 5-12. Under visible light irradiation, •OH was captured by TA to form 2-hydroxyterephthalic acid (TAOH). The fluorescence intensity of TAOH was proportional to the concentration of •OH in the solution. A stronger fluorescence intensity denoted more •OH generated [124]. N-TiO_2 was used to compare with the synthetic g-C_3N_4/$Bi_4O_5Br_2$ composite. It can be seen that the fluorescence intensity of N-TiO_2 increased with the extension of illumination time, indicating that the •OH formed at 425 nm (Fig. 5-12(a)). However, the •OH fluorescence intensity was weak at 10 min, 15 min and 20 min (Fig. 5-12(b)), indicating that there was too little or almost no •OH formed by adding the g-C_3N_4/$Bi_4O_5Br_2$ composite in the photocatalytic system. This result sugests that •OH is not the active species in the g-C_3N_4/$Bi_4O_5Br_2$ composite reaction system. In addition, the oxidation-reduction potential of •OH/OH^- is +1.99 eV, while the VB potentials of g-C_3N_4 and $Bi_4O_5Br_2$ are +1.57 eV and +1.32 eV, respectively. That is, the E_{VB} values of both single-phase photocatalysts are lower than the oxidation-reduction potential of •OH/OH^-, meaning that h^+ could not oxidize OH^- to •OH on the CB. In summary, •OH is not the active species in this reaction system.

The free radical of •O_2 was investigated by the conversion of NBT with ultraviolet-visible spectrophotometry analyzer. The more•O_2 produced in the solution, the less amount of NBT. Results showed that the absorbance was lower, indicating that more NBT were conversed at 260 nm (Fig. 5-13). The E_{CB} of pure g-C_3N_4 is -1.13eV, and the oxidation-reduction potential of O_2/•O_2 was -0.046eV, meaning that the E_{CB} of g-C_3N_4 could easily reduce O_2 to •O_2. Therefore, it was confirmed that NBT conversion was very significant (Fig. 5-13(a)) in this reaction system. However, there was almost no change in the NBT conversion of $Bi_4O_5Br_2$ (Fig.

5-13(b)). This phenonmenon can be attributable to the E_{CB} of $Bi_4O_5Br_2$ (0.12 eV), which is positive in the O_2/O_2^- oxidation-reduction potential. Therefore, it is impossible for O_2 to be reduced to $\bullet O_2$ by the CB electron of the $Bi_4O_5Br_2$. Fig. 5-13 (c) shows a very significant NBT conversion, which is due to that the single phase photocatalyst $Bi_4O_5Br_2$ was coupled with g-C_3N_4 and the formation of composite g-C_3N_4/$Bi_4O_5Br_2$ photocatalyst. As the E_{VB} of g-C_3N_4 is more positive than the E_{VB} of $Bi_4O_5Br_2$ in the g-C_3N_4/$Bi_4O_5Br_2$, the h^+ of the VB of g-C_3N_4 is easily transferred onto the $Bi_4O_5Br_2$ VB, so that the photo-generated e^- and h^+ could be effectively separated. This is consistent with the observation from the PL spectrum. In summary, it was inferred that $\bullet O_2$ was the active species in the photocatalytic reaction of the composite g-C_3N_4/$Bi_4O_5Br_2$.

The effects of g-C_3N_4/$Bi_4O_5Br_2$ on the photocatalytic decolorization of RhB were investigated by using different free radical scavengers. In the experiments, 1 mmol iso-propanol (IPA), 1 mmol p-benzoquinone (BQ), and 1 mmol sodium oxalate (SO) were added into the RhB solution containing g-C_3N_4/$Bi_4O_5Br_2$ photocatalyst to capture •OH, $\bullet O_2$ and h^+, respectively. From Fig. 5-14, it can be seen that the effect of IPA on RhB decolorization was less as compared with the scenario of only g-C_3N_4/$Bi_4O_5Br_2$ in the RhB solution, indicating that •OH is not the active species in this reaction system. This observation is consistent with the result from the TA-PL analysis (Fig. 5-12). However, the decolorization rate of RhB was significantly reduced with BQ, indicating that $\bullet O_2$ is the main active species in this reaction system. On the other hand, the photocatalytic efficiency was significantly inhibited when the scavenger of SO was added, resulting in low RhB decolorization. This implies that h^+ plays a dominant role in the photocatalytic system. Therefore, h^+ is the main active species and $\bullet O_2$ is the secondary active species in the reaction system.

5.3.4 Stability evaluation

The stability of the catalyst is also an important factor for its practical application. RhB was used as the target pollutant by g-C_3N_4/$Bi_4O_5Br_2$ (5:5) for four cycles under visible light illumination (Fig. 5-15(a)). The results show that the catalytic activity of g-C_3N_4/$Bi_4O_5Br_2$ (5:5) was not affected, almost stable after 5 cycles of utilization. After four cycles' decolorization, the sample g-C_3N_4/$Bi_4O_5Br_2$ was again characterized by XRD patterns (Fig. 5-15(b)) and FT-IR (Fig. 5-15(c)). No impurity peak appeared and the position of the peaks was unchanged. In addition, the strength of characteristic peaks was basically unchanged after the 5 cycle's

reaction.

5.3.5 Mechanisms analysis

Based on the above analysis, the photocatalytic reaction mechanisms of $Bi_4O_5Br_2$/g-C_3N_4 was analyzed (Fig. 5-16). Before the coupling of $Bi_4O_5Br_2$ with g-C_3N_4, the Fermi level of $Bi_4O_5Br_2$ was lower than that of g-C_3N_4. Through the coupling of $Bi_4O_5Br_2$ with g-C_3N_4 by in-situ method, the CB and VB of $Bi_4O_5Br_2$ and g-C_3N_4 were migrated due to EF flat, resulting in the decline of the entire energy band of g-C_3N_4 coupled with $Bi_4O_5Br_2$. The heterostructure and IEF in $Bi_4O_5Br_2$/g-C_3N_4 were generated. Photogenerated e^- and h^+ can be excited after the absorption of visible light by $Bi_4O_5Br_2$ and g-C_3N_4. According to the migration relationship of the composite energy band, the E_{VB} of g-C_3N_4 is more positive than the E_{VB} of $Bi_4O_5Br_2$, and the h^+ of g-C_3N_4 VB could be transferred to the $Bi_4O_5Br_2$ VB to directly decompose the organics. Although the E_{CB} of g-C_3N_4 is negative compared with the E_{CB} of $Bi_4O_5Br_2$, the e^- on the g-C_3N_4 CB may be transferred into the $Bi_4O_5Br_2$ CB. This is due to the the heterojunction formed between g-C_3N_4 and $Bi_4O_5Br_2$, and thereby, e^- of g-C_3N_4 CB can reduce O_2 adsorbed and produce $\bullet O_2^-$ and then induce the oxidation reaction. At last, RhB might be decomposed into CO_2 and H_2O. Therefore, in the newly composite photocatalyst (g-C_3N_4/$Bi_4O_5Br_2$) system, the recombination of photogenerated e^- and h^+ can be significantly inhibited, resulting in accelerated separation efficiency of the photogenerated e^- and h^+.

5.3.6 Application of the composite in chromium detoxification

The new photocatalyst was also tested for its detoxification effect on Cr(VI) in this study. Fig. 5-17 shows that Cr(VI) can be transformed into stable Cr(III) under the visible light. The detoxification ability of g-C_3N_4/$Bi_4O_5Br_2$ photocatalysts for Cr(VI) was increased with the increase of $Bi_4O_5Br_2$ loading within 30 min dark at the initial solution pH7. Among all the tested photocatalysts, g-C_3N_4/$Bi_4O_5Br_2$ obtaided the best detoxification effect on Cr(VI), about 60% in dark condition (Fig. 5-17(a)). The detoxification rate of Cr(VI) was also increased with the increase of of $Bi_4O_5Br_2$ loading during the light illlustration. Compared with the single-phase g-C_3N_4 and the synthesized samples of g-C_3N_4/ $Bi_4O_5Br_2$ (3:7 and 1:9), g-C_3N_4 /$Bi_4O_5Br_2$ (5:5) obtained the best detoxicification effect on Cr(VI), about 100% within 40 min under visible light. The distribution of Cr(VI) on the surface of the synthesized photocatalyst after the first detoxification test for was analysized by XPS (Fig. 5-17(b)). The result shows that all the Cr(VI) have been transformed into stable Cr(III), indicating that the new photocatalyst has

greatpotential in the treatment of wastewater containing various pollutants.

5.4 Summary

In this chapter, the narrow band gap g-C_3N_4/$Bi_4O_5Br_2$ composite photocatalyst was successfully synthesized through the coupling of single-phase photocatalysts g-C_3N_4 with $Bi_4O_5Br_2$ by in-situ method. The high photocatalytic performance of the composite photocatalyst was confirmed by RhB decolorization, chromium detoxicification and phenol degradation. The active species generated during the photocatalytic reaction were investigated by NBT conversion, capture agent and TA-PL analysis, indicating that h^+ was the main active species and $\bullet O_2^-$ was the secondary active species during the photocatalytic process of g-C_3N_4/$Bi_4O_5Br_2$ composites.The obtained photocatalyst g-C_3N_4/$Bi_4O_5Br_2$ also has good stability after 5 times' reutilization, suggesting its high photocatalytic activity for pollutants removal.

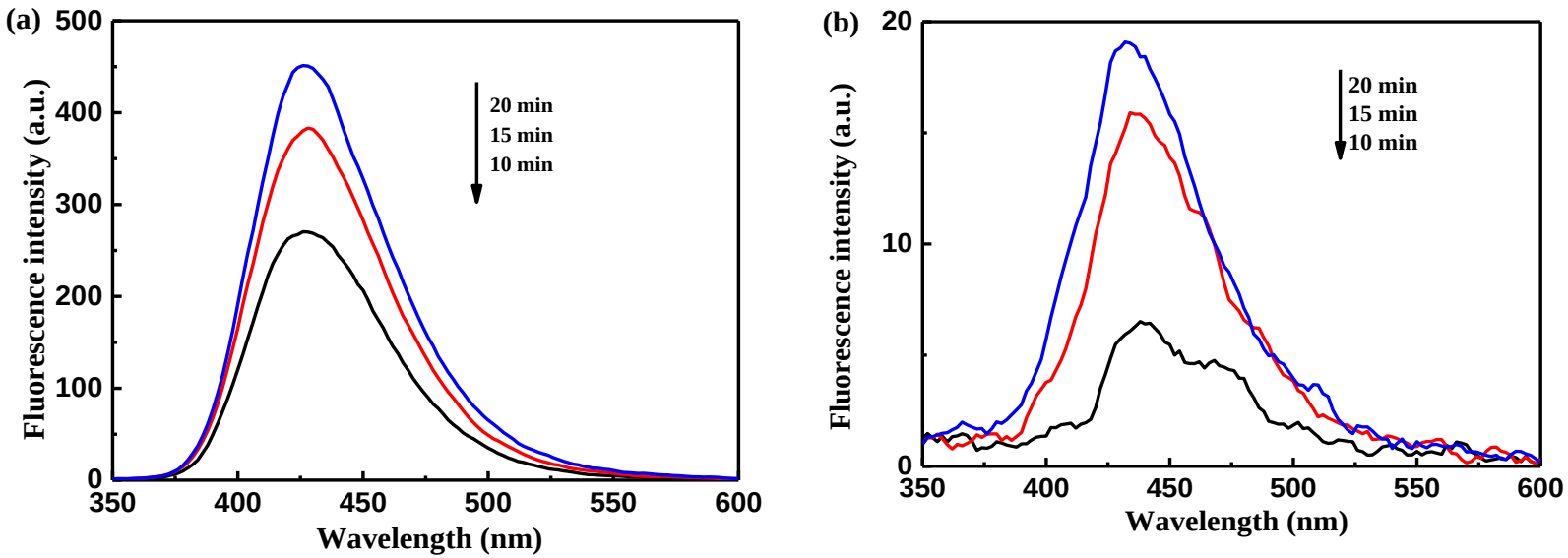

Fig. 5-12 •OH trapping in the PL spectra during irradiation by using N-TiO_2 (a) and g-C_3N_4/$Bi_4O_5Br_2$ (5:5) (b)with TA

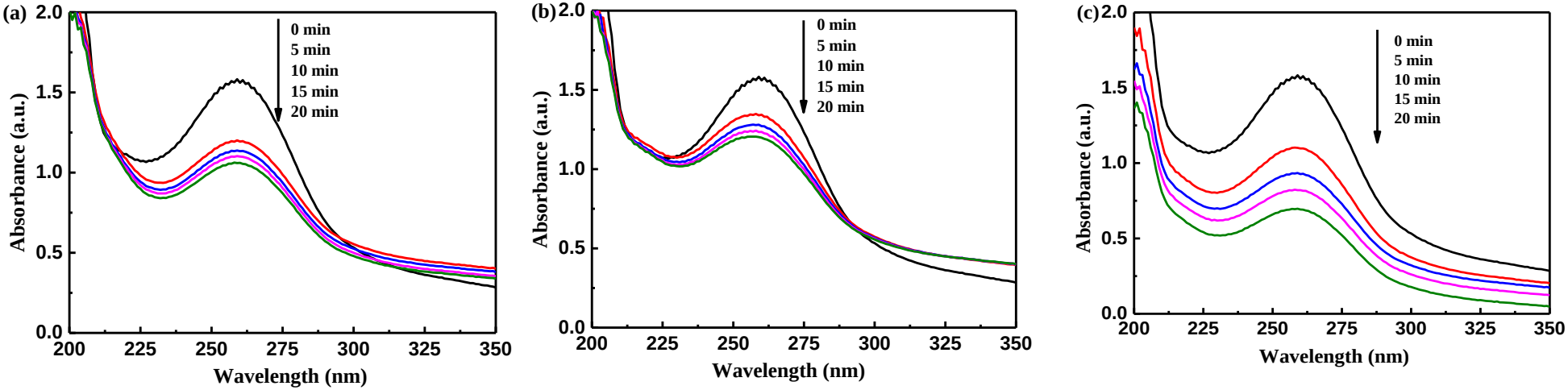

Fig. 5-13 Spectra of NBT transformation generated by g-C_3N_4 (a), $Bi_4O_5Br_2$(b) and g-C_3N_4/$Bi_4O_5Br_2$ (c) under visible light

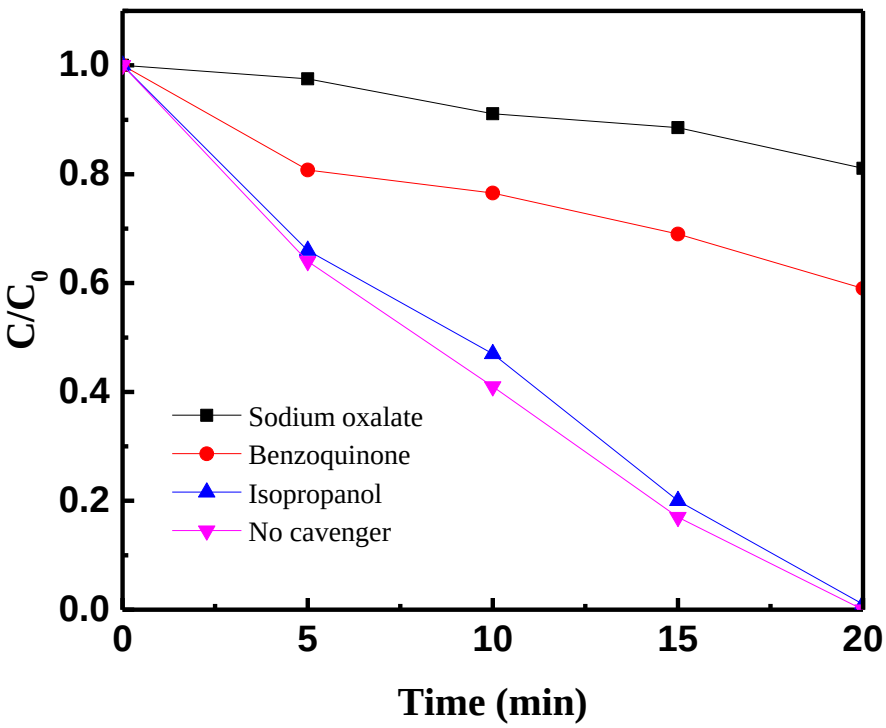

Fig. 5-14 Photocatalytic decolorization of RhB by g-C_3N_4/$Bi_4O_5Br_2$ (5:5) with different scavengers

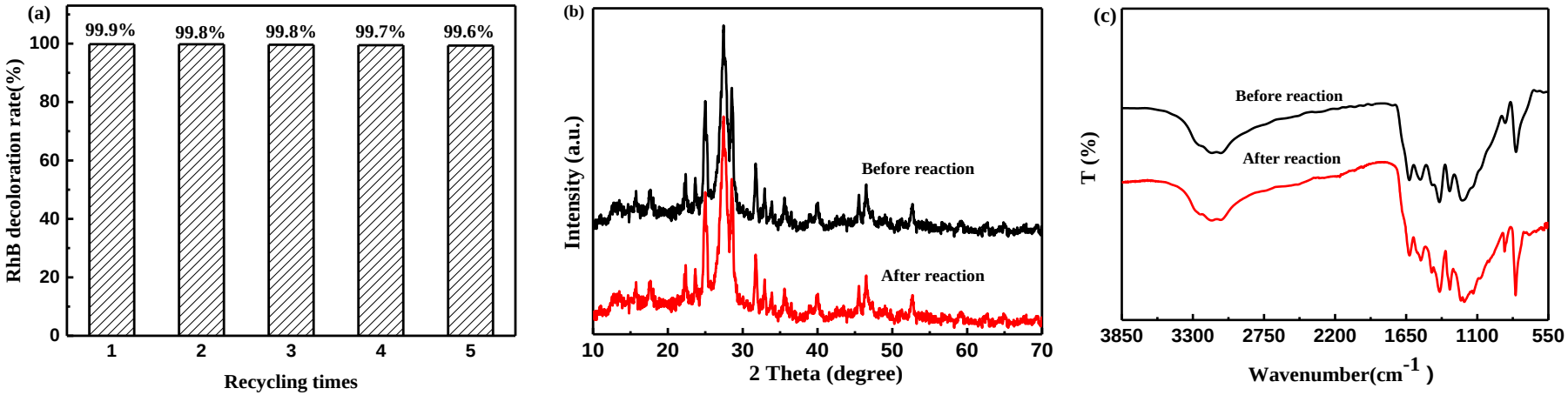

Fig. 5-15 (a) Recycling runs for the photocatalytic decolorization of RhB by using g-C_3N_4/$Bi_4O_5Br_2$ composite under visible light irradiation; (b) XRD patterns of g-C_3N_4/$Bi_4O_5Br_2$ composite before and after 4 cycles reaction, and (c) FT-IR spectra

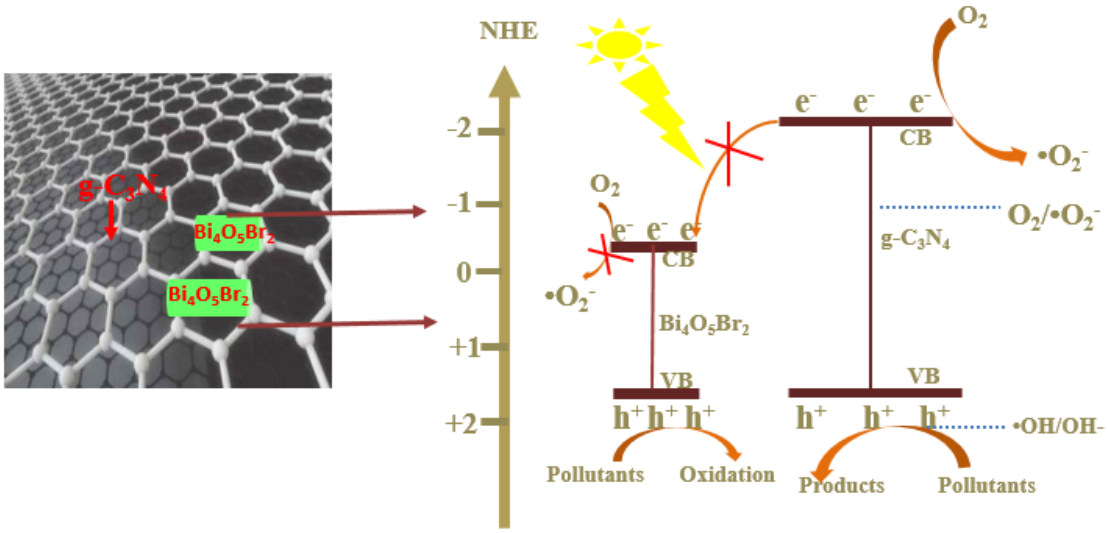

Fig. 5-16 The mechanisms involved in RhB decolorization by g-C_3N_4/$Bi_4O_5Br_2$

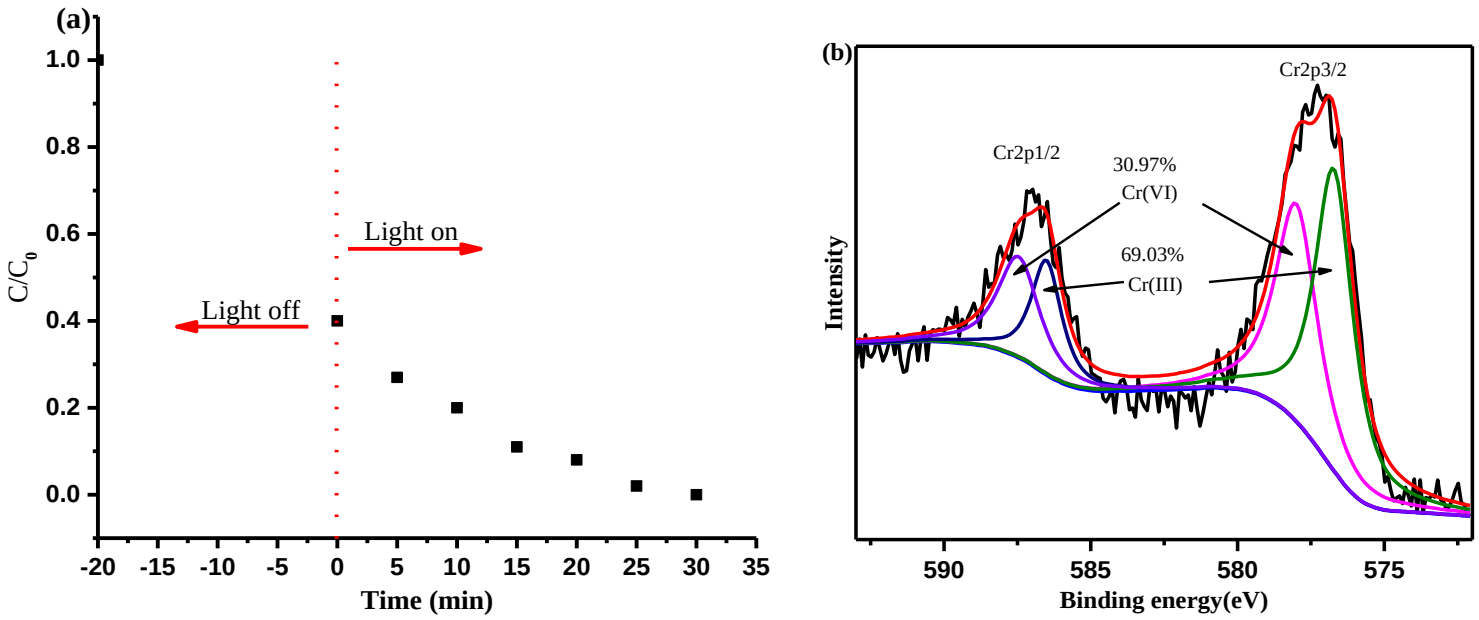

Fig. 5-17 Cr(VI) removal by the synthesized g-C_3N_4/$Bi_4O_5Br_2$ samples (a) and Cr(VI) detoxification kenetics (b) under visible light

Chapter 6 Conclusions and future research

This dissertation focused on the development of highly efficient bismuth-based photocatalysts which can be utilized in wastewater treatemmtn. All the results from Chapter 2 to Chapter 5 were summaried in this chapter (Table 6-1), including their characteristic structure and phase, optical property, photocatalytic performance and scavenging activity on SO, IPA and p-BQ during the decolorization of RhB under visible light. And their application in organics and toxicants removal was also discussed.

Table 6-1 The characteristic sand properties of the synthesized photocatalysts

Composite	**Phase**	**Optical property**	**Photocatalytic performance under visible light**
$Bi_4O_5Br_2$	Special cell and facets, dimensional flower-like nanostructure, Lattice	Ban dgap energy (2.43 eV), Red shift	100% RhB and 70% Cr(VI) removal
$Bi_4O_5Br_2$/ SBA-15	Crystal facets, Special cell, Si peak, Langmuir type IV hysteresis loops, Mesoporous	Band gap energy (3.10 eV), Red shift	100% RhB and Cr(VI), ammonium nitrogen removal, strong activity
$Bi_4O_5Br_2$/ ZrO_2-WO_3/ SBA-15	Zr high energy spectrum, IV hysteresis loops, Mesoporous, Crystal facets, IV hysteresis loops,	Band gap energy (2.69 eV), Red shift	100% RhB, ammonium nitrogen, Cr(VI), and phenol removal
g-C_3N_4/ $Bi_4O_5Br_2$	Multiple facets, Special groups, Carbon-nitrogen heterocycle, Special cell, Speciafic peaks of N-C and N-H	Band gap energy (2.30 eV), Red shift	100% RhB, Cr(VI), and phenol removal

6.1 Conclusions

Bismuth-based photocatalyst is promising in environmental protection and energy

production. This research developed new Bi-based photocatalysts by using four strategies according to its special layered structure and realized excellent property and performance in watewter treatment. The synthesized photocatalysts overcomed the problems of easy recombination of photogenerated carriers, fewer active sites and single pollutant removal.

Taking full consideration of the material's special structure, a novel $Bi_4O_5Br_2$, a polycrystalline bismuth-rich and environmental friendly material was prepared in Chapter 2, which revealed great application potential for RhB decoloration and chromium detoxification in wastewater treatment. The conclusions regarding the special structure, property and the application can be drawn as follows.

(1) A novel $Bi_4O_5Br_2$ was fabricated through breaking the layered structure by adjusting the alkalinity of synthesis system with polymer PEG-10000 as directing agent.

(2) The synthesized $Bi_4O_5Br_2$ photocatalyst possessed the special structure with poly-crystalline facets nanosheet structure and high visible light activity with the maximum light absorption at 500 nm.

(3) The new photocatalyst has good photocatalytic performance for RhB decolorization and Cr(VI) detoxification. 100% RhB solution (10 mg/L) was decolorated within 20 min, and 90% Cr(VI) was transformed into stable Cr(III) in wastewater under visible light within 120 min at an initial solution pH11.

Althogh $Bi_4O_5Br_2$ had good photocatalytic performance under visible light, its practical application was limited due to its aggragation proplem in wastewater treatment. In order to solve this problem, another strategy was adoped to enhance the specific surface area of $Bi_4O_5Br_2$ photocatalyst in Chapter 3. A mesoporous molecular sieve material SBA-15 was applied as support, and loading strategy was used as the single phase photocatalyst modification, which enhanced the photocatalytic activity. In addition, due to the special property of SBA-15, the synthsied material can realize inorganic pollutants removal simultaneously. Conclusions from this study can be drawn as follows.

(1) A novel photocatalyst $Bi_4O_5Br_2$/SBA-15 was firstly synthesized with different loadings of singl- phase $Bi_4O_5Br_2$ on SBA-15.

(2) Except for the special crystalline facets, the synthesized $Bi_4O_5Br_2$/SBA-15 also had ordered mesoporous structure with Langmuir type IV hysteresis loops and high specific surface area of 156 m^2/g.

(3) High photocatalytic performance (100% of 10 mg/L RhB decolorization within 20 min, 81.3% of ammonium nitrogen and 100% of Cr(VI) detoxitiation within 120 min) was attained

during wastewater treatment under visible light.

$Bi_4O_5Br_2$/SBA-15 composite had excellent photocatalytic performance on pollutants removal, while the separation rate of the photogenerated electrons was still unsatisfied due to the width band gap. In order to solve this problem, the strategy of tenary metal compound was applied to form narrow band gap $Bi_4O_5Br_2/ZrO_2$-WO_3/SBA-15 by introducing ZrO_2 and WO_3 onto the surface structure of mesoporous $Bi_4O_5Br_2$/SBA-15 and produce p-n heterojunction in Chapter 4. After analysis of the structure, optical property and photocatalytic performance of the newly synthesized photocatalysts, the results can be summaried as follows.

(1) A novel $Bi_4O_5Br_2/ZrO_2$-WO_3/SBA-15 was firstly prepared by using tenary metal compound.

(2) Besides the property of $Bi_4O_5Br_2$/SBA-15, the tenary metal composite $Bi_4O_5Br_2/ZrO_2$-WO_3/SBA-15 had special p-n heterojunction confirmed by Zr high energy spectrum expreesion.

(3) The $Bi_4O_5Br_2/ZrO_2$-WO_3/SBA-15 composite had good photocatalytic performance, including 100% of 10 mg/L RhB decolorization within 10 min, attributable to the n-p type heterojunction of $Bi_4O_5Br_2/ZrO_2$-WO_3/SBA-15 beneficial for the effective separation of photo-generated electron-hole pairs. The $Bi_4O_5Br_2/ZrO_2$-WO_3/SBA-15 was also stable because the RhB decolorization efficiency decreased only by 10.0% after 5 cycles' reuse. This ternary composite was found to have better decontamination effects on organic/inorganic matters under visible light. The photocatalyst had better co-catalytic performance for inorganic/organic matters, which exhibited removals of ammonium removal, Cr(VI) and phenol from the simulated waste water about 100%, 99% and 70%, respectively.

Seen from the bove results, different Bi-based composites can be obtained with high photocatalytic activity by using new strateges. However, the photogenerated electron-hole pairs was directly affected by photocurrent. Therefore, the high photocurrent photocatalyst needs to be designed by coupling the single-phase photocatalyst $Bi_4O_5Br_2$ with the semiconductor (g-C_3N_4) (Chapter 5). The conclusion can be drawn as follows.

(1) The new semiconductor photocatalyst g-$C_3N_4/Bi_4O_5Br_2$ composite can be prepared by using in-situ synthesis method.

(2) This new synthesized g-$C_3N_4/Bi_4O_5Br_2$ was found to have strong photocurrent indesity and p-n heterojunction.

(3) 100% of 10 mg/L RhB decolorization and 80% of phenol removal were achieved by g-$C_3N_4/Bi_4O_5Br_2$ within 15 and 120 min, respectively, which showed the highest photocatalytic activity at the g-C_3N_4 /$Bi_4O_5Br_2$ mass ratio of 5:5. Meanwhile, the composite possessed a large

specific surface area (26.90 m^2/g) and highly stable photocatalytic activity (99.6% of 10 mg/L RhB decolorization remained after 5 times' recycling of the used composite). In addition, the g-$C_3N_4/Bi_4O_5Br_2$ composite was also found to have 100% of detoxification effect on Cr(VI) in wastewater under visible light.

Results from this work are expected to provide new strategies and useful information for the modification of bismuth-based photocatalysts. And the scientific data of these cmposites on the removal of specific pollutants are meaniful for their practical application in wastewater treatment in the future.

6.2 Future research and suggestions

In the present study, synthesized photocatalysts showed positive effect on RhB, ammonium, phenol and chromium removal. The investigation on the morphology, XRD pattern, optical property, photocatalytic performance, stability of synthesized photocatalyst during the synthesis and application process, the mechanisms can be elucidated to a great extent. However, because of the special structure of bismuth-based photocatalyst, there is still a long way to apply the modified photocatalysts into practice to treat the complex wastewaters. In the future, more research work should be done with respect to the following aspects.

(1) To achieve its cost-effectiveness and high efficincy recovery of the photocatalysts after applied in wastewater treatment through the introduction of magnetic metal to change the internal structure and form magnetic field.

(2) Due to the aggregation of $Bi_4O_5Br_2/ZrO_2$-WO_3/SBA-15, the practical application of the synthesized photocatalyst will be limited by active sites. In addition, the recovery of $Bi_4O_5Br_2/ZrO_2$-WO_3/SBA-15 is difficult. Therefore, to design magnetic interpenetrating network co-catalyst for the co-existing multiple pollutants removal will be of great importance.

(3) Althogh g-$C_3N_4/Bi_4O_5Br_2$ has better photocatalytic performance than other photocatalysts, the staggered p-n heterojunction is very difficult in the synthesis process. In addition, the mechanism of interaction of three metals during synthesis processing remains unclear. From this viewpoint, the optimal condition of staggered p-n heterojunction photocatalyst and the formation principles in different types of g-$C_3N_4/Bi_4O_5Br_2$ during synthesis process will be researched. The value of g-$C_3N_4/Bi_4O_5Br_2$ photocatalyst needs to be evaluated taking its practical application in wastewater treatment into consideration.

(4) The impact of nanoparticles on the environment has always been a mystery due to the distribution of particles can not be completely recovered during wastewater treatment. When

environmental toxicology being considered, excellent carriers should be found for the particles of $Bi_4O_5Br_2$ photocatalyst, such as glass fibers, aluminum sheets and membrane. The experiments can be done by selecting different carriers using different sysnthesis conditions, and then apply the new photocatalysts for the target pollutants removal. The characteristics and photocatalytic performance of the new photocatalyst can be analyzed by different methods. The result will be more direct and meaningful for the toxicity of photocatalyst in the environment.

References

[1] Gogate P., Pandit A., A review of imperative technologies for wastewater treatment II: hybrid methods. Adv. Environ. Res., 2004, 8(3-4): 553-597.

[2] Hoffmann M., Choi W., Bahnemann D., Environmental applications of semiconductor photocatalysis, Chem. Rev., 1995, 95(1): 69-96.

[3] Fu Y., Shen P., Hu Z., Sun C., Guo R., Jiang Q., The role of CuO–TiO_2 additives in the preparation of high-strength porous alumina scaffolds using directional freeze casting, J. Porous Mat., 2015, 2: 1-9.

[4] Zhang Q., Zhang T., He T., Li C., Removal of crystal violet by clay/PNIPAm nanocomposite hydrogels with various clay contents, Appl. Clay Sci., 2014, 90(90): 1-5.

[5] Rane N., Chandanshive V., Khandare R., Gholave A ., Yadav S., Govindwar S., Green remediation of textile dyes containing wastewater by Ipomoea hederifolia L, RSC Adv., 2014, 4(69): 36623-36632.

[6] Olusegun S. J., Lima L.F., Mohallem N. D. S., Enhancement of adsorption capacity of clay through spray drying and surface modification process for wastewater treatment, Chem. Eng. J., 2018, 334:1719-1728.

[7] Jeyakumar R., Chandrasekaran V., Adsorption of lead (II) ions by activated carbons prepared from marine green algae: equilibrium and kinetics studies, Int. J. Ind. Eng. Chem., 2014, 5(1):1-9.

[8] Zhao Q., Li X., Inhibition of microbial activity by ammonia-nitrogen in landfill leachate, Environ. Pollut. Control, 1998, 20(6):1- 4. (in Chinese)

[9] Li Y., Luo G., Dai Y., Phenol Removal from Aqueous Solution Through Hollow Fiber Membrane Extraction, Chinese Chem. Eng., 1999, 7(2):104-109.

[10] Chong M., Jin B., Chow C., Saint C., Recent developments in photocatalytic water treatment technology: A review, Water Res., 2010, 44(10): 2997-3027.

[11] Chen C., Ma W., Zhao J., Semiconductor-mediated photodegradation of pollutants under visible-light irradiation, Chem. Soc. Rev., 2010, 39:4206.

[12] Ma Y., Wang X., Jia Y., Chen X., Han H., Li C, Titanium dioxide-based nanomaterials for photocatalytic fuel generations, Chem. Rev., 2014, 114:9987.

[13] Chang X., Wang T., Gong J, CO_2 photo-reduction: insights into CO_2 activation and reaction on surface of photocatalysts, Energy Environ. Sci., 2016, 9:2177.

[14] Schrauzer G. N., Guth T. D, Photolsis of water and photoreduction of nitrogen on titanium dioxide, J. Am. Chem. Soc.,1977, 99:7189.

[15] Lang X., Ma W., Chen C., Ji H., Zhao J, Selective aerobic oxidation mediated by TiO_2 photocatalysis, Acc. Chem. Res., 2014, 47:355-363.

[16] Fujishima A., Honda K., Electrochemical photolysis of water at a semiconductor electrode, Nature, 1972, 238: 37-38.

[17] Bard A., Photoelectrochemistry and heterogeneous photo-catalysis at semiconductors, J. Photochem., 1979, 10(1): 59-75.

[18] Bard A., Photoelectrochemistry, Science, 1980, 207(4427): 139-144.

[19] Bard A., Design of semiconductor photoelectrochemical systems for solar energy conversion, J. Phys. Chem., 1982, 86(2):172-177.

[20] Carey J., Lawrence J., Tosine H., Photodechlorination of PCB's in the presence of titanium dioxide in aqueous suspensions, B Environ. Contam. Tox., 1976, 16(6): 697-701.

[21] Kumar S. G., Devi L. G., Review on modified TiO_2 photocatalysis under UV/visible light: selected results and related processes on interfacial charge carrier transfer dynamics, J. Phys. Chem. A, 2011, 115 (46):13211 - 41.

[22] Chen Y., Dionysiou D. D., Effect of calcination temperature on the photocatalytic activity and adhesion of TiO_2 fi lms prepared by the P25 powder-modifi ed sol-gel method, J. Mol. Catal. A: Chem., 2006, 244 (1): 73-82.

[23] Xiao J., Rabeah J., Yang J, Xie Y., Fast electron transfer and •OH formation: key features for high activity in visible-light-driven ozonation with C_3N_4 catalysts, ACS Catal., 2017, 7(17): 6198-6206.

[24] Tong H., Ouyang S., Bi Y., Umezawa N., ChemInform abstract: nano-photocatalytic materials: possibilities and challenges, Adv. Mater., 2012, 24: 229-251.

[25] Zhou W, Li W, Wang J., Qu Y., Ordered mesoporous black TiO_2 as highly efficient hydrogen evolution photocatalyst, J. Am. Chem. Soc., 2014, 136(26): 9280-9283.

[26] Jungwon K, Platinized WO_3 as an environmental photocatalyst that generates •OH radicals under visible light, Chem. Soc. Rev., 2010, 44(17): 6849-6854.

[27] Liu T., Liao H., Lin C., Hu S., Chen S., Biofunctional ZnO nanorod arrays grown on flexible substrates, Langmuir, 2006, 22(13): 5804-5809.

[28] Zhao J., Lv X., Wang X., Yang J., Yang X., Lu X., Fabrication of BiOX (X=Cl, Br, and I) nanosheeted films by anodization and their photocatalytic properties, Mater. Lett., 2015, 158: 40-44.

[29] Ahern J. C., Fairchild R., Thomas J. S., Jordan C., Patterson H. H., Characterization of BiOX compounds as photocatalysts for the degradation of pharmaceuticals in water, Appl. Catal. B: Environ., 2015, 179: 229-238.

[30] Tang.R., Su H., Duan S., Sun D., Enhanced visible-light-driven photocatalytic performances using Bi_2WO_6/MS (M=Cd, Zn) heterostructures: facile synthesis and their photocatalytic mechanisms, RSC Adv., 2015, 5(52): 41949-41960.

[31] Li C., Chen G., Sun J., Rao J., Han Z., Hu Y., Zhou Y., A novel mesoporous single-crystal-like Bi_2WO_6 with enhanced photocatalytic activity for pollutants degradation and oxygen production, ACS Appl. Mater. Inter., 2015, 7(46): 25716-25724.

[32] Di J., Xia J., Ji M., Li H., Xu H., Li H., Chen D., The synergistic role of carbon quantum dots for the improved photocatalytic performance of Bi_2MoO_6, Nanoscale, 2015,7(26): 11433-11443.

[33] Jin B., Jiao Z., Bi Y., Efficient charge separation between Bi_2MoO_6 nanosheets and ZnO nanowires for enhanced photoelectrochemical properties, J. Mater. Chem. A, 2015, 3(39): 19702-19705.

[34] Wang P., Huang B., Qin X., Zhang X., Dai Y., Wei J., Whangbo M., Ag@ AgCl: a highly efficient and stable photocatalyst active under visible light, Angew. Chem., 2008, 47(41): 7931-7933.

[35] Sun Y., Qu B., Liu Q., Gao S., Yan Z., Yan W., Pan B., Wei S., Xie Y., Highly efficient visible-light-driven photocatalytic activities in synthetic ordered monoclinic $BiVO_4$ quantum tubes–graphene nanocomposites, Nanoscale, 2012, 4 (12): 3761-3767.

[36] Ma D., Zhou S., Hu X., Jiang Q., Huang S., Hierarchical BiOI and hollow Bi_2WO_6 microspheres: topochemical conversion and photocatalytic activities, Mater. Chem. Phys., 2013, 140(1): 11-15.

[37] Zhang L., Xu T., Zhao X., Zhu Y., Controllable synthesis of Bi_2MoO_6 and effect of morphology and variation in local structure on photocatalytic activities, Appl. Catal. B: Environ., 2010, 98(3): 138-146.

[38] Hou D., Luo W., Huang Y., Yu J., Hu X., Synthesis of porous $Bi_4Ti_3O_{12}$ nanofibers by electrospinning and their enhanced visible-light-driven photocatalytic properties, Nanoscale, 2013, 592: 2028-2035.

[39] Liu Y., Zhang M., Li L., Zhang X., In situ ion exchange synthesis of the $Bi_4Ti_3O_{12}/Bi_2S_3$ heterostructure with enhanced photocatalytic activity, Catal. Commun., 2015, 60: 23-26.

[40] Li Z., Shen Y., Yang C., Lei Y., Guan Y., Lin Y., Liu D., Nan C., Significant enhancement

in the visible light photocatalytic properties of $BiFeO_3$-graphene nanohybrids, J. Mater. Chem. A, 2013, 1: 823-829.

[41] Di L., Yang H., Hu G., Xian T., Ma J., Li R., Li Z., Enhanced photocatalytic activity of particles by surface decoration with Ag nanoparticles, J. Mater. Sci. Mater. Electron., 2014, 25: 2463-2469.

[42] Jin W., Wu Y., Chen Z., Lu Z., Solvothermal fabrication of $Bi_2Fe_4O_9$ and its photocatalytic properties, Rare Metal Mater. Eng., 2015, 44: 657-661.

[43] Zhang Q., Gong W., Wang J., Ning X., Wang Z., Zhao X., Ren W., Zhang Z., Size dependent magnetic, photoabsorbing, and photocatalytic properties of single crystalline $Bi_2Fe_4O_9$ semiconductor nanocrystals, J. Phys. Chem. C, 2011, 115: 25241–25246.

[44] Sun S., Wang W., Xu H., Zhou L., Shang M., Zhang L., $Bi_5FeTi_3O_{15}$ hierarchical microflowers: hydrothermal synthesis, growth, mechanism, and associated visible-light-driven photocatalysis, J. Phys. Chem. C, 2008, 112: 17835-17843.

[45] Zhao J., Lv X., Wang X., Yang J., Yang X., Lu X., Fabrication of BiOX (X = Cl, Br, and I) nanosheeted films by anodization and their photocatalytic properties, Mater. Lett., 2015, 158: 40-44.

[46] Song J., Mao C., Niu H., Shen Y., Zhang S., Hierarchical structured bismuth oxychlorides: self-assembly from nanoplates to nanoflowers via a solvothermal route and their photocatalytic properties, Cryst. Eng. Comm., 2010, 12:3875-3881.

[47] Zhao L., Zhang X., Fan C., Liang Z., Han P., First-principles study on the structural, electronic and optical properties of BiOX (X = Cl, Br, I) crystals, Physica B., 2012, 407(17): 3364-3370.

[48] Zhang K., Liang J., Wang S., Liu J., Ren K., Zheng X., Luo H., Peng Y., Zou X., Bo X., Li J., Yu X., BiOCl sub-microcystals induced by citric acid and the high photocatalytic activities. Cryst. Growth, 2012, 12(2): 793-803.

[49] Chen G., Fang G., Tang G., Photoluminescence and photocatalytic properties of BiOCl and $Bi_{24}O_{31}Cl_{10}$ nanostructures synthesized by electrolytic corrosion of metal Bi, Mater. Res. Bull., 2013, 48(3): 1256-1261.

[50] Zhang K., Liu C., Liu C., Huang F., Zheng C., Wang W., Study of the electronic structure and photocatalytic activity of the BiOCl photocatalyst, Appl. Catal. B: Environ., 2006, 68:125-129.

[51] Huang W., Zhu Q., Electronic structures of relaxed BiOX (X = F, Cl, Br, I) photocatalysts. Comp. Mater. Sci., 2008, 43 (4):1101-1108.

[52] Liu Y., Li J., Zhou B., Li X., Chen H., Chen Q., Wang Z., Li L., Wang J., Cai W., Efficient electricity production and simultaneously wastewater treatment via a high-performance photocatalytic fuel cell, Water Res., 2011, 45(13):3991-3998.

[53] Cheng H., Huang B., Dai Y., Engineering BiOX (X = Cl, Br, I) nanostructures for highly efficient photocatalytic applications, Nanoscale, 2014, 6(4):2009-2026.

[54] Shang M., Wang W., Zhang L., Preparation of BiOBr lamellar structure with high photocatalytic activity by CTAB as Br source and template, J. Hazard. Mater., 2009, 167(1-3):803-809.

[55] Feng Y., Li L., Li J., Wang J., Liu L., Synthesis of mesoporous BiOBr 3D microspheres and their photodecomposition for toluene, J. Hazard. Mater., 2011, 192 (2):538-544.

[56] Zhang T., Chu S., Li J., Wang L., Efficient Degradation of aqueous carbamazepine by bismuth oxybromide-activated peroxide oxidation, Appl. Catal. A: General. 2011, 397:192-200.

[57] Huo Y., Zhang J., Miao M., Jin Y., Solvothermal synthesis of flower-like BiOBr microspheres with highly visible-light photocatalytic performances, Appl. Catal. B: Environ., 2012, 111: 334-341.

[58] Zhang D., Li J., Wang Q., Wu Q., High {001} facets dominated BiOBr lamellas: facile hydrolysis preparation and selective visible-light photocatalytic activity, J. Mater. Chem. A, 2013, 1(30):8622-8629.

[59] Gu Y., Zhao L., Yang M., Xiong Y., Wu J., Zhou M., Yan J., Preparation and characterization of highly photocatalytic active hierarchical BiOX (X=Cl, Br, I) microflowers for rhodamine B degradation with kinetic modelling studies, J. Cent. South Univ., 2015, 179: 229-238. (in Chinese)

[60] Song J., Mao C., Niu H., Shen Y., Zhang S., Hierarchical structured bismuth oxychlorides: self-assembly from nanoplates to nanoflowers via a solvothermal route and their photocatalytic properties, Cryst. Eng. Comm., 2010, 12:3875-3881.

[61] Huo Y., Zhang J., Miao M., Jin Y., Solvothermal synthesis of flower-like BiOBr microsphere with highly visible light photocatalytic performance, Appl. Catal. B-Environ., 2012, 111-112: 334-341.

[62] Feng Y., Li L., Li J., Wang J., Liu L., Synthesis of mesoporous BiOBr 3D microsphere and their photodecomposition for toluene, J. Hazard. Mater., 2011, 192:538-544.

[63] Bai Y., Chen T., Wang P., Wang L., Ye L., Bismuth-rich $Bi_4O_5X_2$ (X = Br, and I) nanosheets

with dominant {101} facets exposure for photocatalytic H_2 evolution, Chem. Eng. J., 2016, 304:454–460.

[64] Jiang J., Zhao K., Xiao X., Zhang L., Synthesis and facet-dependent photoreactivity of BiOCl single-crystalline nanosheets, J. Am. Chem. Soc., 2012, 134(10): 4473-4476.

[65] Yin B., Liu C., Convenient synthesis and enhanced photocatalytic activity of BiOI/BiOBr nanostructures with different Morphologies, J nanosci nanotech., 2018, 18(7): 4771-4779.

[66] Wang J., Yu Y., Zhang L., Highly efficient photocatalytic removal of sodium pentachlorophenate with Bi_3O_4Br under visible ligh, Appl. Catal. B-Environ. 2013, 136-137:112–121.

[67] Song J., Zhang L. Yang J., Huang X., Hu J., Hierarchical porous $Bi_{24}O_{31}Br_{10}$ microarchitectures assembled by ultrathin nanosheets with strong adsorption and excellent photocatalytic performances, Mater. Design, 2017, 5:128-136.

[68] Jing L., Zhou W., Tian G., Fu H., Surface tuning for oxide-based nanomaterials as efficient photocatalysts, Chem.Soc. Rev., 2013, 42(24): 9509-9549.

[69] Di J., Xia J., Ji M., Yin S., Li H., Xu H., Zhang Q., Li H., Controllable synthesis of $Bi_4O_5Br_2$ ultrathin nanosheets for photocatalytic removal of ciprofloxacin and mechanism insight, J. Mater. Chem. A, 2015, 3:15108–15118.

[70] Athanasopoulos S., Tscheuschner S., Bassler H., Kohler A., Efficient charge separation in organic photovoltaics through incoherent hopping, Mesoscale and Nanoscale Physics, 2016, 2:1-5.

[71] Martin S., Ulrich A., Philipp S., Li Y., Hou W., Schmid M., Selloni A., Diebold U., Reaction of O_2 with subsurface oxygen vacancies on TiO_2 anatase (101), Science, 2013, 341(6149): 988-991.

[72] Pan X., Yang M., Fu X., Zhang N, Xu Y., Defective TiO_2 with oxygen vacancies: synthesis, properties and photocatalytic applications, Nanoscale, 2013, 5(9): 3601-3614.

[73] Liu J., Li H., Du N., Song S., Synthesis, characterization, and visible-light photocatalytic activity of BiOI hierarchical flower-like microspheres, RSC Adv., 2014, 4 (59):31399.

[74] Lin H., Zhao Y., Wang Y., Cao J., Chen S., Controllable in-situ synthesis of Ag/BiOI and Ag/AgI/BiOI composites with adjustable visible light photocatalytic performances, Mater. Lett., 2014, 132:141-144.

[75] Jiang G., Wang R., Wang X., Xi X., Novel highly active visible-light-induced photocatalysts based on BiOBr with Ti and Ag decorating, ACS Appl. Mater. Inter., 2012, 4(9):922−927.

[76] Pare B., Sarwan B., Jonnalagadda S. B., Photocatalytic mineralization study of malachite green on the surface of Mn-doped BiOCl activated by visible light under ambient condition, Appl. Surf. Sci., 2011, 258:247−253.

[77] Cao X., Yin Z., Zhang H., Three-dimensional graphene materials: preparation, structures and application in supercapacitors, Energ. Environ. Sci., 2014, 7:1850−1865.

[78] Wang D., Wang Y., Zhang H., Deng L., Zhang C., Han X., Hou Y., Spontaneous emission of terbium complex in−filled in single−crystal colloidal multilayer, J. Nanosci. Nanotechnol., 2008, 8 (3):1371−1374.

[79] Yang F., Liu D., Wang T., Li W., Hu W., Zhou X., Construction of Ag/AgCl nanostructures from Ag nanoparticles as high-performance visible-light photocatalysts, J. Nanopart. Res., 2016, 18:335-339.

[80] Wang P., Qi C., Hao L., Wen P., Xu X., Sepiolite/Cu_2O/Cu photocatalyst: preparation and high performance for degradation of organic dye, J. Mater., Sci., Tech., 2019, 35(3):285-291

[81] Ye L., Su Y., Jin X., Xie H., Zhang C., Recent advances in BiOX (X = Cl, Br and I) photocatalysts, Environ. Sci.: Nano., 2014, 1:90-94.

[82] Xiong W., Zhao Q., Zhang D., One step synthesis of flower-like Ag/AgCl/BiOCl composite with enhanced visible-light photocatalytic activity, Catal Comm., 2011, 16:229-233.

[83] Ye L., Liu J., Gong C., Tian L., Peng T., Zan L., Two different roles of metallic Ag on Ag/AgX/BiOX (X=Cl, Br) visible light photocatalyst: surface plasmon resonance and Z scheme bridge, ACS Catal., 2012, 2:1677-1683.

[84] Jiang J., Zhao K., Xiao X., Zhang L., Synthesis and facet-dependent photoreactivity of BiOCl single-crystalline nanosheets, J. Am. Chem. Soc., 2012, 134(10): 4473-4476.

[85] Li J, Zhang L., Li Y., Yu Y., Synthesis and internal electric field dependent photoreactivity of Bi_3O_4Cl single-crystalline nanosheets with high {001} facet exposure percentages, Nanoscale, 2014, 6(1):167-171.

[86] Lang X., Chen X., Zhao J., Heterogeneous visible light photocatalysis for selective organic transformations, Chem. Soc. Rev., 2014, 43(1):473-486.

[87] Li H., Cui Y., Hong W., High photocatalytic performance of BiOI/Bi_2WO_6 toward toluene and reactive brilliant red, Appl. Surf. Sci., 2013, 264:581-588.

[88] Fu J., Tian Y., Chang B., Lu J., Fu J., Hydrothermal synthesis of graphitic carbon nitride-

Bi_2WO_6 heterojunctions with enhanced visible light photocatalytic activities, J. Mater. Chem., 2012, 22(39): 21159-21166.

[89] Kong L., Jiang Z., Lai H., Nichollset Rebecca J., Xiao T., Jones M. O., Edwards P. P., Unusual reactivity of visible-light-responsive AgBr-BiOBr heterojunction photocatalysts, J. Catal., 2012, 293(18):116-125.

[90] Jiang J., Zhang X., Sun P., Zhang L., ZnO/BiOI heterostructures: photoinduced charge-transfer property and enhanced visible-light photocatalytic activity, J. Phys.Chem. C, 2011, 115 (42):20555-20564.

[91] Zhang D., Chen L., Xiao C., Feng J., Liao L., Wang Z., Wei T., Facile synthesis of high {001} facets dominated BiOCl nanosheets and their selective dye-sensitized photocatalytic activity induced by visible light, J. Nanomater., 2009, 113(17):7371-7378.

[92] Gao F., Zeng D., Huang Q., Tian S., Xie C., Chemically bonded graphene/ BiOCl nanocomposites as high-performance photocatalysts, Phys. Chem., 2012, 14(30): 10572-10578.

[93] Song S., Gao W., Wang X., Li X., Liu D., Xing Y., Zhang H., Microwave-assisted synthesis of BiOBr/graphene nanocomposites and their enhanced photocatalytic activity, Dalton T., 2012, 41(34):10472-10476.

[94] Liu Z., Xu W., Fang J., Xu X., Wu S., Zhu X., Chen Z., Decoration of BiOI quantum size nanoparticles with reduced graphene oxide in enhanced visible-light-driven photocatalytic studies, Appl. Surf. Sci., 2012, 259(41):441-447.

[95] Li H., Shang J., Ai Z., Zhang L., Efficient visible light nitrogen fixation with BiOBr nanosheets of oxygen vacancies on the exposed {001} facets, J.Am. Chem. Soc., 2015, 137:6393−6399.

[96] Yin H., Chen X., Hou R., Zhu H., Li S., Huo Y., Li H., Ag/BiOBr film in a rotating-disk reactor containing long-afterglow phosphor for round-the-clock photocatalysis, ACS Appl. Mater. Inter., 2015, 7:20076-20082.

[97] Huo Y., Hou R., Chen X., Yin H., Gao Y., Li H., BiOBr visible-lightphotocatalytic films in a rotating disk reactor for the degradation of organics, J. Mater. Chem. A, 2015, 3:14801-14808.

[98] Zhang X., Ai Z., Jia F., Zhang L., Generalized one-pot synthesis, characterization, and photocatalytic activity of hierarchical BiOX (X = Cl, Br, I) nanoplate microspheres, J. Phys. Chem. C, 2008, 112 (3):747-753.

[99] Fang Y., Ma W., Huang Y., Cheng G., Exploring the reactivity of multicomponent

photocatalysts: insight into the complex valence band of BiOBr, Chem-Eur. J., 2013, 19 (9): 3224-3229.

[100] Ye L., Tian L., Peng T., Zan L., Synthesis of highly symmetrical BiOI single-crystal nanosheets and their {001} facet-dependent photoactivity, J. Mater. Chem., 2011, 21 (33):12479-12484.

[101] Huang H., Han X., Li X., Wang S., Chu P., Zhang Y., Multiple heterojunctions fabrication with tunable visible-light-active photocatalytic reactivity in the BiOBr-BiOI fullrange composites based on microstructure modulation and band structures, ACS Appl. Mater.Inter., 2015, 7:482–492.

[102] Guo Y., Huang H., He Y., Tian N., Zhang T., Chu P., An Q., Zhang Y., *In situ* crystallization for fabrication of a core–satellite structured BiOBr–CdS heterostructure with excellent visible-light-responsive photoreactivity, Nanoscale, 2015, 7:11702–11711.

[103] Wu X., Wang L., Du Y., Dou S., Amal R., Scott J., Improving the photo-oxidative capability of BiOBr via crystal facet engineering, J. Mater. Chem. A, 2017, 5(17):8117-8124.

[104] Wu D., Yue S., Wang W., An T., Li G., Ye L., Yin H. Y., Wong P. K., Influence of photoinduced Bi-related self-doping on the photocatalytic activity of BiOBr nanosheets, Appl. Surf. Sci., 2017, 391:516-524.

[105] Yan P., Xu L., Jiang D., Li H., Xia J., Zhang Q., Hua M., Li H., Photoelectrochemical monitoring of ciprofloxacin based on metallic Bi self-doping BiOBr nanocomposites, Electrochimica Acta, 2018, 259:873-881.

[106] Guo J., Liao X., Lee M.-H., Hyett G., Huang C.-C., Hewak D.W., Mailis S., Zhou W., Jiang Z., Experimental and DFT insights of the Zn-doping effects on the visible-light photocatalytic water splitting and dye decomposition over Zn-doped BiOBr photocatalysts, Appl. Catal. B-Environ., 2019, 243:502-512.

[107] Yin S., Fan W., Di J., Wu T., Yan J., He M., Xia J., Li H., La^{3+} doped BiOBr microsphere with enhanced visible light photocatalytic activity, Colloid Surface A, 2017, 513:160-167.

[108] Guo W., Qin Q., Geng L., Wang D., Guo Y., YangY., Morphology-controlled preparation and plasmon-enhancedphotocatalytic activity of Pt–BiOBr heterostructures, J. hazard. Mater., 2016, 308:374-385.

[109] Li J., Dong X., Sun Y., Cen W., Dong F., Facet-dependent interfacial charge separation

and transfer in plasmonic photocatalysts, Appl. Catal. B-Environ., 2018, 226:269-277.

[110] Yu C., Fan C., Meng X., Yang K., Cao F., A novel Ag/BiOBr nanoplate catalyst with high photocatalytic activity in the decomposition of dyes, React. Kinet. Mech. Catal., 2011, 103:141-151.

[111] Liu H., Cao W., Su Y., Wang Y., Wang X., Synthesis, characterization and photocatalytic performance of novel visible-light induced Ag/BiOI, Appl. Catal. B-Environ., 2012, 111 112: 271-279

[112] Li Y., Liu M., Chen L., Polyoxometalate built-in conjugated microporous polymers for visible-light heterogeneous photocatalysis, J. Mater. Chem. A, 2017, 5:13757-13762.

[113] Xiang Y., Ju P., Wang Y., Sun Y., Zhang D., Yu J., Chemical etching preparation of the Bi_2WO_6/BiOI p–n heterojunction with enhanced photocatalytic antifouling activity under visible light irradiation, Chem. Eng. J., 2016, 288: 264-275.

[114] Fu J., Tian Y., Chang B., Xia F., Dong X., BiOBr-carbon nitride heterojunctions: synthesis，enhanced activity and photocatalytic mechanism, J. Mater. Chem., 2012, 22: 21159-21166.

[115] Singha P., Jiang Z., Lai H., Nicholls R., Xiao T., Jones M., Edwards P., In situ formed Bi/$BiOBr_xI_{1-x}$ heterojunction of hierarchical microspheres for efficient visible-light photocatalytic activity, J. Saudi Chem. Soc., 2012, 293:116-125.

[116] Zheng C., Cao C., Ali Z., A hemin binding G-quadruplex/Pb^{2+} complex to construct a visible light activated photoelectrochemical sensor on a ZnO/BiOI heterostructure, Phys. Chem. Chem. Phys., 2015,17:13347-13354.

[117] Zhang X., Zhang L., Xie T., Wang D., Low-temperature synthesis and high visible-light-induced photocatalytic activity of BiOI/TiO_2 heterostructures, J. Phys. Chem. C, 2009, 113:7371-7378.

[118] Lin W., Yu X., Zhu Y., Zhang Y., Graphene oxide/BiOCl nanocomposite films as efficient visible light photocatalysts, Front. Chem., 2018, 14 (30): 1052-1058.

[119] Zang Y., Ding E., Preparation and properties of phase change materials PEG/CPE, Petrochem. Tech. Appl., 2008, 26:224-226. (in Chinese)

[120] Nematollahzadeh A., Seraj S., Mirzayi B., Catecholamine coated maghemite nanoparticles for the environmental remediation: Hexavalent chromium ions removal, Chem. Eng. J., 2015, 277: 21-29.

[121] Zhao Y., Tan X., Yu T., Wang S., SDS-assisted solvothermal synthesis of BiOBr microspheres with highly visible-light photocatalytic activity, Mater. Lett.,

2016,164:243-247.

[122] Mao D., Ding S., Meng L., Dai Y., Sun C., Yang S., He H., One-pot microemulsion mediated synthesis of Bi-rich $Bi_4O_5Br_2$ with controllable morphologies and excellent visible-light photocatalytic removal of pollutants, Appl. Catal. B: Environ., 2017, 207:153-165.

[123] Herrmann J., Tahiri H., Ait-Ichou Y., Lassaletta G., González-Elipe A., Fernandez A., Characterization and photocatalytic activity in aqueous medium of TiO_2 and Ag-TiO_2 coatings on quartz, Appl. Catal. B: Environ., 1997, 13:219–228.

[124] Gate L. F., Comparison of the photon diffusion model and Kubelka-Munk equation with the exact solution of the radiative transport equation, Appl. Optics, 1974, 13:236-238.

[125] Xiong X., Ding L., Wang Q., Li Y., Jiang Q., Hu J., Synthesis and photocatalytic activity of BiOBr nanosheets with tunable exposed {010} facets, Appl. Catal. B: Environ., 2016, 188:283-291.

[126] Chen L., Huang R., Xiong M., Yuan Q., He J., Jia J., Yao M., Luo S., Au C., Yin S., Room-temperature synthesis of flower-like BiOX (X= Cl, Br, I) hierarchical structure and their visible-light photocatalytic activity, Inorg. Chem., 2013, 52:11118-11125.

[127] Wu N., Wang J, Tafen D., Wang H., Zheng J., Lewis J., Liu X., Leonard S., Manivannan A., Shape-enhanced Photocatalytic Activity of Single-crystalline Anatase TiO_2 (101) Nanobelts, J. Am. Chem.Soc., 2010, 132(132): 6679-6685.

[128] Yuan E., Wu C., Liu G., Li G., Wang L., Effects of SBA-15 physicochemical properties on performance of Pd/SBA-15 catalysts in 2-ethyl-anthraquinone hydrogena-tion, J. Indust. Eng. Chem., 2018, 66:158-167.

[129] Li G., Wang B., Xu W., Han Y., Sun Q., Rapid TiO_2/SBA-15 synthesis from il-menite and use in photocatalytic degradation of dimethoate under simulated solar light, Dyes Pigments, 2018, 155:265-267.

[130] Liu J., Huang H., Liu X., Xiao J., Zhong S., She X., Fu Z., Kirk S.R., Yin D., Preparation of Fe_2O_3 doped SBA-15 for vapor phase ortho-position C-alkylation of phenol with methanol, Catal. Commun., 2017, 92:90-94.

[131] Zhang Z., Luo Y., Guo Y., Shi W., Wang W., Zhang B., Zhang R., Bao X., Wu S., Cui F., Pd and Pt nanoparticles supported on the mesoporous silica molecular sieve SBA-15 with enhanced activity and stability in catalytic bromate reduction, Chem. Eng. J., 2018, 344:114-123.

[132] Chen D., Ray A., Photodegradation kinetics of 4-nitrophenol in TiO_2 suspension, Water

Res., 1998, 32:3223-3234.

[133] Cheng M., Zhao H., Yang J., Zhao J., Yan L., Song H., Chou L., The catalytic dehydrogenation of isobutane and the stability enhancement over Fe incorporated SBA-15, Micropor. Mesopor. Mat., 2018, 266:117-125.

[134] Zhao D., Sun J., Li Q., Stucky G.D., Morphological control of highly ordered mesoporous silica SBA-15, Chem. Mater., 2000, 12:275-279.

[135] Zhang M., Shao C., Mu J., Huang X., Zhang Z., Hierarchical heterostructures of Bi_2MoO_6 on carbon nanofibers: controllable solvothermal fabrication and enhanced visible photocatalytic properties, J. Mater. Chem., 2011, 22:577-584.

[136] Bian L., Zhang L., Zhu Z., Li Z., Methanation of carbon oxides on Ni/Ce/SBA-15 pretreated with dielectric barrier discharge plasma, Mol. Catal., 2018, 446:131–139.

[137] Liu C., Lin X., Li Y., Xu P., Li M., Chen F., Enhanced photocatalytic performanceof mesoporous TiO_2 coated SBA-15 nanocomposites fabricated through anovel approach: supercritical deposition aided by liquid-crystal template, Mater. Res. Bull., 2016, 75:25-34.

[138] Xia F., Ou E., Wang L., Wang J., Photocatalytic degradation of dyes over cobalt doped mesoporous SBA-15 under sunlight, *Dyes Pigment*, 2008, 76:76-81.

[139] Wang Y., Bai X., Pan C., He J., Zhu Y., Enhancement of photocatalytic activity of Bi_2WO_6 hybridized with graphite-like C_3N_4, J. Mater. Chem., 2012, 22:11568-11573.

[140] Zhou L., Wang W., Liu S., Zhang L., Xu H., Zhu W., A sonochemical route to visible-light-driven high-activity $BiVO_4$ photocatalyst, J. Mol. Catal. A: Chem., 2006, 252:120-124.

[141] Long M., Cai W., Cai J., Zhou B., Chai X., Wu Y., Efficient photocatalytic degradation of phenol over $Co_3O_4/BiVO_4$ composite under visible light irradiation, J. Phys. Chem. B, 2006, 110:20211-20216.

[142] Liu G., Niu P., Sun C., Smith S., Chen Z., Lu G., Cheng H., Unique electronic structure induced high photoreactivity of sulfur-doped graphitic C_3N_4, J. Am. Chem. Soc., 2010, 132:11642–11648

[143] Priya R., SethuRaman M., SenthilKumar N., Chandrasekaran J., Balan R., Synthesis and characterization of CTAB-assisted WO_3 deposited on silicon for the fabrication of photoresponse p-n junction diode, Optik, 2016, 127:7913-7924.

[144] Zeng J., Hu M., Wang W., Chen H., Qin Y., NO_2-sensing properties of porous WO_3 gas sensor based on anodized sputtered tungsten thin film, Sensor. Actuat. B:

Chem., 2012, 161(1):447–452.

[145] Long H., Zeng W., Zhang H., Synthesis of WO_3 and its gas sensing: a review, J. Mat. Sci.: Mat. Electron., 2015, 26(7):4698–4707.

[146] Nandiyanto A., Arutanti O., Ogi T., Iskandar F., Kim T., Okuyama K., "Synthesis of spherical macroporous WO_3 particles and their high photocatalytic performance," Chem. Eng. Sci., 2013, 101:523–532.

[147] Aflaki M., Davar F., Synthesis, luminescence and photocatalyst properties of zirconia nanosheets by modified Pechini method, J. Mol. Liq., 2016, 221:1071-1079.

[148] Venkata Reddy Ch., Babu B., Neelakanta Reddy I., Shim J., Synthesis and characterization of pure tetragonal ZrO_2 nanoparticles with enhanced photocatalytic activity, Ceram. Int., 2018, 44: 6940-6948.

[149] Bansal P., Chaudhary G. R., Mehta S.K., Comparative study of catalytic activity of ZrO_2 nanoparticles for sonocatalytic and photocatalytic degradation of cationic and anionic dyes, 2015, 280:475-485.

[150] Zhu W., Shu Y., Yin D., Ni Z., Chen M., Study on visible light catalytic with WO_3-ZrO_2/SBA-15, J. Chongqing Univ., 2018, 41(8):26-33. (in Chinese)

[151] Jabbari V., Hamadanian M., Shamshiric M., Villagrána D., Band gap and Schottky barrier engineered photocatalyst with promising solar light activity for water remediation, RSC Adv., 2016, 6:15678-15685.

[152] Zhang W., Chen S., He M., Zhu G., Facile hydrolysis synthesis of $Bi_4O_5Br_2$ photocatalyst with excellent visible light photocatalytic performance for the degradation of resorcinol, RSC Adv., 2016, 6(53):47545-47551.

[153] Huang L., Xu H., Zhang R., Cheng X., Xia J., Xu Y., Li H., Synthesis and characterization of g-C_3N_4/MoO_3 photocatalyst with improved visible-light photoactivity, Appl. Surf. Sci., 2013, 283(14): 25-32.

[154] Gu Y., Chen L., Shi L., Ma J., Yang Z., Qian Y., Synthesis of C_3N_4 and graphite by reacting cyanuric chloride with calcium cyanamide, Carbon, 2003, 41(13): 2653-2689.

[155] Zhao J., Ji M., Di J., Ge Y., Zhang P., Xia J., Li H., Synthesis of g-C_3N_4/$Bi_4O_5Br_2$ via reactable ionic liquid and its cooperation effect for the enhanced photocatalytic behavior towards ciprofloxacin degradation, J. Photoch. Photobio A, 2017, 347:168-176.

[156] Wang Y., Bai X., Pan C., Zhu Y., Enhancement of photocatalytic activity of

Bi_2WO_6 hybridized with graphite-like C_3N_4. J. Mater. Chem., 2012, 22(23): 11568-11573.

[157] Horibe T., Kusaba K., Niwa K, Hasegawa M., Yasuda K., Iahigami R., Molecular routes syntheses of graphite-like C–N compounds with various N/C ratios in high pressure and temperature, J. Ceram. Soc. JPN, 2016, 124:1013-1016.

[158] Franklin E., The ammono carbonic acids, J. Am. Chem. Soc., 1922, 44(3): 486-509.

[159] Liu A., Cohen M., Prediction of new low compressibility solids, Science, 1989, 245(4920): 841-842.

[160] Guo Q., Yang Q., Yi C., Zhu L., Xie Y., Synthesis of carbon nitrides with graphite-like or onion-like lamellar structures via a solvent-free route at low temperatures, Carbon, 2005, 43(7): 1386-1391.

Acknowledgements

How time flies. Five years will soon pass, and my overseas study will be over after these 5 wonderful years' stay here. Today, I think it's time to say thank you to all the people who gave me help and guidance all the time not only to my study and research, but also to my life.

First of all I would like to say thank you from the bottom of my heart to my supervisors, dear Professor Zhengya Zhang and Professor Zhongfang Lei for giving me the opportunity to study for a doctoral degree in Japan, and their careful guidance and kindness always make me feel optimistic to face all the problems I met in my research and life. I also want to thank Professor Mingqing Chen, Professor Zengwei Yuan, Professor Guixue Wang, Professor Zhemin Zhou, Professor Chuanping Feng, Professor Zhenhui Kang, Professor Weidong Shi, Professor Yong Zhou and Professor Dajun Shu in China for the help and guidance in my research and life.

Secondly, I want to say thanks to all the members in Professor Zhang's research group in University of Tsukuba and the members in Professor Chen's group in Jiangnan University. Because of your help, I could continue my study and research with energy and enough time.

Thirdly, special thanks should go to my thesis committee members, Professors Zhenya Zhang, Zhongfang Lei, Kazuya Shimizu and Helmut Yabar for their patiently reading and listening, and valuable suggestions and comments. All the instructors provided great help for the improvement of my dissertation and future study.

Fourthly, I want to say thank you to all the members of our groups in China and Japan. Thanks for your help in the colorful years when we studied and worked together. Whenever I had a question, we could communicate with each other.

Finally, I would like to express my gratitude to my parents, my husband and my son. They are always standing by me to give support and make me feel strong.

Publication

Y. Shu, S. Yan, K. Dong, J. Chen, Preparation of novel mesoporous photocatalyst $Bi_4O_5Br_2$/SBA-15 with enhanced visible-light-driven catalytic activity, Open Journal of Applied Science, 2018, **8**:532-544.